Condensation phenomena in Fuel-cell Turbochargers

A Numerical Study

Master of Science Thesis

Anwesha Das

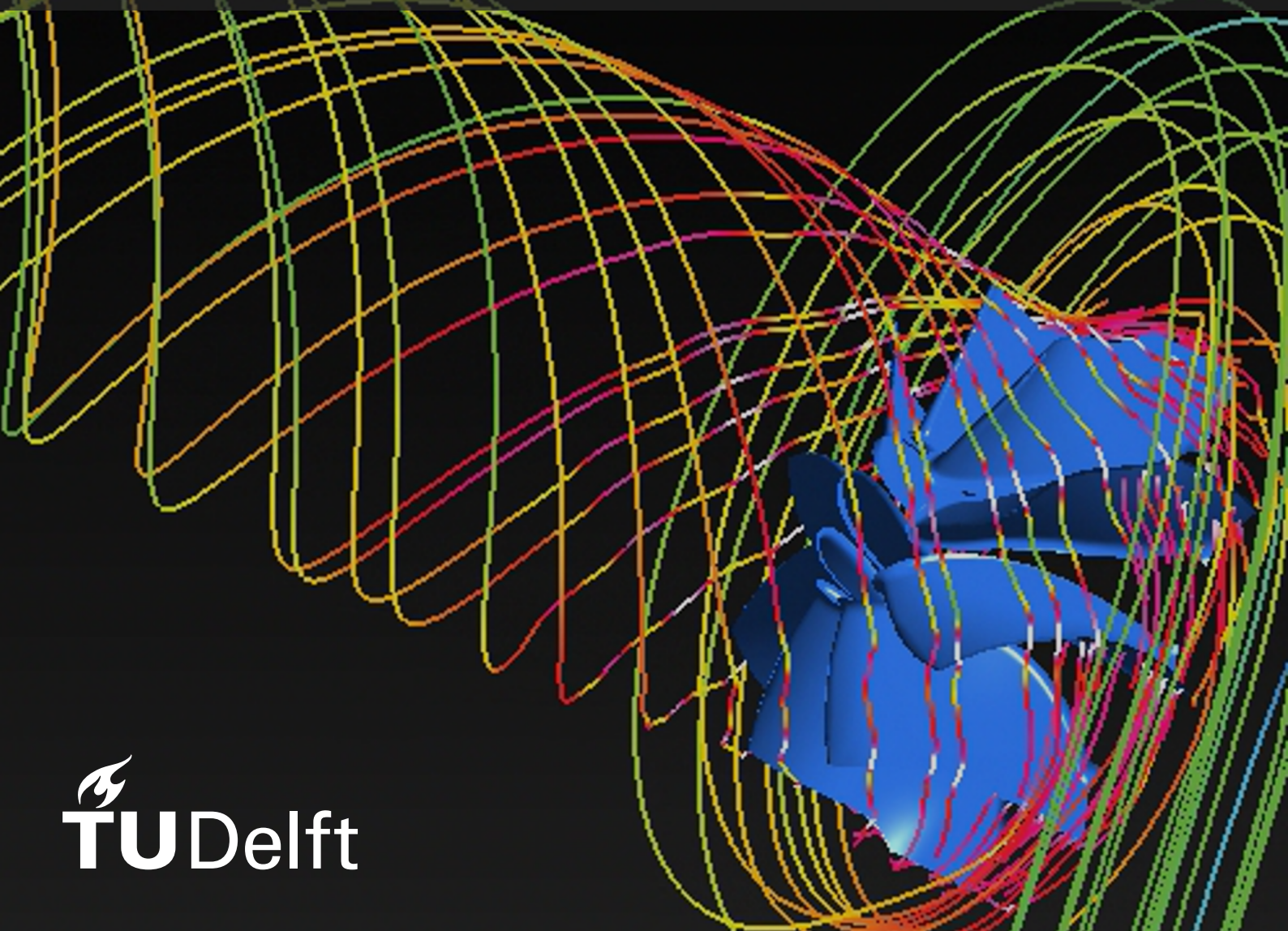

TU Delft

Condensation phenomena in Fuel-cell Turbochargers

A Numerical Study

---

by

Anwesha Das

in partial fulfillment of the requirements for the degree of

Master of Science
in Mechanical Engineering

at the Delft University of Technology,
to be defended publicly on Thursday, August 21, 2025, at 10:30 hrs.

Student number:	5946778	
Project Duration:	November 2024 - August 2025	
Thesis committee:	Dr. Maria Martinez Garcia	MTEE, Supervisor
	Dr. Pedro S. Costa	TU Delft, Chair
	Prof. dr. Rene Pecnik	TU Delft, Examiner

MITSUBISHI TURBOCHARGER AND ENGINE EUROPE

TU Delft

Acknowledgments

This journey of the past nine months has been as fulfilling, as it was intense. Full of highs and lows, it taught me the importance of patience and perseverance, and to celebrate every little achievement. I express my deep gratitude for everyone who stood by me throughout this period.

Firstly, I would like to thank my supervisors Dr. Martinez Garcia and Dr. Costa. In the midst of their own demanding responsibilities and schedules, they were always available to help. Whether it was to clarify a concept or just to listen and reassure me when things got overwhelming, I could always count on their unwavering support and insights. They spared no effort to make every resource available for me to work with, and the many discussions we had greatly helped refine my understanding and problem-solving approach. I am extremely grateful for the incredibly opportunity to join the MTEE Turbo engineering team, and learn from seasoned engineers. I can only be grateful to them for making my first exposure to the industry such an enriching experience.

I owe a debt of gratitude to my friends, here and back home in India. Their faith in me has always been my biggest strength. Thank you for all the beautiful experiences - the late night walks, the trips to the cinema, the biryani sessions, the game nights and so much more. I'll always cherish these memories. Your presence has sustained me in ways words cannot express.

Above all, my parents have been my pillar. In spite of the distance, they have been so encouraging and unconditionally supportive. They have taught me to be resilient and pursue the dreams I have, and they are the reason I have come this far today. The thesis, and my journey so far, belongs just as much to them as it does to me, and I can only hope to make them proud.

Anwesha Das
Delft, August 2025

Abstract

Fuel cell vehicle (FCV) technology is gaining traction as a promising alternative to traditional internal combustion engines as well as battery-powered electric vehicles. In order to enhance performance and improve efficiency, turbocharging can be integrated into the system, in which the fuel cell exhaust air containing water-vapor can be passed through a turbine to retrieve some energy. However, the introduction of humid air into the turbine can lead to the flow condensing as it expands. This is of particular concern to Mitsubishi Heavy Industries Engine & Turbocharger Co., Ltd. (MHIET), as condensation of steam can alter flow conditions by causing significant heat release, compromising efficiency. The water droplets formed can also lead to mechanical damage by erosion.

The current study presents a numerical investigation of this process in such a turbine using Computational Fluid Dynamics (CFD). Existing computational research conducted on condensation phenomena in nozzles and steam turbines was surveyed, and the insights obtained from literature were extended to the current case. The Euler-Euler framework was used in ANSYS Fluent to evaluate the two-phase flow field, and to identify the location and intensity of the onset of condensation. Coupled with a User-Defined Function (UDF) to trigger condensation and appropriate turbulence and multiphase models, the interphase exchange of heat and mass was captured.

The model was validated against a benchmark nozzle case, and subsequently applied to the turbine setup. A mesh independence study was performed to ensure a reasonable balance between accuracy and computational expense. Several surfaces of analysis were carefully chosen and illustrated to convey the meaning of the results obtained from the simulations and highlight key flow features. The effect of the latent heat release was pronounced, and flow fields for the wet case were compared to the hypothetical dry case under the same conditions, to isolate the impact of liquid generation. The results showed good qualitative agreement with results from similar studies.

A series of parametric studies were undertaken to investigate the effects of relative humidity at the inlet, the inlet pressure and the rotational speed. Higher relative humidity was observed to cause a stronger subcooling leading to higher liquid generation. The subsequent heating up of the flow raised the power potential of the flow, leading to a marginal increase in efficiency as the air got more humid. However, as compared to the dry cases (not undergoing condensation) with the same relative humidity, the corresponding wet cases exhibited a drop in efficiency due to the loss in gaseous mass flow.

The impact of the inlet pressure was investigated. The phenomenon of thermal throttling was discussed, where, to maintain a fixed mass flow rate, the pressure ratio across the turbine altered. The effective pressure drop was seen to drop once condensation ensued. The amount of liquid generated was governed by a balance of expansion and outlet heating effects. Further, for increasing rotational speeds, the liquid generation was found to rise and attain a peak. However, on increasing it further, the amount of liquid condensing declined.

The findings offered valuable insights into the flow behavior in humidified fuel-cell turbocharging systems, and their implications for the air-management system was discussed. Some recommendations were proposed to enhance the performance of the model and make it more comprehensive.

Contents

List of Figures

List of Tables

Nomenclature

Abbreviations

Abbreviation	Definition
CFD	Computational Fluid Dynamics
DNS	Direct Numerical Simulation
EE	Euler-Euler
EL	Euler-Lagrange
FANS	Favre-Averaged Navier-Stokes
LES	Large Eddy Simulation
LMF	Liquid Mass Fraction
MRF	Multiple Reference Frame
MTEE	Mitsubishi Turbocharger and Engine Europe
PEMFC	Proton Exchange Membrane Fuel Cell
PR	Pressure Ratio
RANS	Reynolds-Averaged Navier–Stokes
RH	Relative Humidity
RPM	Revolutions Per Minute
UDF	User-Defined Function (in Fluent CFD)

Symbols

Symbol	Definition	Unit
C_p	Specific heat capacity at constant pressure	[J/kg.K]
G	Gibbs free energy	[J]
Δh	Specific enthalpy change	[J/kg]
J/J_{CL}	Classical nucleation rate	[1/m^{3}s]
J_{niso}	Non-isothermal nucleation rate	[1/m^{3}s]
k	Turbulent kinetic energy	[m^2/s^2]
$\dot{m}$	Mass flow rate	[kg/s]
P	Pressure	[Pa]
P_{sat}	Saturation pressure	[Pa]
R	Universal gas constant	[J/kg.K]
S	Supersaturation ratio	[-]
T	Temperature	[K]
T_{sat}	Saturation temperature	[K]
ΔT	Subcooling	[K]
V	Velocity	[m/s]
y	Liquid mass fraction	[-]
α	Liquid volume fraction	[-]
γ	Ratio of specific heats	[-]
ϵ	Turbulent dissipation rate	[m^2/s^3]
η_{isen}	Isentropic efficiency	[-]
θ	Azimuthal angle	[°]
κ_T	Isothermal compressibility	[1/Pa]
ρ_l	Liquid density	[kg/m^3]
ρ_v	Vapor density	[kg/m^3]

Symbol	Definition	Unit
σ	Surface tension coefficient	[N/m]
τ	Torque	[Nm]
Ω	Rotational velocity	[rad/s]
ω	Specific dissipation rate	[1/s]

1

Introduction

1.1. Background and Motivation

Since its advent, the automotive industry has been dependent on non-renewable sources of energy such as fossil fuels, which offer high energy density and inexpensive fabrication and handling. Over recent decades, hazardous emissions and depletion of these conventional fuels have been pressing issues for the transportation sector. The current energy scenario is extremely unsustainable and it is the need of the hour to adopt cleaner alternative fuels. Electric vehicles (EVs) have been a hot topic for research throughout the past decade, as they appear to be one of the ideal solutions to the looming global energy crisis.

A general classification of EVs sort them into five types - Battery Electric Vehicles (BEVs), Hybrid Electric Vehicles (HEVs), Plug-In Hybrid Electric Vehicles (PHEVs), Fuel Cell Electric Vehicles (FCEVs) and Extended-range EVs (ER-EVs) [1]. The development of fuel cell electric vehicle (FCEV) technology has garnered growing appeal, as it is a great option to address energy autonomy problems faced by battery-electric vehicles [2]. Vehicles utilizing fuel cell technology have the potential to significantly increase fuel economy and deliver performance comparable to traditional internal combustion (IC) engines. A fuel cell is directly analogous to an IC engine, as it electrochemically converts chemical energy stored in the fuel to rotational mechanical energy [3].

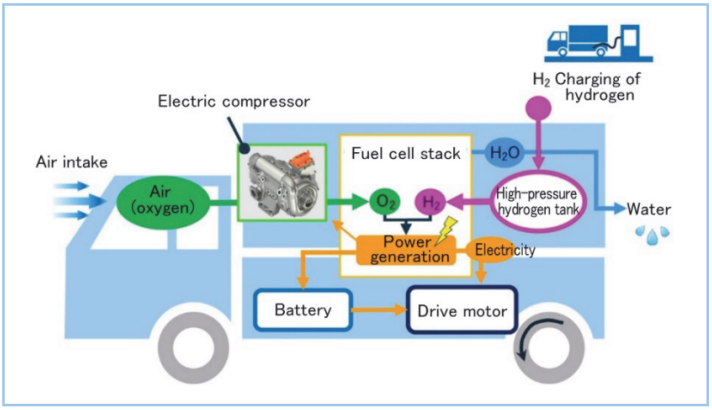

Figure 1.1: Diagram of vehicle system with fuel cells [4].

The layout of a fuel cell is shown in Figure 1.1. A boosting system, generally an electric compressor, is used to supply air into the fuel cell stack, which is the primary power source. This stack consists of multiple fuel cells that produce electricity through a chemical reaction involving hydrogen and oxygen. The fuel tank is placed at the rear of the vehicle, and stores pressurized hydrogen fuel. There is a

battery pack that provides the electricity for start-up and stores energy generated from regenerative braking. The fuel cell provides power to run the drive motor as well as to charge the battery when excess energy is available. Besides these, there are power electronics controller and thermal management systems. A turbocharging system is often introduced to assist the power requirements of the compressor by extracting energy from the fuel cell exhaust gases.

Among the available types of fuel cells, proton exchange membrane fuel cells (PEMFCs) are the most widely used as they use hydrogen as a fuel and oxygen as an oxidant. Using hydrogen offers the advantage of the cell reaction products only being water and heat, and can deliver fuel efficiencies as high as 65%. PEMFCs seem to be the best suited for automobile applications due to optimum operating points, automatic control [5] and their freeze start ability at low temperatures [6]. Turbocharging can be implemented in such PEMFC systems to increase efficiency.

1.1.1. MTEE's Development of FC Turbochargers

Mitsubishi Turbocharger and Engine Europe (MTEE) is a prominent global producer specializing in state-of-the-art engine and turbocharger technologies. With the provision of hydrogen infrastructure, fuel cell systems are anticipated to be widely used in the transportation and industrial sectors by 2030. MTEE is one of the leading enterprises in this transition, focusing on the development of highly efficient electric turbochargers for fuel cell systems, facilitating the shift from internal combustion engine vehicles to zero-emission alternatives [7]. As per the power demand, MTEE is focusing on improving the efficiency of their turbochargers with motor outputs of 25-30 kW, capable of operating at speeds of up to 100,000 rpm or more. Currently, MTEE is developing its second generation of electric compressors for FC turbochargers.

This technology comes with its own set of challenges, such as energy density issues of the hydrogen fuel. This is overcome by using a boosting system in the air supply, and thus the air supply system of the fuel cell needs an electric compressor to improve performance [8]. This leads to the possibility of the integration of a turbocharging system into the design, to assist the compressor using a turbine. The principle of turbocharging is discussed ahead.

1.2. Working Principle of Turbochargers

1.2.1. Traditional ICE Turbochargers

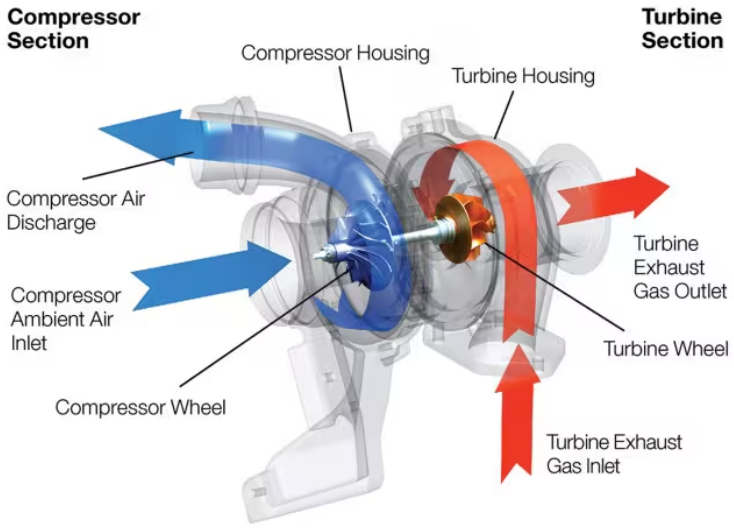

Figure 1.2: Components of a turbocharger used in IC engines [9].

In IC engines, a turbocharger consists of a centrifugal compressor wheel and a turbine wheel connected by a shaft. The purpose of this device is to boost the engine's volumetric efficiency and improve performance. On one side, the compressor pre-compresses the air before it enters the intake manifold

to increase the intake density. On the other hand, the high temperature and pressure of the exhaust gases rotate the turbine wheel, thereby generating power to assist the compressor. The entire process allows more fuel to be burned by packing more into the cylinders, resulting in greater power output. In addition to that, power is extracted from the exhaust gases that would otherwise spew from the tailpipe as wasted energy. Figure 1.2 shows the working mechanism.

Turbochargers somewhat restrict exhaust flow, making it a little more energy-expensive for the engine to empty each cylinder. However, they use up relatively less engine power than superchargers, which makes them ideal for smaller, less-powerful engines and greatly improves the fuel economy of the car. In terms of construction and function, a turbocharger is designed for the service life of the engine. However, in practice, high-performance components in the exhaust gas system are subject to diverse risk factors that can lead to premature failure. These include oil contamination, inadequate lubrication, etc. Additional challenges arise when designing turbochargers for fuel cell vehicles, which will be discussed ahead.

1.2.2. Proton Exchange Membrane Fuel Cell (PEMFC) Turbochargers

PEMFC System

Many types of fuel cells have been developed and are suited for use in the automobile industry. The most popular fuel cell technology is the Proton-Exchange Membrane Fuel Cell (PEMFC). It is versatile, durable, and can be used for a wide range of applications. PEMFCs have the ability to effectively convert hydrogen into electricity with water and heat as by-products. The benefits provided by this technology are high power density, reduced emissions, and relatively low operating temperature and pressure, making them a great candidate for long-range fuel cell - hybrid electric vehicles (FC-HEVs).

A single PEMFC cell is shown in Figure 1.3. It consists of an electrolyte sandwiched between two electrodes. Oxygen from air passes over one electrode and hydrogen over the other, generating electricity, water and heat. Bipolar plates on either side of the cell help to distribute gases and collect the electrical current. These fuel cells layered together make a 'stack', which gives scalability to the design, allowing configuration into a wide array of sizes [10].

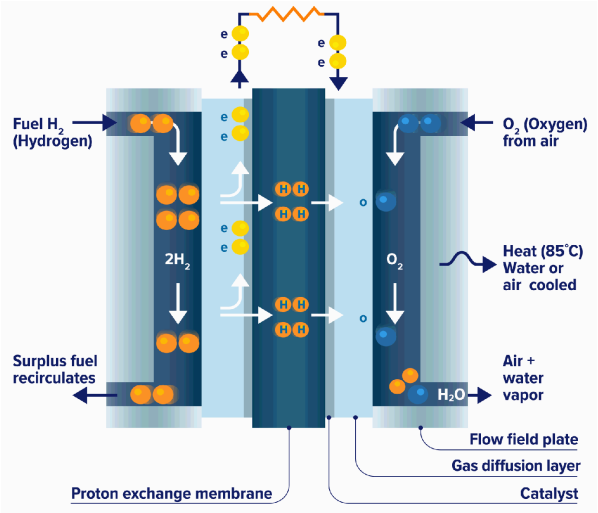

Figure 1.3: A Proton Exchange Membrane Fuel Cell (PEMFC) [10].

An air-supply system, a fuel supply system, a temperature management system, and a stack make up a typical PEMFC system, as depicted in Figure 1.3. The air-supply system provides compressed and humidified air to the stack and is made up of a compressor and a membrane humidifier. The membrane is humidified to maintain proton conductivity to complete the circuit. The system receives air from the compressor, which heats and pressurizes the gases. At the cathode output, the membrane humidifier hydrates the dry incoming air from the compressor by transferring water vapor from the humid exhaust gases [11].

The variations in temperature and concentration between the dry gases from the compressor and the wet gases from the stack generate this heat and mass transfer. The fuel-supply system, which includes a regulator, an ejector, and a high-pressure hydrogen storage tank, provides hydrogen to the stack. The operating temperature of the fuel cell stack is typically 60-100°C.

The stack receives its hydrogen from the storage tank, and the ejector aids in its circulation. The thermal management system regulates the stack's operational temperature and is made up of a cooling fan, radiator, and coolant pump. Depending on the system loads and ambient temperature, the fan and pump speeds regulate the system's heat evacuation.

Why is Turbocharging required?

The system efficiency and the balance of plant (BOP), i.e., the auxiliary components of the system needed to deliver the energy, are some aspects that require consideration. Even with a very efficient stack, the overall efficiency might go down due to the power consumption of the BOP. The coolant pump, radiator, circulation pump, etc. aggravate the energy consumption of the system, upto 25% of the stack power output [12]. Providing a higher operating pressure with a compressor can improve the performance and downsize the system, but the power expenditure rises.

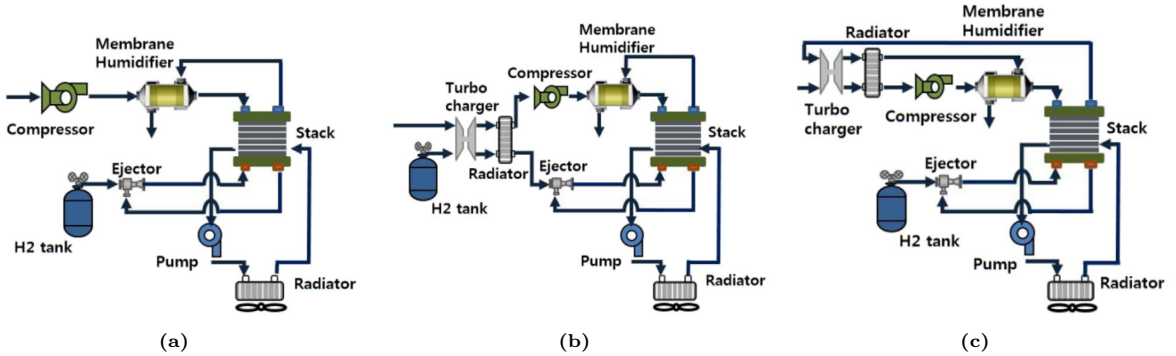

Figure 1.4: (a) Basic PEMFC system; (b) PEMFC system with turbocharger in the fuel supply unit; (c) PEMFC system with turbocharger in the air supply unit [13].

The best way to improve efficiency is to utilize the waste energy of the system. The installation of a turbocharger is a straightforward method of using the wasted kinetic energy of the gas, as a turbine can power the compressor. When adding a turbocharger, the location of the installation should be planned in advance. Both the cathode outlet of the stack and the hydrogen storage tank's outlet are suitable locations for the turbocharger, as shown in Figure 1.4. There are advantages and trade-offs associated with both these locations.

If the turbocharger is mounted right after the hydrogen tank, it can use the pressure energy of the tank without impacting the humidity and temperature of the cathode inlet gas, but, because of the low mass flow rate of hydrogen, the energy recovery will be minimal. Conversely, if the turbocharger is positioned near the stack cathode outlet (T-ASS), it can utilize the kinetic energy of production gases; however, the flow conditions following the turbocharger will impair the performance of the humidifier and the overall stack [13]. Usually the turbocharger is placed in the air-supply unit, where the product gas from the cathode side of the stack rotates the turbine.

The fuel cell stack requires a significant amount of energy to pressurize. The fuel cell stack's "exhaust gas" has considerable energy that can be used to aid with compression. The efficiency of the turbine-assisted compressor system rises, since the turbine may supply between 25% and 30% of the necessary compressor power, even more with assistance available in optimal matching conditions [14]. Additionally, the size of the inverter and motor can be decreased.

Overall, the turbine in the turbocharger recovers the work, which is then used in the compressor. However, the inclusion of the turbine gives rise to other challenges, such as condensation due to expansion, which can lead to decreased volumetric efficiency and mechanical damage to the components. Traditionally, in IC engines, the turbine inlet temperature is so high that condensation is not a typical problem.

However, the operating temperature of the fuel cells is around 100°C, and when the gases enter the turbine at these temperatures and expand, condensation is likely to occur. This can cause the flow to heat up and reach thermodynamic equilibrium, hindering expansion, as well as problems like droplet deposition on blades and erosion. Investigating this problem of condensation in FC turbochargers will be the focus of our project.

1.2.3. Structure of the Report

The investigation of the problem of condensation in fuel cell turbocharger turbines is undertaken in this study. The thesis is organized into several chapters that guide the reader through the literature review, modeling, and analysis of the results.

Chapter 2 deals with the review of relevant literature discussing the phenomena of condensation in turbines, and introducing the treatment of some mathematical concepts used for modeling. The gap in the research is identified, and the main research questions are formulated.

Chapter 3 describes the methodology or the modeling approach used for solving the problem. The theoretical & numerical framework and some elements of the commercial software used for the computational study are discussed.

Chapter 4 presents the results, including the validation of the model used, and parametric studies. The research questions are addressed and answered in this section.

Finally, **Chapter 5** concludes the study with a summary of the findings, limitations, and recommendations for future work.

2

Literature Survey

In this chapter, a survey of available published literature on the topic of condensation phenomena in turbines is undertaken. The relevant theory and modeling approaches are explored, in order to identify the gap in research. Finally, research questions and objectives are formulated to guide the choice of methodology (Chapter 3) and the analysis of the results (Chapter 4).

2.1. Condensation in Turbines

The problem of condensation in turbines has been extensively investigated. The rapid expansion of the flow can cause significant cooling of the flow, leading to potential formation of liquid water. The operating conditions of the turbine and the humidity determine if and when liquid water will be generated. It is one of the challenges faced in the operation of industrial low-pressure steam turbines, where condensation can lead to efficiency losses and mechanical damage.

On the other hand, in IC engine turbochargers, since the exhaust gases are at a very high temperature, condensation is not a common issue, However, the operating temperature of fuel cell turbochargers is relatively much lower (60-100^{o}C), and these turbines are much more susceptible to formation of liquid water. Not a lot of literature is available on this as it is relatively new technology; however, the process of condensation in steam turbines has been studied extensively, and can provide valuable insight into the behavior of humid air in FC turbocharger turbines. Despite many similarities, the key differences between wetness in a steam turbine and a fuel cell turbocharger are [15]:

- The fuel cell turbine works in a much more humid environment, as the fuel cell exhaust gas has a very high moisture content even after being passed through a water separator.
- The pressure ratio of a multistage steam turbine is much larger than that in a fuel cell turbocharger.
- Steam turbines are usually built axially with large diameters, whereas turbines in PEMFC turbochargers are radial, and smaller in size, experiencing much more secondary flow.

It is considered that the turbocharger is placed in the air-supply side, as shown in Figure 2.1. The compressor and turbine are mounted on the same shaft as the electric motor and the turbine assists the compressor. The compressed air goes through a humidifier into the fuel cell stack, as it is important to keep the PEMFC membranes humid for proper functioning of the system. The gas flowing out of the fuel cell stack consists of air, water vapor and liquid water. Most of the liquid water is separated right before entering the turbine. However, the air at the turbine inlet is still very humid, and the expanding flow saturates the gases, and liquid water droplets are formed. This greatly impacts the efficiency of the turbine, as well as causes problems like blade erosion. These effects have been studied by researchers involved in the development of electric fuel cell turbochargers [16–18].

In certain low-pressure steam turbines, the steam enters as dry saturated vapor but exits as two-phase saturated vapor with small droplets of liquid. The formation of these droplets mainly takes place in the blade passages, where the rate of expansion is very high. The heat and mass transfer between the

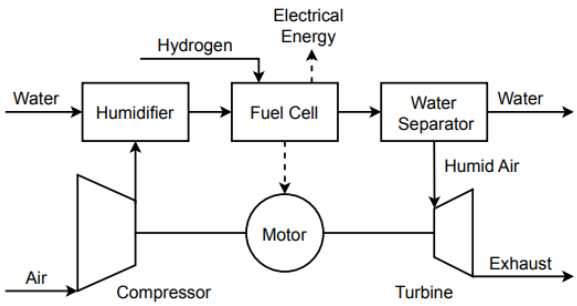

Figure 2.1: Turbocharged air-management system for a PEMFC [18].

two phases can have a strong effect on the flow behavior. The non-equilibrium condensation, being a thermodynamically irreversible process, can bring down the turbine efficiency, and moreover, the flow becomes supersonic in the final stages, leading to complex interactions with the droplet formation process. The condensation process in radial turbines and the issues arising from it are well-researched and a comprehensive overview of these can be found in literature [19–21].

2.1.1. Physical Modelling

Intuitively, the water vapor present should separate out as liquid as soon as the saturation line is crossed during rapid expansion. However, this transition is not immediate and is preceded by the system attaining a metastable equilibrium state, during which small clusters of liquid are formed within the vapor. This process is known as nucleation, and it can occur in one of two ways - homogeneously and heterogeneously, or even both modes simultaneously. Heterogeneous nucleation requires foreign particle or imperfections in solid surfaces, and is encountered frequently in nature.

However, in the absence of any suspended particles, the flow lacks any solid surfaces on which condensation can occur. This surface is provided by molecular clusters, acting as nuclei for the droplets to grow on. This is the process of homogeneous nucleation, which is common in engineering applications, such as supersonic nozzle flows. There is a minimum energy barrier associated with the formation of this new surface, which is much higher in homogeneous nucleation. In the present study, only consider homogeneous nucleation occurring in pure vapor in the absence of foreign particles will be considered.

Understanding the physics behind all the steps leading to nucleation and consequent growth of a droplet of water is key to predicting it numerically in a given setup. The various characteristic aspects of the phenomenon are discussed ahead.

Thermodynamic aspects

Some peculiar properties are observed in pure vapor transitioning into liquid state. From basic thermodynamics, the Gibbs free energy is given by [22],

$$G = U + \frac{P}{\rho} - TS, \tag{2.1}$$

where U denotes the internal energy and S is the entropy. For any set of pressure and temperature, (P, T), the system is in equilibrium if G is minimal. The stability criterion can be expressed by,

$$\left(\frac{\partial^2 G}{\partial T^2}\right)_P < 0 \text{ and } \left(\frac{\partial^2 G}{\partial P^2}\right)_T < 0. \tag{2.2}$$

But,

$$dG = -SdT + \frac{1}{\rho}dP, \text{ and } dS = \frac{C_P}{T}dT + \frac{1}{\rho^2}\left(\frac{\partial \rho}{\partial T}\right)_P. \tag{2.3}$$

Hence,

$$\left(\frac{\partial^2 G}{\partial T^2}\right)_P = -\left(\frac{\partial S}{\partial T}\right)_P = -\frac{C_P}{T} < 0, \tag{2.4}$$

$$\left(\frac{\partial^2 G}{\partial P^2}\right)_T = -\frac{(\partial\rho/\partial P)_T}{\rho^2} = -\frac{\kappa_T}{\rho} < 0. \tag{2.5}$$

where κ_T is the isothermal compressibility, which suggests that the stable state can only be attained if κ_T and C_P are positive. Figure 2.2 shows the projection of the state curves along the $(P, 1/\rho)$ plane, along with isotherms within and beyond the critical point. The slope of any isotherm in the plot is given by,

$$\left(\frac{\partial P}{\partial(1/\rho)}\right)_T = 1/\left(\frac{\partial(1/\rho)}{\partial P}\right)_T = 1/\left(-\frac{(\partial\rho/\partial P)_T}{\rho^2}\right). \tag{2.6}$$

From this it is seen that the second term in (2.5) is the reciprocal of the slope of the isotherms shown in Figure 2.2. Hence, it implies that any fluid will be stable as long as its isotherm exhibits a negative slope, i.e., positive compressibility κ_T.

The curve abc represents the portion of the isotherm within the coexistence curve (bold line). Above the critical point, the slope of isotherms is always positive, making the isothermal compressibility always negative. If a supercritical fluid cooled slowly along critical density, its compressibility will be seen to become infinite at the critical point as the slope is 0. When the temperature dips further, the fluid enters the two-phase zone. At point b, the isotherm shows a positive slope, exhibiting negative compressibility and a one-phase fluid under that condition would be mechanically unstable. Thus, the phase separation occurs.

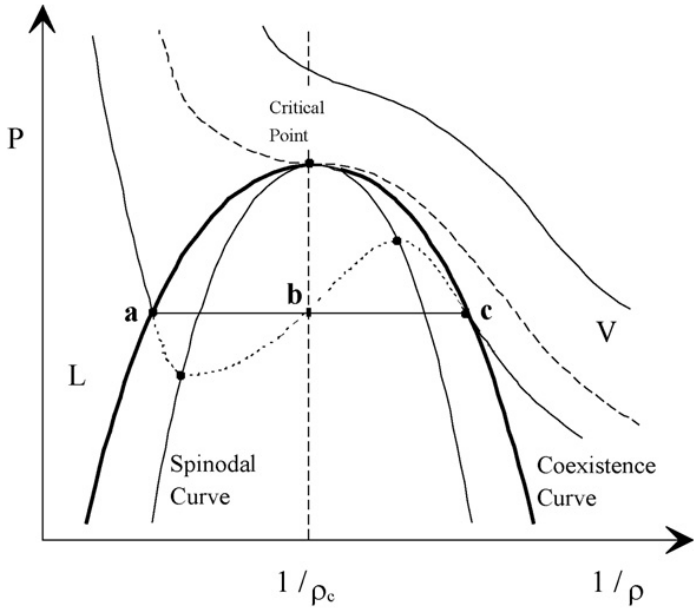

Figure 2.2: Coexistance and spinodal curves [23].

However, some parts of the isotherms inside the dome have a negative slope. These segments extend up to the spinodal line, represented by the thin line in Figure 2.2. This line is obtained from the loci of all the points at which the slope changes sign inside the coexistence curve. The fluid is locally stable in the region bounded by these curves, but its Gibbs potential is not minimum among all possible states at that temperature and pressure. This is called a state of metastability, which implies that the system is immune to small fluctuations in the thermodynamic variables, but will evolve into the state corresponding to the global minimum of free energy.

To attain this state, a barrier (local maximum of free energy) must be crossed, which can be overcome by a fluctuation in the local order parameter (here, density) [24]. After a certain degree of supersaturation, clusters of various sizes are nucleated spontaneously due to these thermal fluctuations. If they reach a critical radius, it marks the onset of the nucleation rate, as they grow into liquid droplets. The ones that don't attain the required size, shrink and disappear.

In the metastable equilibrium state, the standard thermo-fluid relations can be applied to the flow. However, once homogeneous nucleation starts, the total mixture will not be in thermodynamic equilibrium, as the droplets grow actively, and there is an interface exchange of mass, momentum and energy. The formation and growth of liquid droplets is associated with the release of a significant amount of latent heat, which leads to compressible disturbances in the flow, often misleadingly termed as a 'condensation shock' [25–27]. The heat release decreases the extent of subcooling and slows down the droplet growth process, and alters the thermodynamic parameters, eventually reverting the system back into a stable equilibrium state. If a very high amount of heat is released, there is the possibility of thermal choking, which is marked by the existence of normal shocks, and the flow is deemed supercritical.

Theory of Homogeneous Nucleation

The theory of homogeneous nucleation has evolved along two branches [28]. The classical thermo-kinetic approach has been explored widely. It follows the idea that the transition in state is the result of fluctuations and that pure vapor or liquid in the absence of foreign particles behave as if the condensation and freezing point did not exist, hence exhibiting supersaturation and supercooling [26, 29].

The second approach is built on the principles of statistical mechanics, that intends to do away with the uncertainties found in the classical theory [30, 31]. Furthermore, numerous hybrid analytical theories have been developed [32], as well numerical methods like Monte Carlo and molecular dynamics simulations have been deployed to study phase change phenomena [33, 34]. However, even after a century of rigorous research, a definitive nucleation theory has not been agreed upon. Still, for most engineering applications, the predictive capability of the classical theory of homogeneous nucleation developed by Volmer [35], Farkas [36], Becker and Döring [37], along with a few modifications, is reliable [28].

For the formulation of this theory, a simple case is considered at first where a nucleus size is a cluster of molecules. It is assumed that [38]:

- Spherical clusters (radius r) can grow or contract by gaining or losing a molecule.
- On collision with the cluster, the molecule gets attached to it.
- There is no memory of past events, i.e., consecutive events that change the size of the cluster are not correlated.

The Gibbs' free energy of these clusters are approximated macroscopically to simplify the dynamics. The process of the formation and growth of the droplets can be understood by breaking down the process into different steps contributing to the change in the Gibbs' free energy ΔG taking place within the supersaturated vapor [39]:

1. The first n molecules are isolated from the steam. They create the main nucleus, which does not involve any change in Gibbs' free energy,

$$\Delta G_1 = 0. \tag{2.7}$$

2. The steam (assumed calorifically perfect) expands isothermally ($dT = 0$) from pressure P to saturation pressure $P_{sat}(T)$. Let the specific volume of the nucleus be v, and the radius of the cluster r. The change in free energy is given by,

$$dg = vdp - sdT = vdp, \tag{2.8}$$

$$dg_2 = \frac{\Delta G_2}{\frac{4}{3}\pi r^3 \rho_l}, \tag{2.9}$$

$$\Delta G_2 = \frac{4}{3}\pi r^3 \rho_l \int_P^{P_s} \frac{1}{\rho_v} dp = -\frac{4}{3}\pi r^3 \rho_l R T_v \left[ln(S)\right], \tag{2.10}$$

where, $S = \left[\frac{P}{P_{sat}(T_v)}\right]$ denotes the supersaturation ratio. From now onwards, the symbol S will refer to the supersaturation ratio.

3. The n molecules are condensed from the superheated vapor at pressure P. This is not associated with any change in free energy, as the phases co-exist at this pressure.

$$\Delta G_3 = 0. \tag{2.11}$$

4. The n molecules condense at $P_s(T)$ and a droplet of radius r comes into existence. The new surface area created is $A = 4\pi r^2$, leading to,

$$\Delta G_4 = 4\pi r^2 \sigma, \tag{2.12}$$

where σ is the surface tension of the droplets.

5. The droplets are then isothermally compressed from the saturation pressure to the original vapor pressure P. The liquid is assumed incompressible, and hence the liquid phase volume and droplet radii will not change. The free energy change is,

$$\Delta G_5 = \frac{4}{3}\pi r^3 (P - P_{sat}(T_v)). \tag{2.13}$$

This contribution is very small relative to the other ones, and can be neglected.

Summing up, the total change in free energy can be given by,

$$\Delta G = -\frac{4}{3}\pi r^3 \rho_l R T_v \left[ln(S)\right] + 4\pi r^2 \sigma. \tag{2.14}$$

When the supersaturation ratio S is greater than 1, the first term retains the negative sign. The second term is always positive as it is associated with the creation of the liquid bulk surface. The free energy change is dependent on radius r of the droplet. The plot of ΔG vs. r is shown in Figure 2.3. for various supersaturation ratios. For any $S > 1$ curve, there is a local maximum ΔG^*. This radius at which this local maximum is obtained, is called the Kelvin-Helmholtz or critical radius r^*. Any droplet with a radius exceeding the value r^* can reduce the free energy further by agglomerating more molecules. On the other hand, if the radius is any less, it shrinks and evaporates.

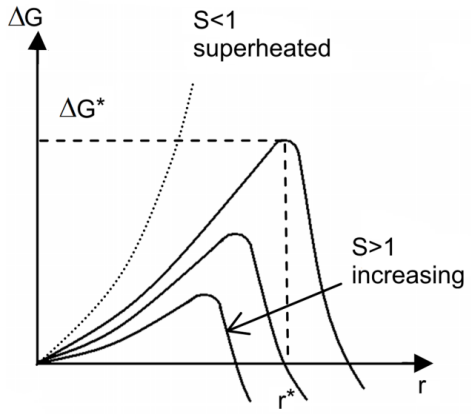

Figure 2.3: Variation in free energy change for different supersaturation ratios [39].

The value of critical radius r^* can be found by differentiating the expression for ΔG,

$$r^* = \frac{2\sigma}{\rho_l R T_v ln(S)}. \tag{2.15}$$

The corresponding ΔG^* is the free energy barrier, which decreases with a rise in the supersaturation ratio,

$$\Delta G^* = \frac{4\pi r^{*2}\sigma}{3} = \frac{16\pi\sigma^3}{3(\rho_l R T_v ln(S))^2}. \tag{2.16}$$

The clusters that reach the critical radius are in a state of unstable equilibrium with the vapor. A statistical distribution, similar to the Boltzmann law, can be used to estimate the frequency of fluctuations leading to the formation of such clusters. This comes under the classical nucleation theory [40, 41]. The main aim of the development of this theory was to provide an expression to estimate

the nucleation rate per unit volume and time (J), and the research surrounding it was supported with numerous experiments as well, mostly in nozzles.

The above discussed parameters can be used to deduce the expression for the classical nucleation rate J_{CL} per unit volume,

$$J_{CL} = q_c \frac{\rho_v^2}{\rho_l} \left(\frac{2\sigma}{\pi m^3} \right)^{1/2} \exp\left(-\frac{4\pi r^{*2} \sigma}{3 k_B T_v} \right). \tag{2.17}$$

The complete derivation is included in Appendix A. The nucleation rate is negligibly small at low values of supersaturation ratios, but grows dramatically with an increase in subcooling $\Delta T = T_{sat} - T_v$.

Since the advent of this theory, several refinements have been added to it. Some of them are discussed below.

1. Courtney's correction: The first correction was suggested by Courtney [42], who remarked that the classical theory had not accounted for the partial pressure of the clusters, and reduced the expression (A.10) for J_{CL} by a factor S or the supersaturation ratio. This ensured consistency with the law of mass action.
2. Condensation coefficient: The value of q_c appearing in (A.10) was estimated to be close to 1 by some authors [43]. Later, Mills [44] conducted experiments that led him to conclude that the interfacial heat transfer resistance was insignificant and the condensation coefficient could have values in the range of 0.45 to 1. The value of unity is mostly associated with condensation on large surfaces. For the formation of clusters q_c is usually smaller than unity.
3. Non-isothermal correction: The vapor and liquid conditions were assumed to be isothermal under the classical theory. However, in reality, the condensation of vapor into liquid nuclei releases some latent heat and the effect of this is realized by gas kinetic collisions is the surrounding vapor, instead of conduction. The reason for this is that the size of the critical nuclei is smaller than the mean free path length. This thermal non-equilibrium between phases affects the nucleation rate, and a correction was introduced by Kantrowitz [45], with the non-isothermal factor ϕ,

$$J_{niso} = \frac{J_{CL}}{1 + \phi}, \tag{2.18}$$

where,

$$\Phi = \frac{2(\gamma - 1)}{\gamma + 1} \frac{L}{R T_v} \left[\frac{L}{R T_v} - \frac{1}{2} \right]. \tag{2.19}$$

Here, γ is the ratio of specific heats for the vapor. The expression for J_{niso} is valid only for stationary nuclei, but can be applied to both steady and unsteady flows when the time scale of the condensation process is smaller than that of the flow.

The characteristic timescale of the condensation process is in the range of $\tau = 10^{-7}$ to 10^{-6} s, and typically, in nozzle flows, the cooling rate leads to a temperature decrease of less than 1 K in a microsecond. Furthermore, the characteristic timescale for nozzle flows is around 10^{-3} s, which is about three orders of magnitude higher than that of the condensation phenomena. Thus, the nucleation rate obtained under the steady state assumption in (2.19) is a good approximation and can be applied to unsteady flows safely.

2.2. Realization of Multiphase flows

Turbulent dispersed multiphase flows are complex to simulate, because of the stochastic nature of both the dispersed and the carrier phases. In the field of fluid mechanics, there are two broad ways to describe motion, the Lagrangian approach and the Eulerian approach. The schemes used for representing multiphase flow fields are broadly classified as Euler-Euler (EE) or Euler-Lagrange (EL).

2.2.1. Euler-Lagrange (EL) approach

In the Euler-Lagrangian approach, the trajectories of the individual particles of the dispersed phase are tracked in a Lagrangian manner. The motion of each element is predicted in accordance with

Newton's second law and information about the mass, momentum and energy history of the particles can be obtained. One of the most important assumptions for this approach is the treatment of the dispersed elements as point masses which should be much smaller than the dimension of the numerical grid. The relevant forces in the field govern the motion of the particles, which can be modeled by using the appropriate resistance coefficients. It is essentially a hybrid approach where the continuum carrier fluid flow on a fixed Eulerian grid is coupled with Lagrangian discrete particle tracking.

The size of each particle is independent, and thus poly-dispersity (variation in size throughout the system) can be handled easily. The scheme can be either one-way coupled or two-way coupled. In one-way coupled simulations, dispersed elements are influenced by the carrier fluid, but not vice-versa. This is appropriate for flows with fewer particles. These descriptions may be combined with any type of simulations, such as DNS (Direct Numerical Simulation), LES (Large-Eddy Simulation) and RANS (Reynolds Averaged Navier-Stokes). The major advantage of this type of formulation is that the particle size distribution can be incorporated and elementary processes can be integrated into it, such as wall collisions, inter-particle collisions and agglomeration.

In order to model non-equilibrium condensation in turbines, these methods with explicit integration of droplets were applied to both 2D cascade problems over turbine blades as well as the full 3D Navier-Stokes equation for the low-pressure stages, quantifying the complex transonic fields and losses [46, 47]. EL is usually employed for flows with less dense particle loading [48], and the large computational resources required makes it less popular in industrial settings.

2.2.2. Euler-Euler (EE) approach

In this approach, the phases are considered to be mixed on length scales smaller than resolvable, and both phases co-exist everywhere in the domain. This concept is called 'interpenetrating continua'. Since the volume of one phase cannot be occupied by another, the concept of phasic volume fraction is introduced. These fractions are treated as continuous functions of space and time, with their total sum always equaling one. The mass, momentum and energy conservation equations are phase-averaged in each grid cell, leading to separate conservation equations coupled by interaction terms [49].

Using the Lagrangian approach becomes computationally challenging when large 3D systems are to be modeled, especially transient flow behavior [50]. This led to the focus on the development of Euler-Euler schemes [51, 52], as they can be naturally integrated into parallel computing for large-scale flows, as the phases share the same grid and there are no load imbalances since moving particles are absent [53]. However, the volumetric averaging of the dispersed phase equations leads to a relatively less accurate estimate of the flow behavior with respect to EL methods. This is more prominent in the nucleation zones, where the flow conditions change dynamically. Moreover, the contribution of the discretization error needs for be accounted for carefully, as it makes it harder to predict the thermodynamic losses [54–56].

In the EE models, the movement of fluid from one cell to another is not explicitly tracked, meaning that the behavior of the fluid in its previous location does not need to be known. This characteristic enables the formulation of equations in time-marching form and simplifies the extension to three dimensions. However, because the solution can vary rapidly over short distances, advanced numerical schemes are required to handle these changes effectively [51].

One of the ways to model condensing flows using this formulation is to modify the source terms in the governing equations as per the rate of heat and mass transfer between phases. The other approach is to solve the governing equations for the mixture along with a volume fraction equation for the liquid phase, and to algebraically model the relative (drift) velocity of the phases. In this study, the Euler-Euler mixture methodology in ANSYS Fluent will be employed, which is discussed ahead.

2.3. Computational Fluid Dynamics (CFD) studies

Computational Fluid Dynamics (CFD) has been a very important tool to resolve the physics of flow and heat transfer occurring in turbulent multiphase flows. The inter-phase transfer mechanisms are challenging to capture when there is phase change involved. This section examines significant computational efforts to predict condensing flows in nozzles and turbines, focusing on numerical methodologies

and critical findings in the literature.

2.3.1. Flow in Nozzles

Nozzles are a popular choice for testing and validating such phase change models, as they provide a simplified respresentation of the same kind of energy conversion found in a turbine. Available Euler-Euler methods can be classified into two types - the E-E Source term model in which the source terms in the governing compressible transport equations can be modified to incorporate inter-phase transfer terms, along with additional equations for liquid mass fraction and droplet number; and the E-E Mixture model which directly solves governing equations formulated for the mixture, weighted by the volume fractions of the phases.

Edathol et al. [57] tested the performance of both these models for wet steam flow in different nozzles in ANSYS Fluent, the comparison of the performance of the two models employed is shown in Figure 2.4. Mostly, the prediction of pressure, droplet size and the location of onset condensation were similar for both models and matched well with experimental data from the Moore B nozzle tests [58]. The EEM model was found to be more prone to the expansion and compression waves, resulting from the nozzle profile discontinuity at the throat.

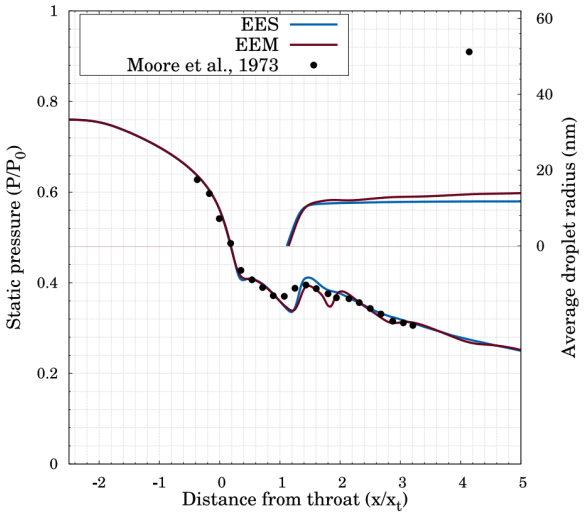

Figure 2.4: Profiles of static pressure normalized with inlet total pressure ($P/P0$) and averaged droplet radius (r) along the centreline for the Moore B nozzle, as predicted by the Euler-Euler Source (EES) term and the Euler-Euler Mixture (EEM) term models formulated by Edathol et al. [57], against experimental data.

Post and di Mare [59] also performed the same comparison between the two types of E-E models, reiterating the importance of fully Eulerian methods for complex 3D flows. They used a density-based OpenFOAM solver, and the advantage of using the E-E source term model was highlighted as the fluxes are calculated using gas-phase properties only, avoiding the need to recompute mixture-averaged fluxes as wetness evolves.

The International Wet Steam Modeling Project was undertaken in 2015 to develop a comparative database for different computational methods and their predictive capability for condensing steam flows in commonly used nozzles. Various institutions provided their computations for some benchmark nozzles. Starzmann et al. [60] compiled these results in their work, which includes the results of numerical predictions for each of the nozzles presented against experimental results. The nozzle designs should ideally be such that they provide a 1D flow free from expansion and compression waves. However, some nozzle designs have drawbacks - the Moore B nozzle has considerable 2D effects and the Moses and Stein nozzle has a narrow throat and the condensation is affected by the boundary layer. Thus, a new nozzle, now known as the Starzmann nozzle was developed to mitigate boundary layer effects.

Both Euler-Euler and Euler-Lagrange methods were used by participants, applied through various in-house and commercial codes. Analysis of the results showed that using the classical theory of ho-

mogeneous nucleation along with a few corrections provide good agreement with experiments. The Euler-Lagrange methods gave a better estimate in modeling the droplet size; the monodispersed models (that assume all droplets are the same radius at any point of time) tend to overestimate the size. The EES and the EEM models were observed to perform similarly, and no general consensus was reached regarding the "best" model.

2.3.2. Flow in Steam turbines

The Euler-Euler framework has been widely used to capture condensation phenomena in axial turbine cascades. Yousif et al. [61] investigated spontaneous condensation in 2-D transonic flow of steam in a low pressure axial turbine cascade both numerically and experimentally. The influence of exit pressure on the location and intensity of condensation was studied using the commercial ANSYS Fluent solver, which solved the 2-D compressible Navier-Stokes equations for the flow using a density-based algorithm, along with the transport equations for the liquid mass-fraction and number of droplets per unit volume. Fair agreement between the computational and experimental results were found.

Other works include Francesco et al. [62], in which the fully Eulerian Mixture model approach was used in ANSYS Fluent to solve the flow over axial turbine blade profiles. Spontaneous nucleation and condensation was captured, and the results were validated against experiments. The pressure rise due to the condensation shock showed some deviation from the experimental data, which shows that some accuracy is compromised due to the volume averaging done in Euler-Euler models. Yeoh and Tu [63] provides a comprehensive understanding of the computational techniques developed for turbulent multiphase flows, and insights into interpreting CFD results.

Elmekawy and Ali [64] utilized the Euler-Euler wet steam (EES) model available in ANSYS Fluent to predict the transient flow and liquid generation in the last stage of a steam turbine. Three blade trailing edge shapes were adopted to study how it impacted condensation, leading to the conclusion that the sharp edge provided the best flow attachment. The flow was in the supersonic regime and two shocks were observed in the flow, a condensation shock and an oblique shock, which interact. It was concluded that the ANSYS Fluent software could predict phase change in a complicated geometry with acceptable accuracy.

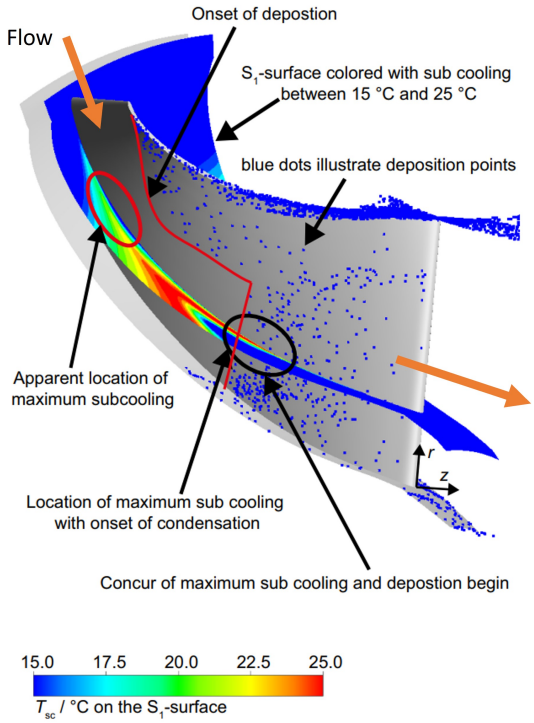

Figure 2.5: Points of subcooling and droplet deposition in the flow passage of a radial turbine from the CFD study by Schuster et al. [65]; the legend shows subcooling values.

There have also been CFD studies conducted on radial turbine models, although fewer. Schuster et al. [65] simulated complex two phase flow involving gas, liquid droplets and liquid wall film through a radial turbine impeller, using Ansys CFX with some in-house modules integrated into the solver. An Euler-Lagrange formulation was used, and to use the computational resources efficiently, the problem was subdivided into more basic problems. The carrier gas phase, a mixture of air and steam was solved in Eulerian form, and the droplets formed were tracked in a Lagrangian frame, incorporating the gas-liquid interactions. These droplets got deposited and formed a film, which was governed by the turbulent flow and the Brownian motion of the droplets near a wall.

The points of subcooling and the droplet deposition on the suction side of a blade is shown in Figure 2.5. The subcooling was seen to increase up to the middle of the passage after the initial expansion. The point of maximum subcooling was reached, where the most number of droplets also deposited. Further along the passage, after condensation starts, the subcooling decreases rapidly due to the release of latent heat into the flow. They concluded that the deposition of droplets starts at the point of maximum subcooling.

2.3.3. Fuel-Cell turbocharger turbines

Apart from steam turbines, there has been some research in the field of condensation in fuel cell turbocharger turbines. Wittmann et al. [15] investigated formation of liquid water in FC turbine passages when humid air from the fuel cell exhaust is passed through the impeller. Several studies by the same research group were conducted as part of the ARIEL ((Charging for Fuel Cell Systems by Interdisciplinary Electric Air Compressors) project [15, 17, 18]. The Discrete Phase Model (DPM) module of ANSYS Fluent was used for this, making the formulation of the dispersed phase Lagrangian. The only forces on the particles considered was the spherical drag, and the condensation was triggered using a minimum value of the nucleation rate. If the nucleation rate exceeded a certain value in any grid cell, the droplets were initialized. The numerical model was validated with some supersonic nozzle test cases.

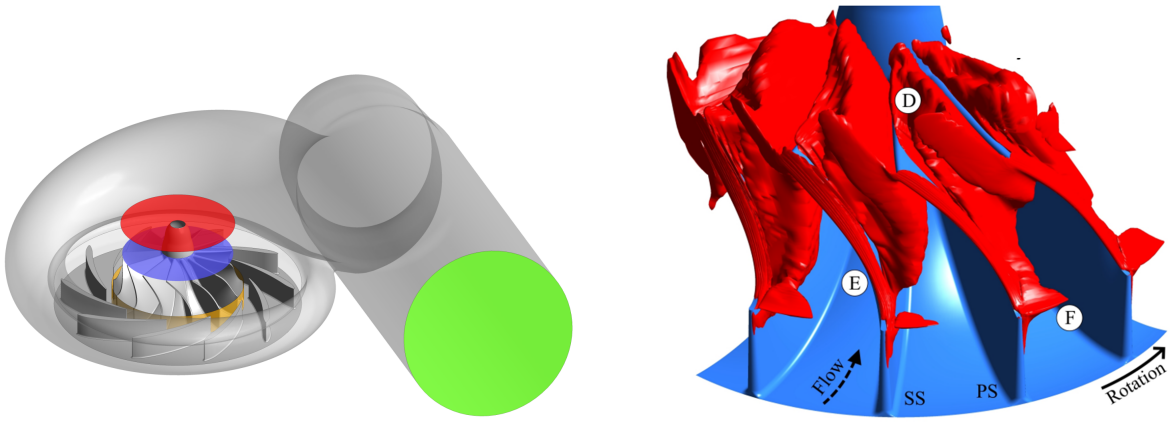

(a) (b)

Figure 2.6: (a)Computation domain for radial turbine: inlet (green), outlet (red), frozen-rotor interface (orange), plane of analysis (blue) [18]; (b) Isocontours of the locations where a critical nucleation rate is reached and condensation starts [17].

In order to apply the model to a full radial turbine, a frozen rotor approach was used, in which the relative motion between rotor and stator is approximated by imposing a ”frozen” interface where flow variables (e.g., pressure, velocity) are interpolated between rotating and stationary domains to avoid computational expenses, and a steady-state problem is solved [66]. The turbine setup used is shown in Figure 2.6a, showing the different planes, namely, the inlet, outlet, frozen rotor interface, and the plane where the flow is analyzed. The effect of inlet humidity and pressure ratios on the intensity and location of onset of condensation were studied.

It was observed that the nucleation started near the rotor entry in the tip gap, and continued into the blade passage as shown by the red isocontours in Figure 2.6b. Condensation had a significant

effect on the thermodynamics of the turbine, affecting the entire air-management system. However, no experimental data was available for the turbine to validate the results. Additionally, the physical effect of condensation on the turbine, namely, droplet induced erosion, was studied [67].

A study conducted by Mao et al. [68] to analyze condensation phenomena in a fuel cell turbocharger turbine employed an Euler-Euler Source (EES) term approach. Their methodology consisted of solving equations for the liquid mass fraction and number of droplets per unit mass, in addition to the conservation equations. Experiments were conducted by the group to provide a more comprehensive validation. Since the results provided were validated, some data from this study is used in the current project for development of the model as well as qualitative validation, which will be discussed in Chapter 4.

So far, no literature has been found employing Euler-Euler Mixture (EEM) methods for the CFD analysis of fuel cell turbocharger turbines, which is a gap this project aims to address.

2.4. Experimental studies

Several experiments have investigated condensation in nozzles and the wet stages of turbines. Initially, the complex nature of the wet steam medium made it difficult to gather satisfactory data, especially empirical data that could be used to tune theoretical models. In the last few decades, sophisticated advances in instrumentation technology and optical techniques [69] have led to reliable and insightful results. Extensive experiments have been conducted, in recent history, on condensing flows in nozzles [70–72]. If properly designed, the nozzles can produce a steady flow that very closely resembles the flow conditions seen in a turbine.

One of the seminal works in the experimental field was carried out by Moses and Stein [73], on a Laval nozzle, which is a type of converging-diverging nozzle. The design was such that the flow could be treated as a steady attached inviscid supersonic expansion, where the flow goes from subsonic conditions at the inlet to supersonic at the outlet. Static pressure measurement and light scattering techniques were used. The captured process is illustrated in Figure 2.7. According to the measurements, the steam expands into the converging section of the nozzle and crosses the saturation line at point 2. The location of this point is dependent on the initial conditions of pressure and temperature. Due to the high expansion rate, the condensate does not immediately appear at 2, but the flow becomes supersaturated to a point 3 where homogeneous nucleation rate increases rapidly and stable molecular clusters are formed. Significant latent heat of vaporization is released to the flow and light scattering is seen at this point, pushing the system to equilibrium again. The droplet growth processes slow down and the flow again expands and cools. The dual measurement proved to be effective as nucleation and droplet growth are coupled at onset, and the data was used to validate important theoretical models such as the Gyarmathy [74] and Hill [75] droplet growth laws.

White et al. [76] conducted experiments on condensing transonic steam flow in a stationary cascade of axial turbine blades. The use of large blades facilitated more extensive instrumentation, capturing data up to the trailing edge where condensation was prominent. The Schlieren photographs show the relative positions of the suction side and the pressure side trailing edge shock waves (S_S and S_P, respectively) and the condensation front S_C for one of the cases in Figure 2.8. On the suction side, large nucleation rates are found, whereas, on the pressure side, the onset of condensation is delayed due to the rise in temperature associated with the trailing edge shock wave, yielding fewer but bigger droplets. This is shown in Figure 2.8 as the Wilson points od maximum subcooling (black dots).

The results obtained from these tests showed that with the inlet and outlet pressure conditions maintained, the surface pressure distributions and the zone of onset of condensation does not change much, contrasting to the earlier discussed work of Moses and Stein [73]. This is explained by Bakhtar et al. [77] as due to the effect of sudden increase in rate of expansion as the flow approaches the throat, followed by a sudden drop, which is often misleadingly termed as 'condensation shock'. The zone of rapid condensation was also somewhat insensitive to the overall pressure ratio [78]. Moreover, a significant drop (up to 5%) in the thermodynamic efficiency was reported [79].

Numerous databases created from such experimental campaigns have made it possible to validate theoretical models that predict the location and conditions for the onset of condensation, as well as the nature of droplet growth. Next, the numerical modeling of the phenomena will be discussed, which will

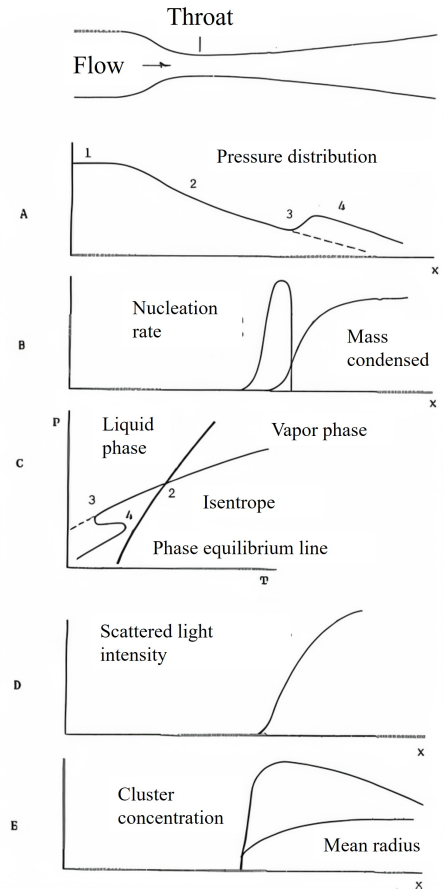

Figure 2.7: The dynamics of condensation measured with pressure (A) and light scattering (D) and other derived quantities [73].

be used in the present work.

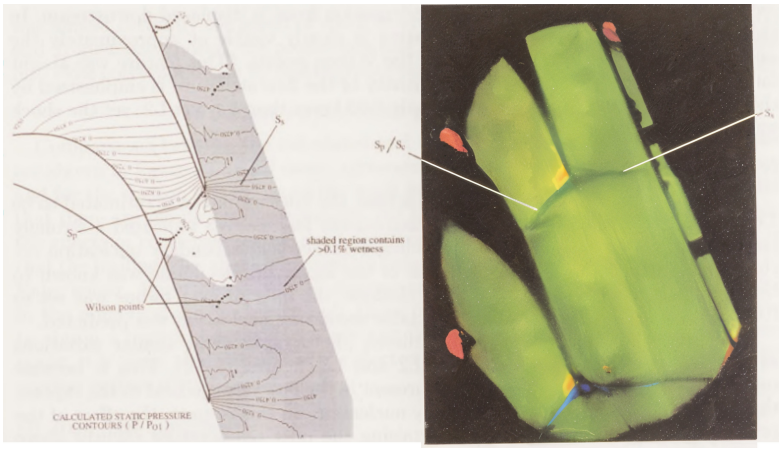

Figure 2.8: Static pressure contours and the Schlieren images of the positions of the suction side and the pressure side shock waves S_S and S_P, respectively; the condensation front S_C coincides with the pressure side shock S_P [76].

2.5. Research Gap

The literature review so far has shown that there has been extensive research carried out on the topic of non-equilibrium condensation using the theory of homogeneous nucleation in steam turbines. Limited literature is available on condensation in fuel cell turbocharger turbines, as the technology is relatively

new. The Euler-Lagrange formulation has been used to computationally predict the flow and heat transfer characteristics for the nucleation of droplets in the FC turbocharger turbines Wittmann et al. [18, 67], however, there are no known studies done in the Euler-Euler Mixture model framework. The accuracy-cost tradeoff of the two methods have been already discussed. In this thesis, we will understand the physics of non-equilibrium condensation in fuel cell turbocharger turbines, and extend the knowledge we have from the Euler-Euler CFD studies on steam turbines to computationally evaluate and validate the flow characteristics.

2.6. Research Questions and Objectives

The literature survey has led us to identify a gap in research in this domain, which brings us to the research questions:

1. Can the Euler-Euler Mixture method (which uses volume averaging to solve the flow field and has no discrete particles) accurately match the results of more elaborate and sophisticated Euler-Lagrange methods for the particular flow conditions where the turbine operating temperature is low and the system is prone to condensation?
2. How do some critical parameters such as the relative humidity, pressure ratio and rotational speed affect the degree of condensation?
3. What are the effects of the latent heat release on the turbine efficiency?

Based on the questions, our plan and objectives for the thesis can be defined as follows:

- Use an Euler-Euler method in ANSYS Fluent and incorporate a UDF (User-Defined Function) to simulate condensation due to flow expansion in a Moore B nozzle.
- Validate the model used against experimental data from Moore B nozzle tests.
- Use the same model to simulate condensation in flow through the turbine rotor.
- Perform parametric studies on how the location and intensity of the condensation are impacted by changes in inlet conditions.
- Determine how the turbine efficiency is impacted due to liquid generation and latent heat release.

3

Methodology

3.1. Computational Setup of Validation case

Experimental data is not available for the condensing turbine flow under conditions similar to those in a fuel cell turbocharger. Thus, for validation of our model, the flow is analyzed for a benchmark case encapsulating the relevant physics, such as a Moore B nozzle. Converging-diverging nozzles are considered to be representative of the flow through a turbine, and are widely used for the validation of models predicting such flows. The experiments conducted by Moore [58], in a wet steam tunnel, investigated several nozzles with different designs. The nozzle B tested by them had a large throat and offered a high expansion rate. Superheated pure steam was passed into the test section and the static pressure and the droplet radii were measured. The pressure measurements were made from tappings along the centreline of the nozzle. Once condensation started just downstream of the throat, the radius of the droplets formed along the centreline was also recorded using optical methods.

For our validation study, a 2D model of the same dimensions as the nozzle from the experiment is used, to represent planar flow along the centre plane. The nozzle geometry is shown in Figure 3.1. The dimensions are as follows:

Coordinate Location [m]	Point A	Point B	Point C	Point D
x (horizontal)	−0.25	−0.2	0	0.5
y (vertical)	0.0563	0.0563	0.05	0.072

Figure 3.1: Sketch of the Moore B nozzle geometry, with the reference points coordinates presented in the table.

To save computational costs, the 2D Cartesian model is used instead of a 3D geometry. Wang et al. [80] proved that the 2D Fluent solver is sufficiently accurate and it is not essential to use a 3D solver for the simulation.

3.1.1. Meshing

Meshes can be broadly classified into two categories:

- Structured mesh: With identical grid-like cell arrangement, it is effective in simpler geometries and harder to implement for more complex one. The cells typically have higher quality and lower skewness, leading to faster convergence and less numerical diffusion.

- Unstructured mesh: These types of meshes consist of irregularly shaped cells (e.g., tetrahedrons) and have good adaptability, as they can accommodate complex geometries. There is higher numerical diffusion and they require more computational resources, causing delayed convergence.

The choice between the two types of meshes depends on various factors, such as the complexity of the geometry and the computational resources available. In this case, for a planar nozzle geometry, a structured mesh is used as shown in Figure 3.2, consisting of 6795 elements. It is generated in ANSYS meshing. The turbulence model utilized is $k-\omega$ SST, with wall functions to model the boundary layer. The average $y+$ is about 10. It is not attempted to resolve the boundary layer here to save on computational time, as the phenomena of interest (condensation) take place in the core of the nozzle and it is not our objective to accurately estimate effects like drag or heat transfer at the walls.

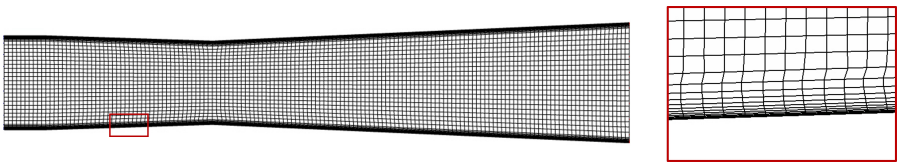

Figure 3.2: Structured mesh for 2D Moore B nozzle along with mesh refinement near the boundaries.

3.1.2. Boundary conditions

The boundary conditions imposed in ANSYS Fluent were the same as those with which the tests were undertaken, in order to reproduce the flow behavior. They are as follows:

Parameter	Value
Inlet Total Temperature	358.1 K
Inlet Total Gauge Pressure	25000 Pa
Outlet Condition	5000 Pa, 300 K
Wall Condition	No-Slip, Adiabatic

Table 3.1: Boundary Conditions for the Moore B nozzle.

The initial conditions are computed from the inlet, and pure steam is used as the working fluid. The steam is considered to be an ideal gas and the properties are calculated as functions of the local conditions using a User-Defined Function (UDF).

3.2. Computational Setup of Turbine

The main geometry of interest for this project is that of the radial turbine used in a fuel cell turbocharger. The domain consists of three parts:

- the inlet zone consisting of the inlet wall and the scroll,
- the rotor zone consisting of the hub, turbine wheel and the shroud, and
- the outlet zone with the outlet and the duct leading to it.

The scroll carries the fuel stack exhaust gas, which is a mixture of air and steam, to the rotor. This turbine has no stator vanes, and the humid air enters the rotor wheel radially and leaves axially from the top. The long cylindrical outlet shaft is provided so that the end effects are not felt near the rotor. The geometry of the full setup is shown in Figure 3.3, along with a close-up of the rotor used.

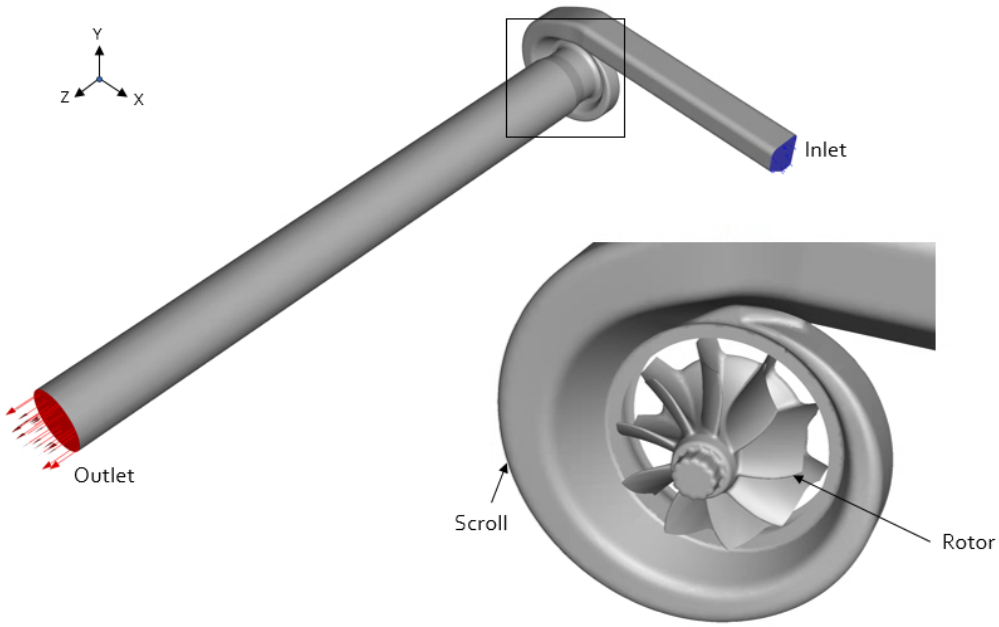

Figure 3.3: The turbine geometry with a close-up of the rotor wheel.

3.2.1. Meshing

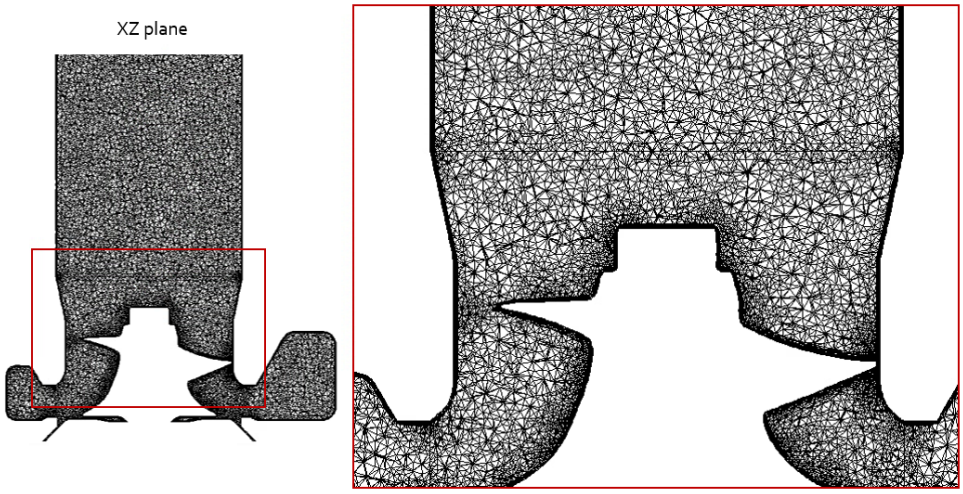

Figure 3.4: An XZ plane slice (side view) passing through the turbine axis, showing the turbine rotor zone mesh shown on the plane section.

For meshing the problem geometry, ANSYS Meshing was used. The mesh is a standard mesh that was developed by the MTEE team. It is a highly complex topology with ample curvature and many sharp edges (e.g., blade tips), and hence, an unstructured mesh made up of tetrahedral elements is chosen. Tetrahedrons have smaller volume than other unstructured grid elements like polyhedral cells, and can define the profile around edges and corners with greater ease and lower skewness, although that means the number of elements required to mesh the same geometry is higher.

A grid independence study to ensure the robustness of the mesh used is presented in the next chapter. Figure 3.4 shows the increased refinement of the grid in the rotor zone as compared to the scroll and the outlet duct, which will be the primary focus of our flow analysis. It is important to capture flow gradients accurately in this region in order to predict the areas where phase change is more likely to occur, especially between the blades. The mesh shown in Figure 3.5 is along the XY plane section,

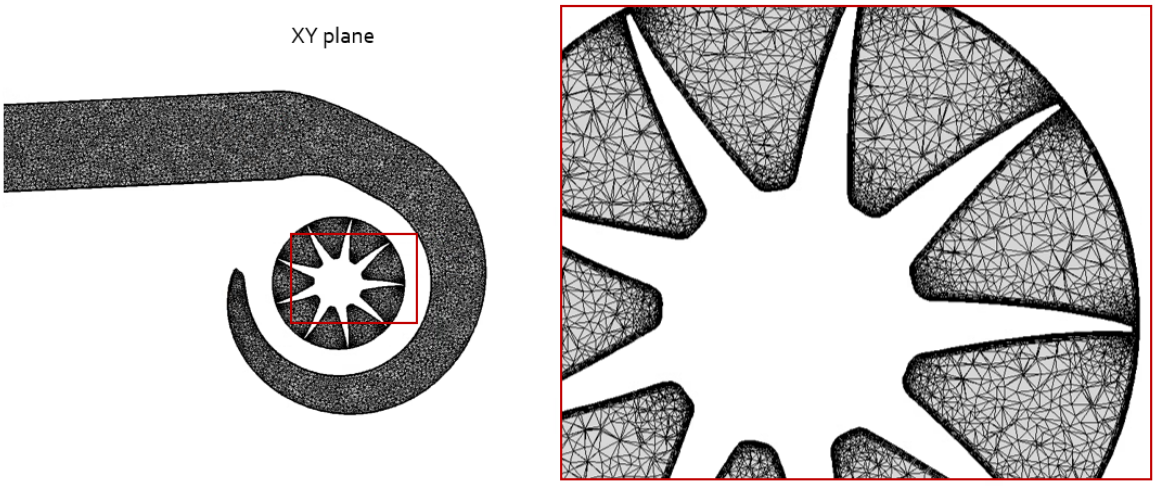

Figure 3.5: An XY plane slice (top view) passing through the turbine axis, showing the turbine rotor zone mesh shown on the plane section.

showing the refinement around the blades up to the tip clearance.

The number of elements used is 9.6 million. The boundary layer is usually not resolved for complex turbomachinery flows, and the $k-\omega$ SST model is a popular choice, since it can efficiently model the flow near the walls and blades and provide accurate predictions for the far-field. The estimated wall $y+$ ranges from 10 to 90 in this case, making it a wall modeled approach.

3.2.2. Boundary Conditions

The boundary conditions imposed are typical conditions encountered in the operation of a fuel cell turbocharger turbine. The humid air flows through the inlet duct into the scroll and radially enters the rotor blade passages.

There is a preliminary simulation run without condensation, just to record the temperature field. This case is run with a pressure inlet boundary condition. The corresponding mass flow of the humid air is fed into the phase change model enabled simulation with a mass flow inlet boundary condition, as using a pressure inlet in this second case led to divergence.

The flow is compressible so the pressure at the outlet must be specified, so a pressure outlet is assigned, exposed to ambient conditions. The values are as follows:

Parameter	Value
Inlet Temperature	353.15 K
Inlet Mass Flow	0.1269 kg/s
Humidity	70%
Outlet Condition	101325 Pa, 300 K
Wall Condition	No-Slip, Adiabatic
Angular speed	97000 RPM

Table 3.2: Boundary Conditions for the turbine case.

3.2.3. The Frozen Rotor Approach

The rotation of the turbine wheel is modeled using the Multiple Reference Frame (MRF) method, popularly known as the frozen rotor method. It involves a steady state formulation which assigns different rotational speeds to different zones connected by an interface. The velocities and velocity gradients for the moving subdomains are computed relative to those in the stationary domain. The

mesh does not move, and it is equivalent to looking at the instantaneous flow-field in a "frozen" snapshot of the wheel in that position [66].

The interface across which this is applied is shown in yellow in Figure 3.6. Outside of this interface is the scroll which is the stationary frame and inside it lies the moving frame which is the entire rotor zone. MRF models are ideal where there is weak rotor-stator interaction, and in this case, there are no stator vanes, so it is a good choice. It is far less computationally heavy than using a moving mesh approach.

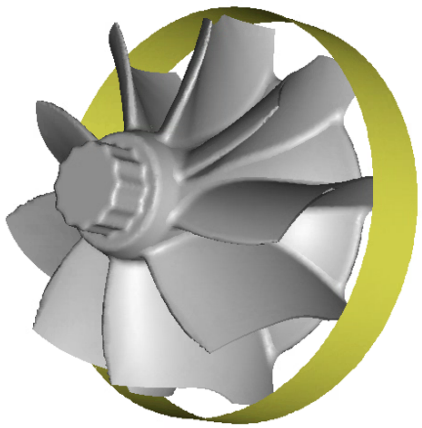

Figure 3.6: The frozen rotor interface (yellow).

3.3. Turbulence modeling

The computational setup has been described for both the validation case (the Moore B nozzle) and the turbine. The instantaneous fluid, momentum, and energy equations governing fluid flow and heat transfer for an unsteady viscous compressible fluid can be given by,

$$\frac{\partial \rho}{\partial t} + \frac{\partial (\rho u_i)}{\partial x_i} = 0, \tag{3.1}$$

$$\frac{\partial (\rho u_i)}{\partial t} + \frac{\partial (\rho u_i u_j)}{\partial x_j} = -\frac{\partial P}{\partial x_i} + \frac{\partial \tau_{ij}}{\partial x_j} + \rho f_i, \tag{3.2}$$

$$\frac{\partial (\rho E)}{\partial t} + \frac{\partial \left((\rho E + P) u_i \right)}{\partial x_i} = \frac{\partial}{\partial x_i} \left(k \frac{\partial T}{\partial x_i} + \tau_{ij} u_j \right) + \rho f_i u_i, \tag{3.3}$$

where,

$$\tau_{ij} = \mu \left(\frac{\partial u_i}{\partial x_j} + \frac{\partial u_j}{\partial x_i} \right) - \frac{2}{3} \mu \delta_{ij} \nabla \cdot \vec{u}. \tag{3.4}$$

To apply Reynolds averaging, all variables can be separated into a mean and a fluctuating component, $\bar{\Phi}$ Φ'. It can be expressed as,

$$\bar{\Phi} \equiv \frac{1}{T} \int_T \Phi(t)\, dt, \tag{3.5}$$

$$\Phi' \equiv \Phi - \bar{\Phi}. \tag{3.6}$$

In case of variable-density flows, it is convenient to define another type of time-averaging called Favre averaging, which is density-weighted. This approach reduces the number of unclosed terms and gives the equations a similar form to the RANS equations. The Favre averaged term $\tilde{\Phi}$ is expressed as:

$$\tilde{\Phi} \equiv \frac{\overline{\rho\Phi}}{\bar{\rho}}, \tag{3.7}$$

with corresponding Favre fluctuation:

$$\Phi'' \equiv \Phi - \tilde{\Phi}. \tag{3.8}$$

Substituting such expressions for the flow variables into these equations, and taking a Favre average, yields the Favre-averaged-Navier-Stokes (FANS) equations [81],

$$\frac{\partial \bar{\rho}}{\partial t} + \frac{\partial}{\partial x_i}\left(\bar{\rho}\tilde{u}_i\right) = 0, \tag{3.9}$$

$$\frac{\partial}{\partial t}\left(\bar{\rho}\tilde{u}_i\right) + \frac{\partial}{\partial x_j}\left(\bar{\rho}\tilde{u}_i\tilde{u}_j + \bar{P}\delta_{ij} - \tilde{\tau}_{ij}^{\text{tot}}\right) = 0, \tag{3.10}$$

$$\frac{\partial}{\partial t}\left(\bar{\rho}\tilde{E}\right) + \frac{\partial}{\partial x_j}\left(\bar{\rho}\tilde{u}_j\tilde{E} + \tilde{u}_j\bar{p} + \tilde{q}_j^{\text{tot}} - \tilde{u}_i\tilde{\tau}_{ij}^{\text{tot}}\right) = 0, \tag{3.11}$$

where,

$$\tau_{ij}^{\text{tot}} = \tau_{ij}^{\text{lam}} + \tau_{ij}^{\text{turb}}, \tag{3.12}$$

$$\tau_{ij}^{\text{lam}} = \mu\left(\frac{\partial\tilde{u}_i}{\partial x_j} + \frac{\partial\tilde{u}_j}{\partial x_i} - \frac{2}{3}\frac{\partial\tilde{u}_k}{\partial x_k}\delta_{ij}\right) \quad , \tag{3.13}$$

$$\tau_{ij}^{\text{turb}} \approx -\overline{\rho u_i'' u_j''} \approx \mu_t\left(\frac{\partial\tilde{u}_i}{\partial x_j} + \frac{\partial\tilde{u}_j}{\partial x_i} - \frac{2}{3}\frac{\partial\tilde{u}_k}{\partial x_k}\delta_{ij}\right) - \frac{2}{3}\bar{\rho}k\delta_{ij}, \tag{3.14}$$

$$q_j^{\text{tot}} = q_j^{\text{lam}} + q_j^{\text{turb}}, \tag{3.15}$$

$$q_j^{\text{lam}} = \tilde{q}_j \approx -C_p\frac{\mu}{Pr}\frac{\partial\tilde{T}}{\partial x_j} = -\frac{\gamma}{\gamma-1}\frac{\mu}{Pr}\frac{\partial}{\partial x_j}\left(\frac{\bar{P}}{\bar{\rho}}\right) \quad , \tag{3.16}$$

$$q_j^{\text{turb}} = C_p\bar{\rho}\mu_t\tilde{T} \approx -C_p\frac{\mu_t}{Pr_t}\frac{\partial\tilde{T}}{\partial x_j} = -\frac{\gamma}{\gamma-1}\frac{\mu_t}{Pr_t}\frac{\partial}{\partial x_j}\left(\frac{\bar{P}}{\bar{\rho}}\right), \tag{3.17}$$

$$P = (\gamma-1)\bar{P}\left(\tilde{E} - \frac{\tilde{u}_k\tilde{u}_k}{2} - k\right) \tag{3.18}$$

.

This is the form that the closures take after the conservation equations are modeled as the mixture equations with the multiphase approach, which will be discussed ahead. Moreover, the steady-state solution is evaluated for this work, since transient effects are not our primary focus here.

3.3.1. Selection of RANS model

Several turbulence closure models are available in Fluent. The $k-\omega$ SST (Shear-Stress Transport) is a popular model, which will be used for our system [66, 82]. The SST $k-\omega$ essentially utilizes the strength of the classic $k-\omega$ near the wall: where it is able to better predict flows under adverse pressure gradients compared to the standard $k-\epsilon$, and blends it with the standard $k-\epsilon$ away from the walls, which is robust in predicting free-shear turbulence and is not sensitive to free-stream conditions unlike the classic $k-\omega$ model. The governing equations for the turbulent kinetic energy k and the turbulent specific dissipation rate ω (which is the ratio of the dissipation rate ϵ to k), are given by,

$$\frac{\partial}{\partial t}(\rho k) + \frac{\partial}{\partial x_i}(\rho k u_i) = \frac{\partial}{\partial x_j}\left(\Gamma_k\frac{\partial k}{\partial x_j}\right) + G_k - Y_k + S_k + G_{b,k}, \tag{3.19}$$

$$\frac{\partial}{\partial t}(\rho\omega) + \frac{\partial}{\partial x_i}(\rho\omega u_i) = \frac{\partial}{\partial x_j}\left(\Gamma_\omega\frac{\partial\omega}{\partial x_j}\right) + G_\omega - Y_\omega + S_\omega + G_{b,\omega}. \tag{3.20}$$

Here,
G: Generation terms (due to mean velocity gradients)

Γ: Effective diffusivity
Y: Dissipation due to turbulence
S: User-defined source terms,
G_b: Buoyancy terms
for k and ω in their respective equations. The description and expressions for these terms can be found in [66]. The formulation of the eddy viscosity term is as follows,

$$\mu_t = \frac{\rho k}{\omega} \frac{1}{\max\left[\frac{1}{\alpha^*}, \frac{SF_2}{a_1 \omega}\right]}, \tag{3.21}$$

where S is the magnitude of the strain rate and α^* is a damping coefficient described as,

$$\alpha^* = \alpha^*_\infty \left(\frac{\alpha^*_0 + Re_t/R_k}{1 + Re_t/R_k}\right), \tag{3.22}$$

where $Re_t = \rho k/\mu\omega$, $R_k = 6$ and $\alpha^*_0 = 0.024$. The other terms are given as,

$$F_2 = \tanh\left(\Phi_2^2\right), \tag{3.23}$$

$$\Phi_2 = \max\left[2\frac{\sqrt{k}}{0.09\omega y}, \frac{500\mu}{\rho y^2 \omega}\right]. \tag{3.24}$$

3.4. Multiphase Flow modeling

In order to carry out the current investigation into condensation in turbines of PEMFC turbochargers, Computational Fluid Dynamics (CFD) tools were employed. ANSYS Fluent is powerful commercial software that is widely used in industrial and academic research. The approaches used for formulating and solving the governing equations will be discussed.

Some of the assumptions involved in the modeling of the flow are:

- Only homogeneous condensation takes place in the bulk of the flow.
- The slip (or, drift) velocity, which is the difference in the velocity of the two phases, is negligible.
- The interaction between the particles of the dispersed liquid phase is not accounted for.
- The humid air is modeled as an ideal gas.

3.4.1. Selection of Multiphase Flow Model

In Fluent, three Euler-Euler multiphase models are available: the volume-of-fluid (VoF) model, the mixture model and the Eulerian model [66]. The VoF model is a surface-tracking technique mostly used for stratified flows where the interface is distinct. The mixture model solves the mixture governing equations, and is suitable for flows in which one phase is dispersed throughout the carrier phase.

The "Eulerian model", in this context is a mathematical model named so by ANSYS (as all the models being discusses adhere to the Eulerian framework), and is more rigorous, as it solves conservation equations for each phase, and coupling between phases is achieved by the use of interphase exchange coefficients. It is computationally much heavier than the other two models as a higher number of equations are being solved. The comparison among the models are given in Table 3.3.

The Euler-Euler Mixture formulation is chosen here to model the multiphase flow field. The non-equilibrium phase change is captured using the Lee (evaporation-condensation) model. The mixture model solves the continuity, momentum, and energy equations for the mixture, along with the volume fraction equation for the secondary phases and algebraic expressions for the relative velocities.

	Volume of Fluid (VoF)	**Mixture Model**	**Eulerian Model**
Phase Representation	Tracks sharp or diffuse interfaces between immiscible fluids.	Treats phases as interpenetrating continua with slip velocity.	Solves separate momentum equations for each phase.
Usage	Best when dispersed phase volume fraction < 0.1.	Best for dilute flows, with evenly distributed particles.	Supports multiple phases and dense flows, useful when dispersed phases are concentrated in some parts
Interfacial Resolution	High (explicit interface capturing).	No interface capturing (averaged properties).	No interface capturing (phases share space).
Momentum Coupling	Single momentum equation, velocity field is shared.	Single momentum equation for mixture and slip velocity correction.	Separate momentum equations for each phase.
Computational Cost	Moderate.	Moderate (simpler than Eulerian).	High.
Typical Applications	Free-surface flows, jet breakup, bubble columns, motion of liquid after dam break.	Slurry flows, dust transport, sprays.	Fluidized beds, dense slurry flows, sedimentation.

Table 3.3: Comparison of Euler-Euler models - VoF, Mixture, and Eulerian in ANSYS Fluent [66].

3.4.2. Governing equations

Let v, l, m denote the vapor phase,the liquid phase and the mixture, respectively. The continuity equation for the mixture is given by

$$\frac{\partial}{\partial t}(\rho_m) + \nabla \cdot (\rho_m \vec{v}_m) = 0, \tag{3.25}$$

where $\vec{v}_m$ is the mass-averaged velocity, and ρ_m is the mixture density,

$$\vec{v}_m = \frac{\alpha_v \rho_v \vec{v}_v + \alpha_l \rho_l \vec{v}_l}{\rho_m}, \tag{3.26}$$

$$\rho_m = \alpha_v \rho_v + \alpha_l \rho_l. \tag{3.27}$$

The mixture momentum equation is given by,

$$\frac{\partial}{\partial t}\Big(\rho_m \vec{v}_m\Big) + \nabla \cdot \Big(\rho_m \vec{v}_m \vec{v}_m\Big) = -\nabla P + \nabla \cdot \Big[\mu_m \Big(\nabla \vec{v}_m + \nabla \vec{v}_m^T\Big)\Big] - \nabla \cdot \left(\sum_{k=1}^{p} a_k \rho_k \vec{v}_{dr,k} \vec{v}_{dr,k}\right). \tag{3.28}$$

It is assumed that the drift phase velocity $v_{dr,k} = 0$ and viscosity mixture μ_m,

$$\mu_m = \alpha_v \mu_v + \alpha_l \mu_l. \tag{3.29}$$

The energy equation for the mixture can be defined as follows,

$$\frac{\partial}{\partial t} \sum_k \Big(\alpha_k \rho_k E_k\Big) + \nabla \cdot \sum_k \Big(\alpha_k \vec{v}_k \Big(\rho_k E_k + P\Big)\Big) = \nabla \cdot (k_{eff} \nabla T + \overline{\overline{\tau}}_{eff} \vec{v}) + S_h, \tag{3.30}$$

where k represents any phase, τ_{eff} represents the effective shear stress tensor and k_{eff} denotes the effective conductivity,

$$k_{eff} = \alpha_v (k_v + k_t) + \alpha_l (k_l + k_t). \tag{3.31}$$

Here, k_t is the turbulent thermal conductivity, defined as per the turbulent model in use. The first 2 RHS terms in (3.30) denote the energy transport due to conduction and viscous dissipation, respectively. S_h represents the volumetric heat source term. Since the phases are compressible, for a phase k,

$$E_k = h_k - \frac{P}{\rho_k} + \frac{v^2}{2}, \tag{3.32}$$

where the sensible enthaply is denoted by h_k for phase k.

In addition to these equations, the turbulence $(k-\omega)$ equations and the ideal gas equation of state are used to close the system. The colume fraction equation and species equations (air/water vapor) are solved.

3.4.3. Volume fraction equation and the Lee Condensation model

The continuity equation describes the mixture as a whole and no information is provided about the distribution of phases due to the phase change. A volume fraction equation is also required for the secondary phase (l) formed due to the system undergoing condensation, which can be expressed as

$$\frac{\partial}{\partial t}\left(\alpha_l \rho_l\right) + \nabla \cdot \left(\alpha_l \rho_l \vec{v}_l\right) = \dot{m}_{vl} - \dot{m}_{lv}. \tag{3.33}$$

In order to model the mass transfer during condensation, the Lee model available in Fluent [83] is used. In (3.33), the terms $\dot{m}_{lv}$ and $\dot{m}_{vl}$ denote the rates of mass transfer due to evaporation and condensation, respectively. The Lee model introduces expressions for the evaporation and condensation mass transfer rate terms, with respect to the saturation temperature T_{sat}, as follows:

If $T_l > T_{sat}$ (evaporation),

$$\dot{m}_{lv} = coeff_1 * \alpha_l \rho_l \left(\frac{T_l - T_{sat}}{T_{sat}}\right). \tag{3.34}$$

If $T_v < T_{sat}$ (condensation),

$$\dot{m}_{vl} = coeff_2 * \alpha_v \rho_v \left(\frac{T_{sat} - T_v}{T_{sat}}\right). \tag{3.35}$$

The empirical coefficients $coeff_1$ and $coeff_2$ [s^{-1}] are time relaxation factors denoting how fast the transfer process is. They are called the evaporation/condensation frequency and can be fine-tuned to match experimental data. Literature shows that the value of $coeff_2$ can range from as low as 0.1 s^{-1} [84] in evaporation to as high as 10^6 s^{-1} [85] for condensation. It can depend on a number of factors (conditions, grid size, etc.), and can even alter for different cases in the same problem. The value of $coeff_1$ is maintained at the default value of 0.1, any evaporation is not accounted for here. In the energy equation (3.30), the source term can be expressed using the same mass transfer rate term and the latent heat of vaporization of water,

$$S_h = \dot{m}_{vl} h_{fg}. \tag{3.36}$$

The T_{sat} is calculated at the given pressure p from the Antoine equation (derived from the Clausius-Clapeyron equation),

$$T_{sat} = \frac{B}{A - \log_{10}(P)} - C, \tag{3.37}$$

where, A, B and C are substance-specific coefficients.

3.4.4. Triggering condensation via User-Defined Functions (UDFs)

Using the Mixture model of ANSYS Fluent alone does not fully capture the condensation shock that results from the release of latent heat once condensation commences: It solves for the homogeneous mixture, and does not model the droplet nucleation and growth. Thus, custom User-Defined Functions (UDFs) are implemented to introduce a triggering factor for condensation to start, which, in this case, is a critical level of subcooling of the air-steam mixture below the local saturation temperature. As discussed previously, in non-equilibrium expansions, condensation does not start immediately when the saturation line is crossed, and usually, there exists a threshold of subcooling that must be reached.

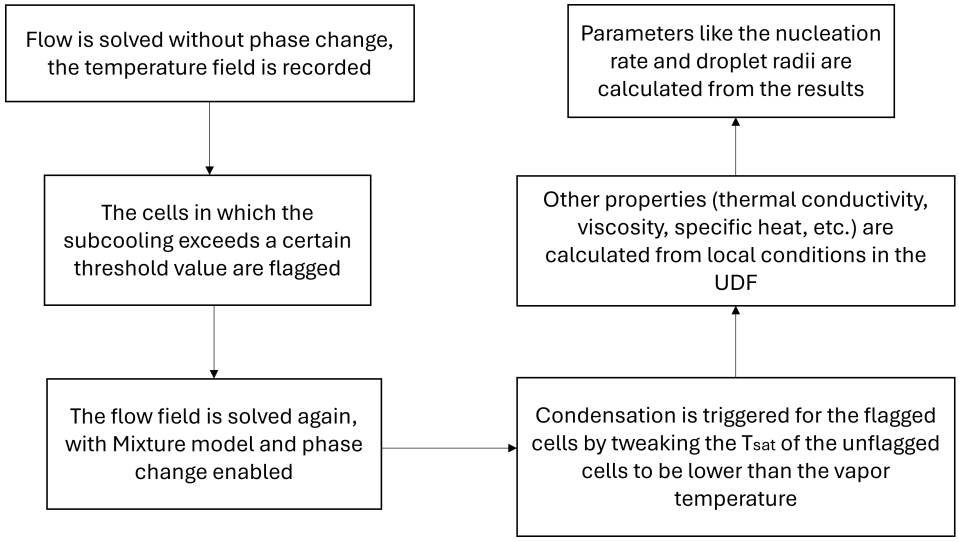

Figure 3.7: The algorithm for the ANSYS Fluent UDF (User-Defined Function) used to trigger condensation based on a critical value of subcooling.

The working of the UDF is illustrated in Figure 3.7. The flow field is initially solved without enabling phase change, only to record the temperature field, and then checked for cells that exceed a certain level of subcooling ($T_{sat} - T_v$). These cells are flagged, and in the next simulation, with the multiphase and phase change models enabled, condensation is triggered in these cells. The ideal gas properties of the air-steam mixture are obtained as polynomial functions of the local temperature, calculated in the UDF. The final field is obtained, which now captures phenomena like the condensation shock caused due the release of latent heat due to liquid generation. The nucleation rate and Sauter droplet radii can be evaluated from this data.

This technique utilized here triggers condensation by tweaking the saturation temperature of the flow. In the flagged cells, the local saturation temperature is fed to the saturation temperature parameter field utilized in the Lee model (Equation 3.34). In all other cells, the saturation temperature is made to be lower than the vapor temperature at that point, so that no condensation occurs. This leads to a one-way coupled model, as temperature is read from a no-phase-change case, and based on that, phase change is simulated, which leads to some loss of accuracy. This is because, once the latent heat is released, the subcooling goes down, hindering further condensation to some extent. Since our approach is based on triggering condensation based on the subcooling values read from a preliminary simulation, it becomes difficult to incorporate this feedback.

3.4.5. Droplet size modeling

An ensemble of droplets in nature contain droplets of various sizes. This size distribution can be visualized in the form of a histogram. It is often convenient to work with an average value, which can be obtained in many ways, such as arithmetic, geometric or harmonic means, and even fractals. One such formulation is the Sauter mean diameter, also known as the surface-volume mean. This does not give any information about the physical topology for the drops, and is just a mathematical way of estimating the diameter from the surface-to-volume ratio. This formulation goes well with the Euler-Euler model, as by definition, there are no particles, only two continuous phases.

It is assumed that the size of the drops vary from some non-zero minimum diameter to some finite maximum diameter. The n^{th} moment of a distribution function $f(D)$

$$M_n = \int_0^\infty D^n f(D)\, dD. \tag{3.38}$$

A single representative number characterizing the drop size is required, which is often the median diameter. This standardizes the size of the drops throughout the domain. A general mean diameter can be defined by,

$$D_{pq} = \left[\frac{\int_0^\infty D^p f(D)\, dD}{\int_0^\infty D^q f(D)\, dD} \right]^{\frac{1}{p-q}}. \tag{3.39}$$

The mean diameter with the same ratio of volume to surface area as the entire ensemble is known as the Sauter mean diameter D_{32}. It corresponds to values of $p = 3$ and $q = 2$ in the above equations. The German scientist Sauter [86] first used this method to study atomization in carburetors and developed a technique to obtain size of drops based on scattering of light, since scattering is proportional to the surface area of the droplets. The different diameters and their common uses are shown in Table 3.4.

Mean diameter	**Name**	**Field of application**
D_{10}	Arithmetic or linear	Evaporation
D_{20}	Surface	Surface area controlling (e.g., absorption)
D_{30}	Volume	Volume controlling (e.g., hydrology)
D_{21}	Surface diameter	Adsorption
D_{31}	Volume diameter	Evaporation, molecular diffusion
D_{32}	Sauter	Efficiency studies, mass transfer, reaction
D_{43}	De Brouke	Combustion equilibrium

Table 3.4: The different mean diameters used to characterize droplet sizes and their applications [87].

Now, the D_{32} term shall be modeled in the context of atomized drops of fluid in vapor, which is similar to a condensing flow.

It is assumed that, at $t = 0$, when a liquid is introduced into a gas flow with constant turbulence properties, the liquid phase pattern will gradually evolve into a monodispersed spray over time. The characteristic time scale for this transition towards the equilibrium monodispersed spray is denoted as τ_c. In this final state, the equilibrium droplet size r_{eq} is determined by the equilibrium between the forces driving droplet break-up, such as the shear effects from fluctuating or mean velocity gradients and droplet collisions, and the coalescence process.

The expression for the equilibrium radius is derived under the assumption that droplet collision is the dominant break-up mechanism and that the kinetic energy of colliding droplets is equal to the minimum increase of the surface tension energy during break-up [88]. Thus, the representative mean radius is given by,

$$r_{32} = r_{eq} = C_r \left(\frac{\bar{\rho}\tilde{Y}_l}{\rho_l} \right)^{2/15} \frac{\sigma^{2/5}}{\tilde{\epsilon}^{\frac{2}{5}} \rho_l^{3/5}}, \tag{3.40}$$

where, $\tilde{Y}_l$ is the liquid mass fraction, σ is the surface tension of the liquid, and C_r is a constant that needs to be tuned.

3.5. Solution Strategy

The types of solvers available in Fluent may be divided into pressure- and density-based. The solver used for the simulations is a pressure-based solver. Generally, the density-based solver is recommended for compressible flows as it has better shock resolution capability, however, it is not compatible with the Mixture model, so the pressure-based one is adopted. The velocity and pressure are solved numerically from Equation 3.25 and Equation 3.28, and this step is referred to as pressure-velocity coupling.

Under the pressure-based option, there are two types of pressure-velocity coupling algorithms available:

- Segregated algorithm - The governing equations are solved one-by-one, requiring less memory (SIMPLE, SIMPLEC, PISO).
- Coupled algorithm - The momentum and continuity equations are solved in a coupled manner, improving the convergence speed.

The pressure-based coupled solver is chosen for the steady-state problem as it is efficient and performs better for more complex cases, such as multiphase problems. The algorithm followed by this solver is shown in Figure 3.8.

The gradient spatial discretization technique used is the Green-Gauss Node Based scheme, as it has minimal false diffusion as compared to the other available methods, and is strongly recommended for unstructured and skewed meshes with tetrahedral elements [89]. PRESTO! is chosen as the pressure interpolation scheme, which is suitable for high-speed rotating flows in domains with strong curvature [66]. It is generally recommended to be used with the Mixture model. Moreover, Warped Face Gradient Correction is enabled which improves the accuracy of gradient calculation on grids with high aspect ratios. For the discretization of all convective terms except the volume fraction, the second-order upwind

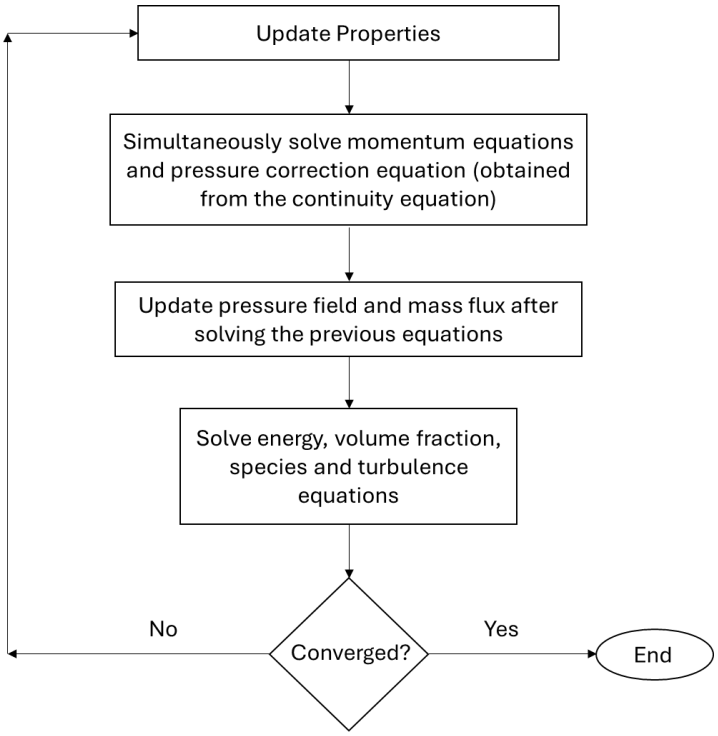

Figure 3.8: The ANSYS Fluent Pressure-based Coupled solver algorithm.

scheme is used, as the use of first-order schemes lead to significant numerical diffusion. Higher Order Term Relaxation (HOTR) is enabled, which is proven to accelerate convergence for steady-state rotating turbomachinery cases using the $k-\omega$ turbulence models [66].

Under the Mixture model, an implicit formulation is chosen for the volume fraction discretization, which is iterative and suitable for steady-state applications. A first-order method is utilized. An under-

relaxation method is enabled, and the solution is stabilized by using smaller under-relaxation factors in the range of 0.2 to 0.5 for different terms. If higher under-relaxation factors are used, the solution diverges, so it is quite sensitive to these values.

The system is initialized using an Hybrid initialization method (where a simplified Euler problem is solved for 10 iterations to get a good initial guess field). The patch function is used to initialize the entire domain with humid air (80%) relative humidity), at volume fraction 1. The convergence criteria is set to 10^{-3} for the energy residuals and 10^{-6} for all other scalar residuals (ANSYS Fluent default settings).

In addition, the average mass flow rate at a plane on the outlet duct is used as a convergence criterion, as it is difficult to get very flat residuals in turbomachinery cases. This plane is chosen far downstream of the rotor, but upstream of the actual outlet, so that the reverse flow at the outlet doesn't affect the flow there. It is shown in Figure 3.9. When the average mass flow residuals at this plane reach 10^{-5}, convergence is attained.

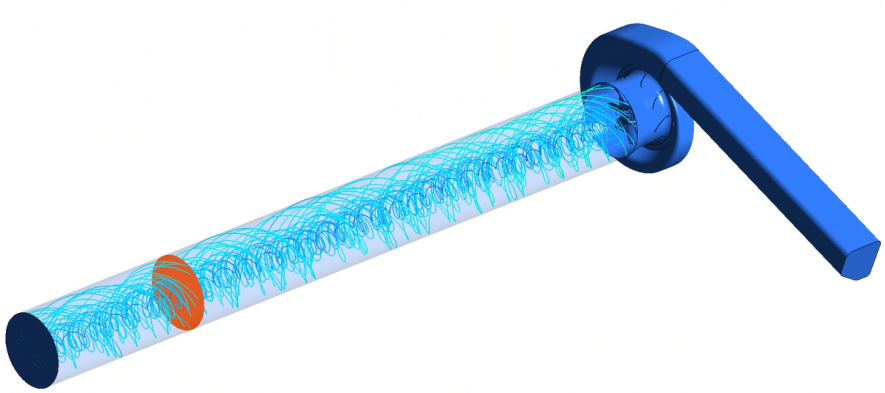

Figure 3.9: The plane (orange) upstream of the outlet where the mass outflow convergence condition is imposed.

4

Results and Discussion

4.1. Model Validation

The multiphase model used, as discussed in Chapter 3, is the Eulerian-Eulerian Mixture model along with custom physics to trigger condensation, defined using a User-Defined Function (UDF). This model is validated for a planar Moore B nozzle geometry against experimental data.

The primary aim of the model is to capture the 'condensation shock', which appears due to the onset of condensation. In Figure 4.1, the static pressure distribution along the centreline is illustrated, for a condensing and a non-condensing flow, under the same conditions. The bump in the pressure represents the pressure recovery due to the release of latent heat as condensation begins. This provides a visualization of the differences to be expected between the flow fields: a dry flow and a condensing flow.

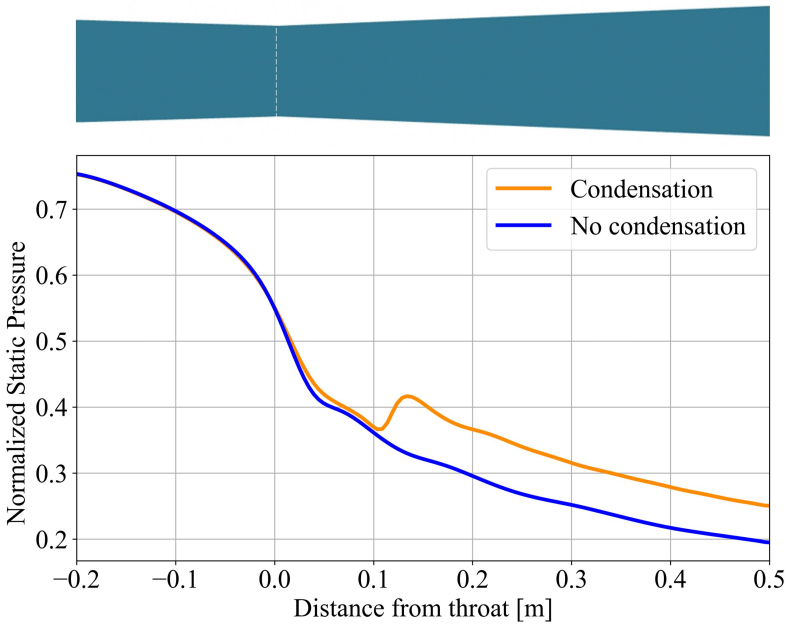

Figure 4.1: The static pressure profile along the centreline of the Moore B nozzle for a condensing and a non-condensing flow.

Apart from experimental validation, our results are also compared with another CFD study from Li et al. [90], which investigates spontaneous condensation in a Moore B nozzle. Thus our validation in done in 2 parts, as presented in the following sections.

4.1.1. Experimental Validation and the Impact of Slip Velocity

The experimental data for condensation in multiple nozzle designs is available from tests conducted by Moore [58]. One of them was the Moore B nozzle, which is popularly used as a benchmark case. Static pressure and droplet size measurements were taken. Two versions of our model are presented against the experimental data.

The slip velocity is simply the relative velocity of the secondary phase (p) with respect to the primary phase (q):

$$\vec{V}_{pq} = \vec{V}_p - \vec{V}_q. \tag{4.1}$$

If enabled, from the slip velocity expression, a drift flux model is obtained [66], which accounts for the acceleration of the particle driven by gravity, centrifugal forces, and turbulence, and includes models for drag formulation.

In one case, the slip velocity equation is included, whereas in the other, it is disabled. The purpose of this distinction is to show how significantly the omission of slip velocity impacts the flow, since, for the final use of the model on the turbine, it is not included: Enabling the slip velocity equation for the turbine rotor flow gives rise to numerical instabilities and leads to solution divergence.

In Figure 4.2a, the centreline normal static pressure (P/P_{0I}) for the two models is plotted against test data, where P is the static pressure and P_{0I} is the inlet total pressure. It is observed that the pressure drops with expansion beyond the throat. As a result of this expansion, the flow cools down. The subcooling (ΔT) of the flow is given by how much the temperature (T_v) drops below the local saturation temperature ($T_{sat}(P) - T_v$). This subcooling reaches a threshold value, and condensation is triggered. As soon as the liquid droplets start to form, latent heat is released, leading to a pressure recovery as it shoots back up before continuing to expand.

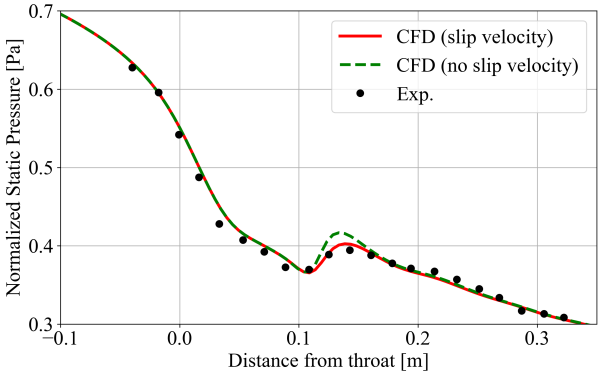

(a)

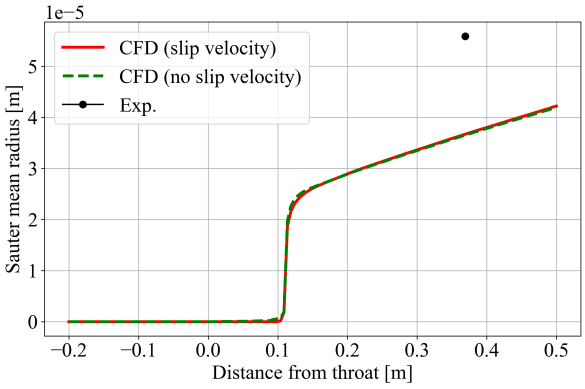

(b)

Figure 4.2: Validation of CFD model (with and without slip velocity) against (a) Static pressure, (b) Droplet radius data from experiments by Moore [58].

It is evident that the model with slip velocity enabled reproduces the experimental data more faithfully, which is expected. The model without slip velocity gives a close estimate; however, in the region of pressure recovery after the onset of condensation, it over-predicts the rise. This might be due to the lack of damping forces resulting from the exclusion of drag and other similar effects. The margin of error is not significant and the location of condensation is predicted accurately; thus, the slip velocity condition can be safely omitted.

From Figure 4.2b, only one data point is available from the experiments, which is significantly higher than the values predicted by the models at that location. The models used give only a representative average diameter at that location, assuming all droplets there are the same size (mono-dispersity). However, in reality, it would be a poly-dispersed scenario with a range of droplet sizes, and it is bound to vary.

4.1.2. Validation against other Numerical Studies

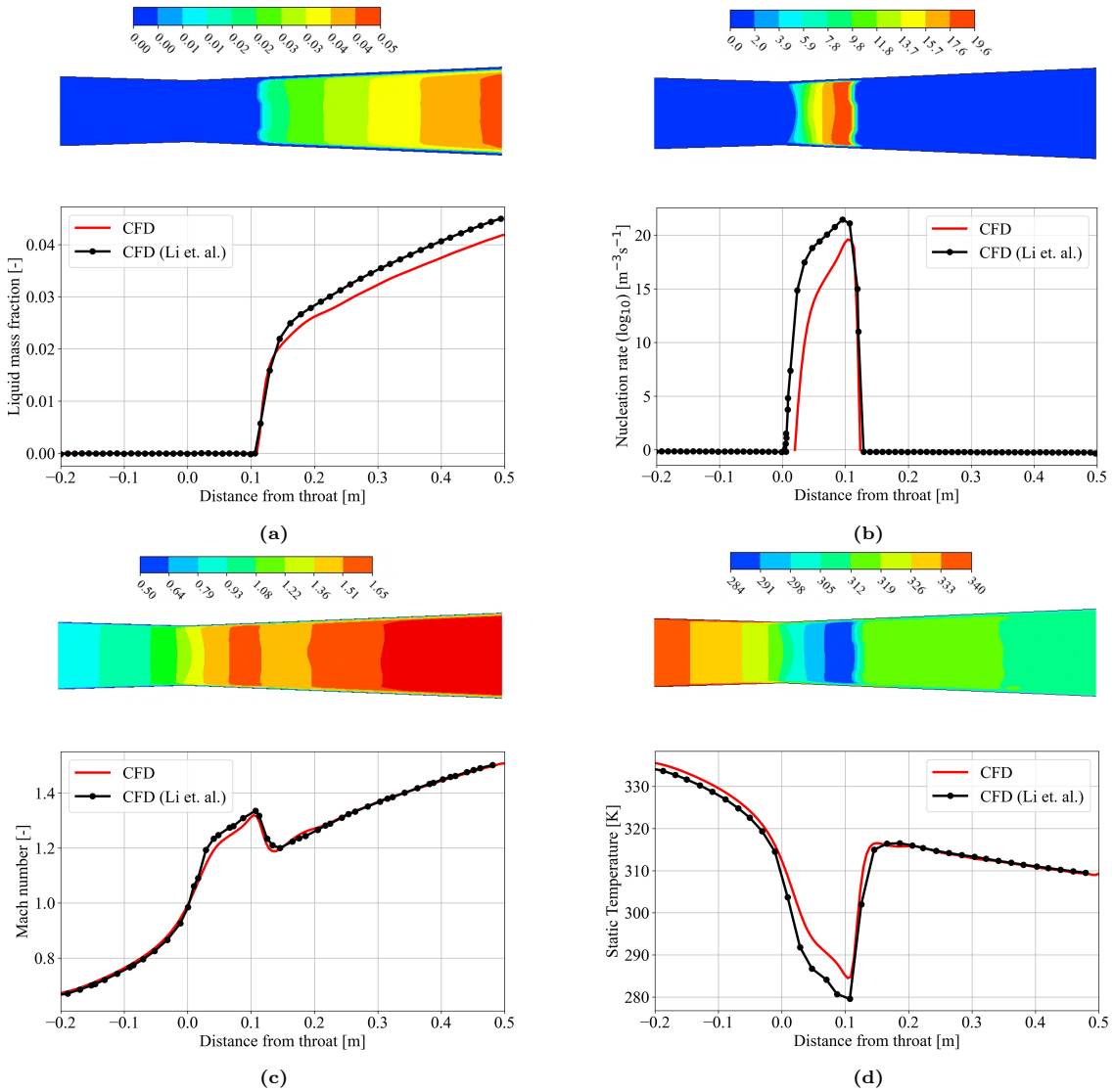

Figure 4.3: Contour surfaces and plots along the nozzle centreline for validation of model (red line) by comparison against data from CFD study by Li et al. [90] (black dots) for parameters: (a) Liquid mass fraction, (b) Nucleation rate, (c) Mach number, and (d) Static temperature.

As an additional validation step, results obtained with the current approach are compared to those of another published CFD study [90]. Their mathematical formulation involves equations for liquid mass transport, nucleation rate, droplet growth and droplet density along with the main conservation and turbulence equations. It is a comprehensive model, with strong coupling among the scalars, and it was employed to study condensation in the Moore B nozzle.

In Figure 4.3a, a comparison of the liquid mass fraction distribution along the centreline is shown. Our model slightly under-predicts the values downstream of the condensation shock zone, by a small margin. Similarly, in Figure 4.3b, the nucleation rate, which is the rate of formation of liquid droplet nuclei per unit volume per unit time, is obtained to be lower compared to the study by Li et al. [90]. The static temperature plot in Figure 4.3d shows that the maximum cooling reached by the system in our case is less than that reached by the reference model, which explains the under-estimation of the condensed liquid fraction and nucleation rate. However, in all these cases, the nature of the plot is reproduced accurately. In Figure 4.3c, the Mach number distributions almost overlap, showing good agreement. Thus, it can be concluded that our model, without slip velocity, guarantees an acceptable degree of accuracy.

4.2. Mesh Independence Study for Turbine Setup

The mesh utilized for this study has been discussed in Section 3.2.1. To ensure the robustness of the mesh, 3 meshes were tested to simulate the same condensing flow problem on the turbine. The mesh sizes corresponded to 6.7 million, 9.6 million, and 12 million cells, as presented in Table 4.1. Some key parameters - the rotor outlet temperature, the mass fraction of liquid at the outlet, and the static pressure drop across the rotor were checked and compared to ensure independence of solution from mesh refinement.

As shown in Table 4.1, the outlet temperature values (T_{out}) do not change much in the finer meshes, and the total pressure drop (ΔP) only changes marginally. The liquid mass fraction values (y_{out}) at the outlet show converging values for Mesh 2 and 3 as well. The circumferentially averaged static pressure profiles along the inlet-to-outlet streamwise direction are shown for all the meshes in Figure 4.4. This line chosen for the analysis is explained ahead, where Figure 4.8a shows the inlet and outlet planes.

The profiles show the static pressure fields approaching convergence as the meshes become finer. From the inlet (streamwise 0 location) up to streamwise 0.2, the pressure profiles for the finer meshes 2 and 3 almost overlap. However, after condensation ensues, some difference is observed in the two profiles, leading to a marginally different pressure drop. However, Mesh 3, consisting of 12 million cells, is considered quite expensive in terms of computational resources, time, and also pre/post processing speed. Thus, Mesh 2 – consisting of 9.6 million cells – is chosen, offering a good balance of accuracy and moderate computational expense.

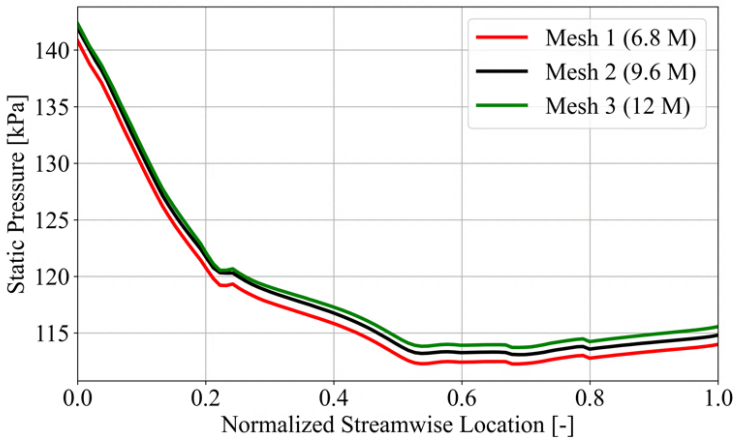

Figure 4.4: The inlet-to-outlet averaged distribution of the static pressure for the three meshes tested.

Parameter	Mesh 1 (coarse)	Mesh 2 (fine)	Mesh 3 (finest)
Cells	6,762,880	9,690,891	12,016,626
Nodes	2,384,215	3,234,932	3,912,129
$T_{out}/T_{out,finest}$	1.00595	1.000049	1
y_{out} (%)	2.228	1.835	1.829
$\Delta P/\Delta P_{finest}$	1.0162	1.0057	1

Table 4.1: Comparison of the three meshes tested.

4.3. Turbine results

In this section, the model that was discussed in Chapter 3 and validated with the Moore B nozzle geometry is implemented for the turbine setup. The results obtained are analyzed and inferences about the physics of the system are drawn. The subcooling threshold is justified, and parametric studies are performed to show the impact of the relative humidity, the inlet pressure and the rotational speed of the rotor on the condensation characteristics.

4.3.1. Choice of Subcooling Threshold

As discussed earlier, the trigger for the condensation to occur is a critical level of subcooling which then cues the solver to generate liquid water in those cells. For the Moore B nozzle, the critical level of subcooling was set at 37 K. It was found from test data that the maximum subcooling reached can be around 30 K and the model was further calibrated to match experimental data. However, a major difference in the turbine case is that our flow consists of an air-steam mixture, and the subcooling levels will be significantly different. This is because the operating conditions are different, and more importantly, the local saturation temperature depends on the partial vapor pressure, given by,

$$P_{total} = P_{H_2O} + P_{air}, \tag{4.2}$$

$$P_{H_2O} = x_{H_2O} \times P_{total}. \tag{4.3}$$

P_{H_2O} is the vapor partial pressure, which depends on the mass fraction x_{H_2O} of the water vapor present in the air. This mass fraction value is governed by the relative humidity value specified at the inlet. For 80% relative humidity (RH), the value of x_{H_2O} is 0.152, so the partial pressure of water vapor will be $\sim 15\%$ of the total pressure. This indicates that the saturation temperature will be much smaller than it would have been if there were only water vapor present. The subcooling is given by,

$$\Delta T = T_{sat}(P, x_{H_2O}) - T(P). \tag{4.4}$$

Now, if the T_{sat} is much lower, the maximum critical subcooling will also have a smaller value than the tested 37 K in the nozzle case. This logical deduction is backed by some results from Mao et al. [91]. The study by Mao et al. [91] was conducted to validate an Euler-Euler Source Term model implemented using CFD, against some experiments conducted using a fuel cell turbine. Their setup is similar to our present case, with the rotor wheel sizes being close and the absence of a stator in either case. The conditions implemented are similar to the ones used in our study, and even though the rotor geometry is different, these values provide a close estimate.

The subcooling data obtained from their model is given in Figure 4.5, based on which our subcooling threshold will be set. The inlet temperatures 348 K, 353 K, and 358 K correspond to 3 different levels of relative humidity, 100%, 80% and 60%, respectively.

The operating point chosen as the base case for analysis comprises of the turbine setup with inlet temperature 353 K, relative humidity 80% and mass flow 0.1269 kg/s which corresponds to a pressure ratio of about 1.55. So the critical subcooling is chosen as 19 K, from the corresponding curve in Figure 4.5.

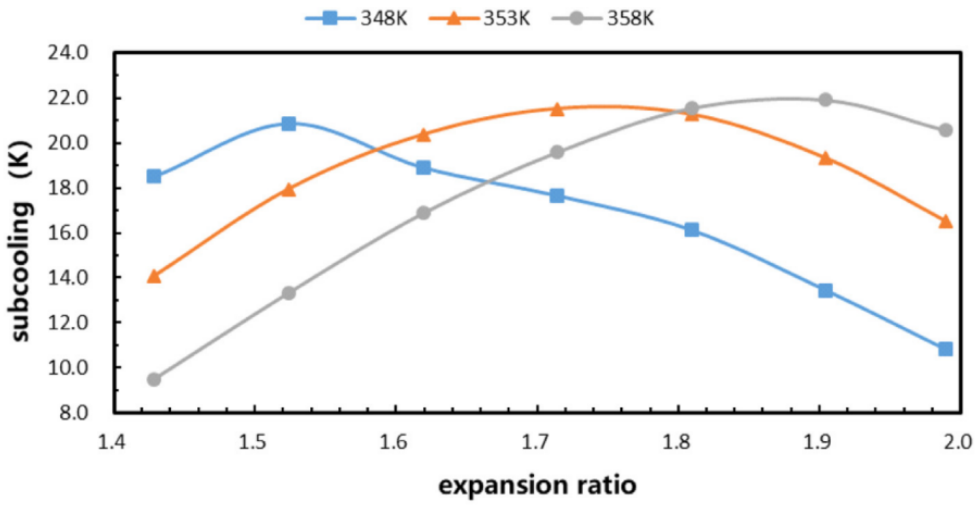

Figure 4.5: The variation of subcooling reached before the onset of condensation with expansion ratio, for different inlet temperatures, from Mao et al. [91].

A preliminary simulation is run as the dry case, where the humid air will not condense and the subcooling is recorded. The isocontours of the regions that have reached the required subcooling are shown in Figure 4.6.

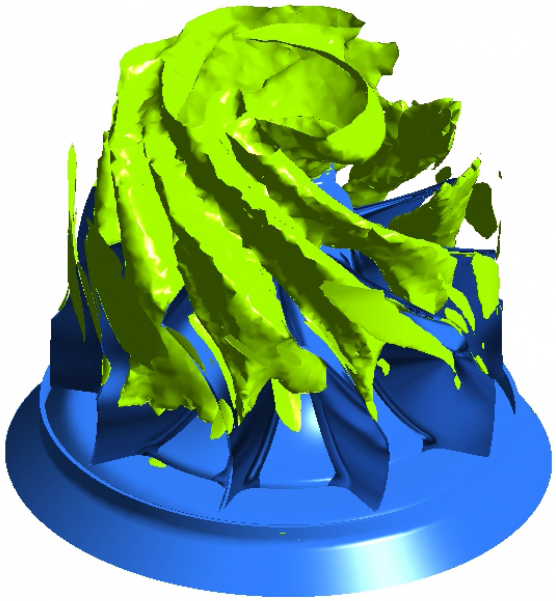

Figure 4.6: Isocontours of subcooling $\Delta T = 19$ K from dry turbine flow (condensation disabled) with humid air.

4.3.2. Surfaces of Analysis

The turbine geometry is revisited, and the flow direction is shown in Figure 4.7. The arrows represent the general flow direction, as it radially enters and axially exits the turbine (flow components in velocity triangles are not shown). In the side view, the leading edge (LE) and the trailing edge (TE) of a blade are shown.

The analysis of the condensing flow is done along various turbo-surfaces and lines,

- Inlet-to-outlet: This represents a line running from the inlet (red) to the outlet (green), which are

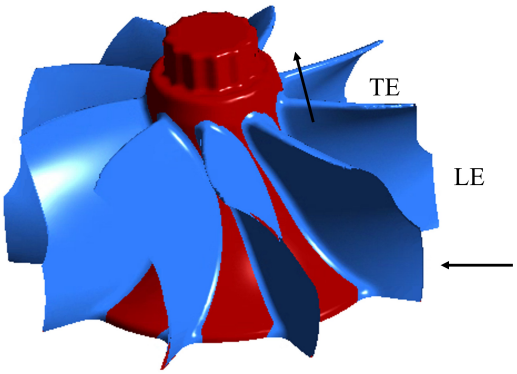

Figure 4.7: The rotor hub and blades; the arrows denote the direction of flow entering and leaving the passages. The leading edge (LE) and trailing edge (TE) are marked.

shown in Figure 4.8a. The inlet is the surface where the scroll opens into the wheel region. The inlet-to-outlet charts use a line along the blade passage in the meridional plane, so it follows the flow between two blades and the circumferentially averaged values of different parameters as the flow proceeds towards the outlet can be observed. The streamwise direction is normalized, so 0 signifies the inlet and 1, the outlet.

- Hub-to-shroud: This is the direction starting from the hub (green) to the shroud wall (red) shown in Figure 4.8b. It signifies the spanwise direction, so 50% span would signify a region right midway between the green and red planes. For spanwise analysis, the circumferential average values are taken starting from normalized span 0 (hub) to 1 (shroud).
- Circumferential: This is the angular direction starting from $\theta = 0°$, as shown in Figure 4.8c, going anti-clockwise. It makes it easy to analyze any circumferential asymmetry in the rotor zone. This can be done at any streamwise location plane starting from the bottom of the blades up to the outlet.
- Meridional: This type of plane sits midway between two blade passages and is similar to a cross-sectional view of the blade passage, going in the radially outward direction. It is the red plane shown in Figure 4.8d. It provides a cross-sectional view of the flow field within the blade passages.
- Blade-to-blade: If a surface extends from the middle of the leading edge to the middle of the trailing edge following the curvature of the blade through the rotor zone, and the surface is laid flat, the plane shown in Figure 4.8e is obtained. In Figure 4.8c, the blades are numbered, and the blade-to-blade section plane goes from B1 to B9 as shown.

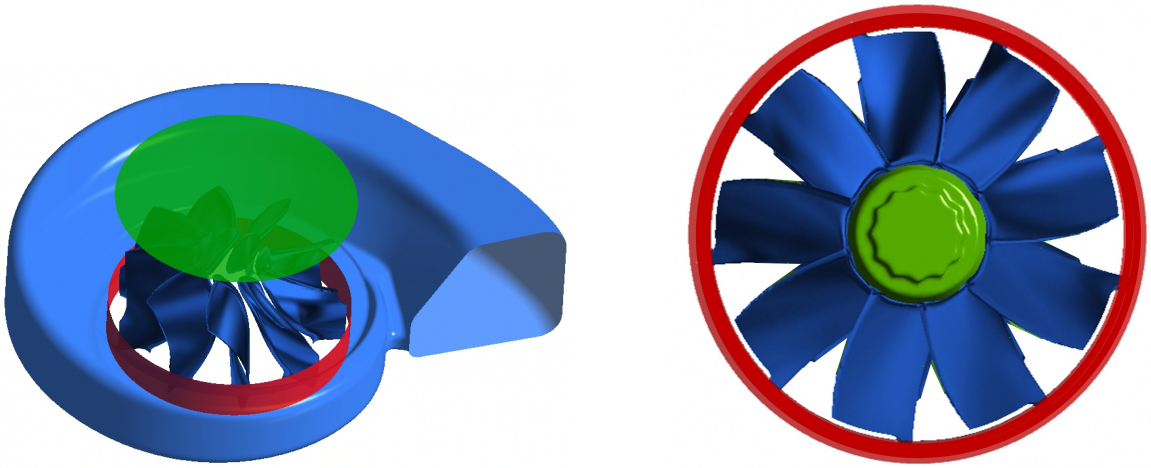

(a) **(b)**

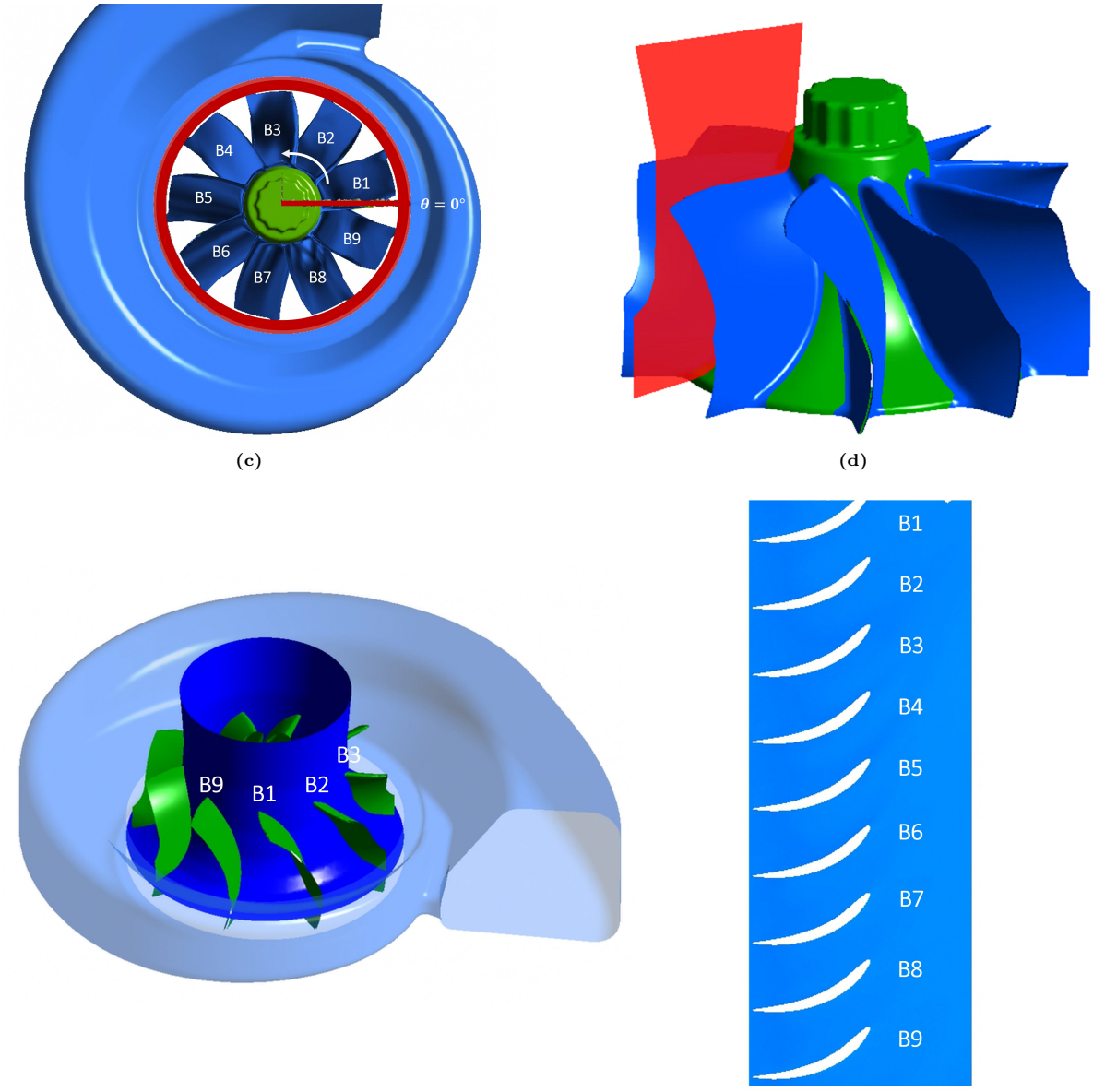

Figure 4.8: Visualizing the surfaces of analysis: a) Inlet-to-outlet, (b) Hub-to-shroud, (c) Circumferential plane, (d) Meridional plane (red) and (e) Blade-to-blade surface at 50% span - the surface within the rotor zone (left) and the surface laid out flat (right).

4.3.3. Inlet-to-outlet analysis

After flagging the cells that exhibit higher than critical subcooling, the condensation model is enabled. The results from this case are analyzed along the inlet-to-outlet turbo-line.

A comparison of the temperature and pressure profiles obtained in the blade passages, from the hypothetical 'dry' case (humid air without condensation model enabled) and the wet case (humid air with condensation enabled) is performed. This is done to isolate the changes in the flow parameters introduced just due to the flow condensing, under the same conditions and composition.

In Figure 4.9a, the static pressure variation from the inlet to the outlet is shown for both cases. The difference is small and the trend for both the graphs is similar. This could be explained by the loss of gaseous mass flow due to condensation, which raises the static pressure to maintain the mass flow rate, since a mass flow inlet boundary condition was imposed. The condensation shock, which was visible in

the Moore B nozzle is not seen here, probably due to the circumferential averaging, as well as the weak intensity of the condensation, as explained by Mao et al. [68].

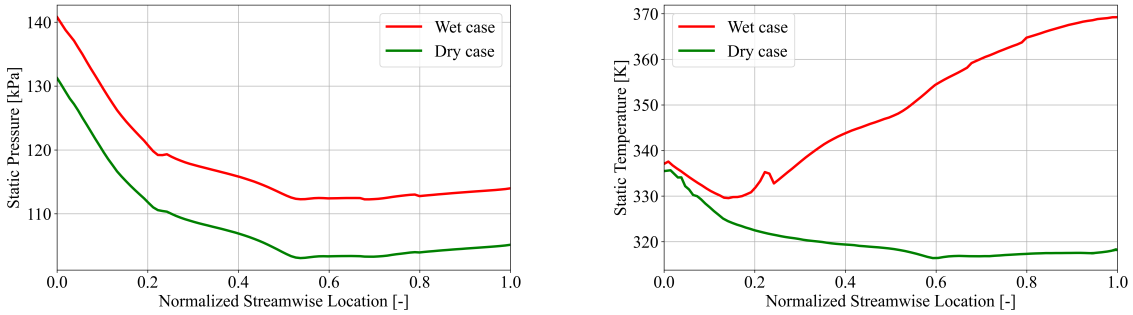

Figure 4.9: The inlet-to-outlet distribution comparing the (a) Static pressure, and (b) Static temperature for dry (hypothetical) and wet cases, i.e., humid air with and without condensation enabled, respectively.

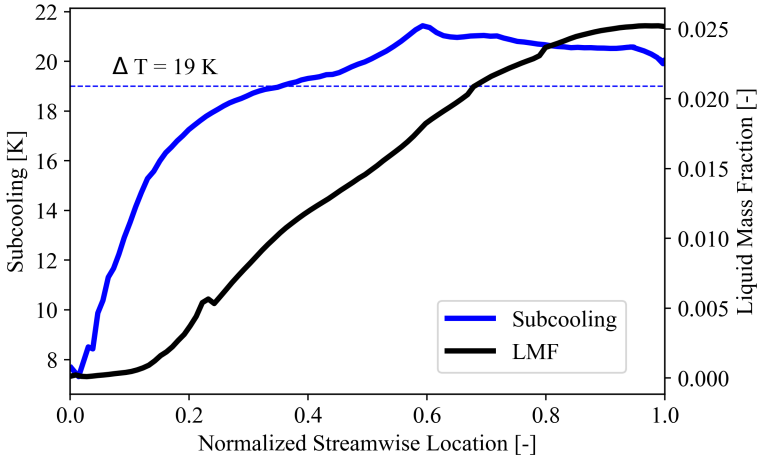

Figure 4.10: The variation of the averaged values of subcooling (green) and liquid mass fraction (red) along the streamwise inlet-to-outlet direction.

The static temperature variation in this direction shows the effects of condensation significantly, as shown in Figure 4.9b. In the dry case, the temperature drops with expansion in the passage, as expected. However, for the wet case, after an initial drop, the temperature keeps rising, marking the onset of condensation. A small spike is seen right after the 0.2 streamwise mark, which might be due to the rapid pressure drop at that location, leading to the onset of condensation. The latent heat release significantly raises the temperature, and a much hotter flow exits the rotor zone. The liquid generation raises the outlet temperature above the rotor inlet temperature.

In Figure 4.10, the subcooling, based on which condensation is triggered, and the liquid mass fraction in the flow are shown along the inlet-to-outlet path. It can be observed that the subcooling reaches 19 K (dotted line), and the liquid mass fraction grows rapidly in that region. However, since these values are circumferentially averaged, it is found that some liquid starts to form before the average reaches 19 K subcooling, as different regions reach the threshold at different points locally. Mostly, the liquid formation is consistent with our provided trigger, and once the nuclei have formed, they continue to grow, and the liquid mass fraction keeps increasing.

The growth of the droplets is represented by the distributions shown in Figure 4.11. The supersaturation ratio is the ratio of the partial pressure of the water vapor to the saturation pressure at that vapor temperature, given by,

$$S = \frac{P_{H_2O}}{P_{sat}(T)} \tag{4.5}$$

The nucleation rate can be described by the expression given in Equation A.10, which is of the form,

$$J = A \exp\left(-\frac{B}{\log_e(S^2)}\right), \tag{4.6}$$

where A and B are certain coefficients, as seen in Equation A.10. It can be seen that with an increase in S, the exponent becomes less negative and this J increases dramatically. Since the nucleation rate expression is not included in the solution process, and only calculated after the fields have been obtained as an indicator of droplet formation, the simpler parameter of supersaturation ratio S can be used instead for analysis.

In Figure 4.11a, it is found that the S increases at first, and then goes down as the flow condenses. The average radius of the droplets formed, as shown in Figure 4.11b, shows a somewhat inverse relationship with the supersaturation ratio. This result is consistent with the results obtained by Mao et al. [91]. Due to a higher nucleation rate resulting from higher S, the formation of very minuscule newly nucleated droplets starts, and as S starts to drop, the already formed droplet sizes keep growing without many additional newly formed droplets, thus increasing the mean radius.

The supersaturation ratio decreases rapidly once liquid formation begins, as the latent heat release raises the temperature. The Sauter mean radius r_{32} distribution is studied in this section, but is skipped for further comparative analysis in the parametric studies section, since its validation in the Moore B nozzle case showed the predicted radius to be in the same order of magnitude as the measured radius, but the values were quite different.

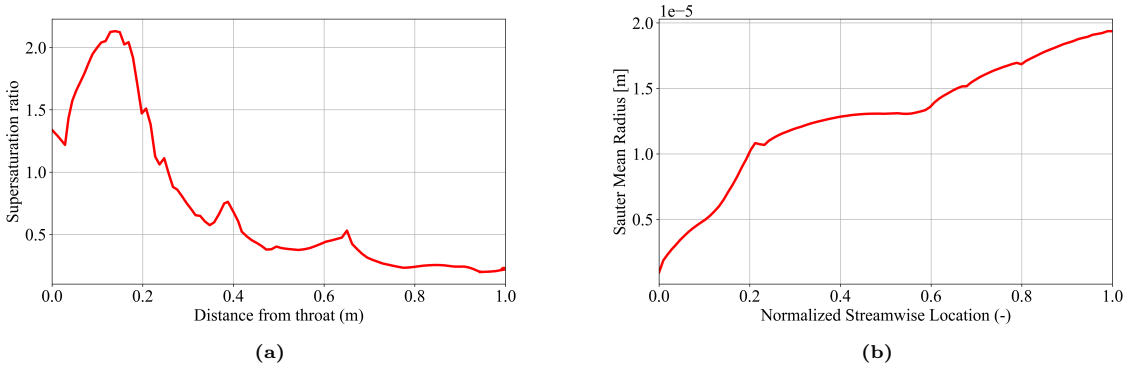

Figure 4.11: The distribution of the averaged (a) Supersaturation ratio and (b) Sauter mean radius along the inlet-to-outlet direction.

4.3.4. Hub-to-shroud analysis

A similar analysis is performed for the hub-to-shroud direction, from which it can be visualized how some parameters vary along the span of the blade, starting from the hub (0) to the shroud (1). This analysis is done at 0.5 normalized streamwise location, which is halfway between the inlet and the outlet. It is seen that most of the liquid generated is in the bulk of the flow, and the averaged value of the liquid mass fraction (LMF) is highest near 40% span. In Figure 4.12a, the pressure is seen to drop progressively from the shroud to the hub, showing that the flow is the most expanded close to the hub.

This explains the trend in the other fields as shown in Figure 4.12. Most of the liquid generated appears at about 40% span. The centrifugal forces try to push the liquid outwards. This is opposed by the tendency of the liquid to accumulate near the low pressure region near the hub, since there is no slip velocity and the liquid travels along with the gas phase. This could be the reason the liquid mass fraction values tend to peak about midway between the hub and the shroud. The latent heat released

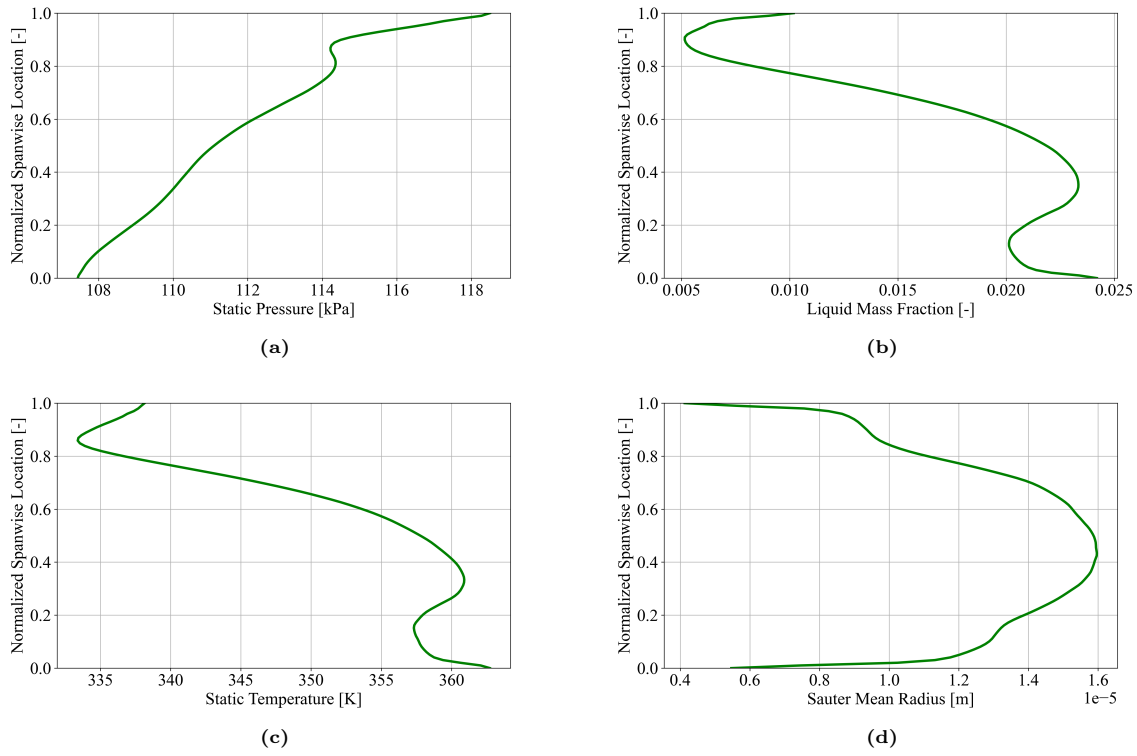

Figure 4.12: The hub-to-shroud distribution for the (a) Static pressure, (b) Liquid mass fraction, (c) Static temperature and (s) Sauter mean radius.

from liquid generation raises the static temperature, and the spanwise peak temperature also occurs at about 40% span. The same is observed for the average Sauter mean radius.

4.3.5. Meridional analysis

The meridional plots showing the Mach number and the liquid mass fraction distribution along the blade passage are presented in Figure 4.13 and Figure 4.14, respectively. A comparison between the results obtained by Mao et al. [68], who performed a study of wetness in an FC turbine, and our current case is presented. The relative humidity is the same for the cases, but the turbine geometries are different and hence the conditions of comparison are not ideal. This comparison is to merely provide a qualitative indication that the results are physical, as the Mach contours and the location for the onset of condensation are at similar streamwise positions.

The Mach number contours show the flow speeding up near the inlet on entering the blade passage, due to rapid expansion. There is good agreement between the two cases. As the liquid condenses, the temperature increases and the pressure recovers, the Mach number goes down. The Mach number in both cases increases in the direction of the blade height, and lower values are seen towards the hub. There is an increase in the gas velocity towards the shroud due to the effect of rotation [68].

The contours of the liquid mass fraction are shown in Figure 4.14. The humid air condenses progressively throughout the blade passage, and most of the liquid is seen downstream of the rotor. The liquid mass fraction predicted in this study is larger for similar inlet conditions. This overestimation could be attributed to the one-way coupling of the subcooling and the liquid generation in our model. In our case, the droplets accumulate towards the hub, which is different from the Mao et al. [68] study, where the droplets move away from the hub. This could be a reflection of the different blade designs causing secondary flows and the fluid accumulating in the low pressure zones near the hub.

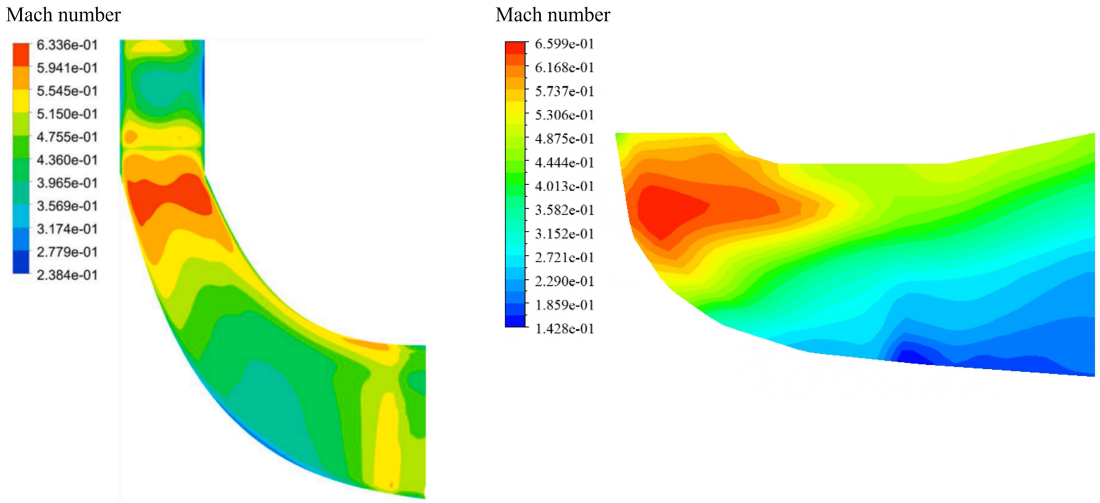

Figure 4.13: Meridional plots comparing the Mach number contours from the study by Mao et al. [68] (left) and present case (right).

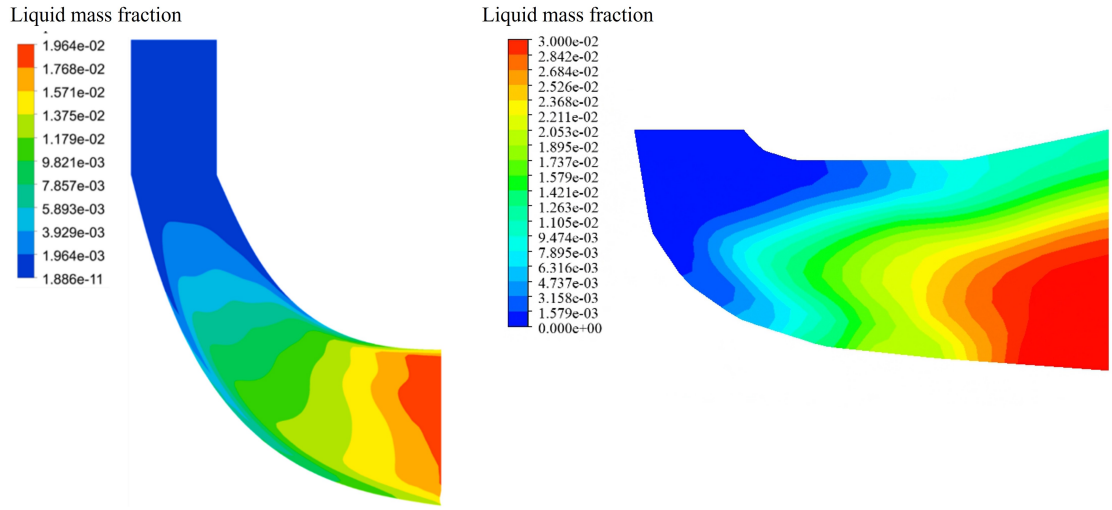

Figure 4.14: Meridional plots comparing the liquid mass fraction contours from the study by Mao et al. [68] (left) and present case (right).

4.3.6. Circumferential asymmetry

Due to scroll asymmetry about the rotation axis, the flow fields in different blade sectors are not identical. This gives rise to a variation in the saturation conditions, and consequently, in the extent of liquid generation. The blade passages farthest away from the start of the scroll show the highest level of subcooling, as the flow velocities are the highest there, as illustrated in Figure 4.15a. This feature of the flow has also been discussed by Wittmann et al. [15]. Some of the effects can be attributed to the technique used to model the rotation, the Frozen-Rotor approach. It is a steady-state approximation and cannot capture transient effects. The rotor is fixed in one position, and a certain blade passage only experiences the inlet conditions in that corresponding sector of the scroll. The effects of different rotor positions with respect to the scroll (clocking) have not been studied.

In Figure 4.15b, the effect of the higher degree of subcooling in some blade passages is reflected as a greater liquid mass fraction. In these passages, most of the liquid is concentrated near the hub and towards the suction side of the blades, most likely due to a combined effect of flow in the streamwise direction and rotational forces, as the secondary forces experienced by radial turbine flows are large [17]. The accumulation of the liquid in the suction side has also been reported in Wittmann et al. [17]. The

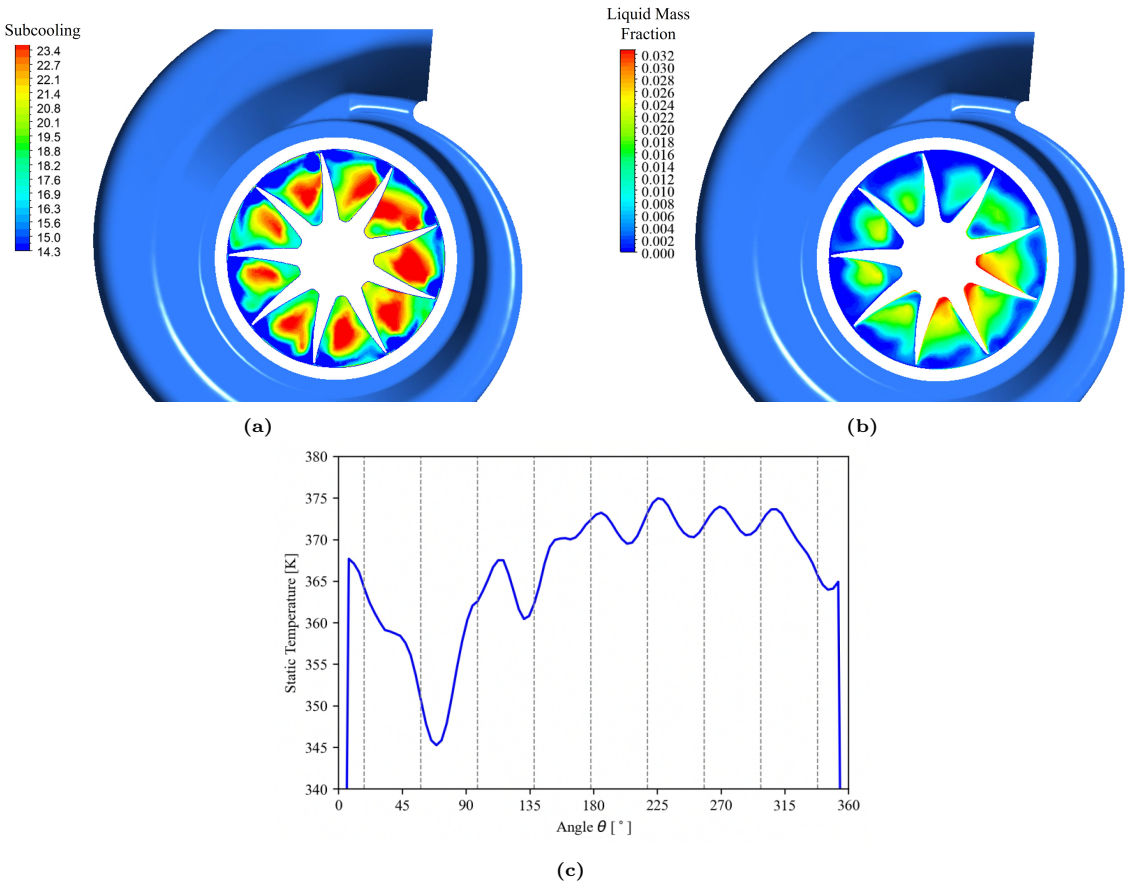

Figure 4.15: The circumferential contours for (a) subcooling, and (b) the liquid mass fraction at 0.5 streamwise location; (c) the circumferential plot for the static temperature downstream of the rotor at streamwise 0.7 location.

formation of liquid films on the blades due to droplet deposition has been investigated in some studies [92], however, the modeling of those effects is beyond the scope of our formulation.

4.4. Effect of Relative Humidity

The relative humidity of gas at the stack outlet is a crucial parameter that decides the location as well as the extent of condensation. In a test setup, the relative humidity can be controlled by changing the stack outlet or the turbine inlet temperature. However, since the aim here is to isolate the effects of the relative humidity, the inlet mass flow and temperature are maintained, and only the RH is varied by specifying the steam mass fraction in the air-steam mixture at the inlet. The values utilized for this study are 50%, 60%, 70%, 80%, and 100%. Only the 60%, 80%, and 100% relative humidity cases will be used for visual analysis, and the other cases will be included in order to show trends.

In Figure 4.16a, from the inlet-to-outlet distribution for subcooling, it is observed that the maximum subcooling reached rises with the increase in the relative humidity at the inlet. If there is a greater fraction of water vapor present from the start, the likelihood of condensation increases. The dotted lines represent the threshold values of subcooling required for the flow to condense, as evaluated from Figure 4.5. For the least relative humidity, 60%, the average subcooling does not go beyond the threshold value till almost midway to the outlet. There are still some regions that cross the threshold locally and thus, condensation ensues there. For 80% RH, at around halfway between the inlet and the outlet, the average subcooling reaches the condition for the onset of condensation. Further raising the humidity, at 100% RH, the threshold is crossed much earlier at about 0.2 streamwise location, causing a much higher fraction of the steam to condense.

Figure 4.16b shows the inlet superheating, which is the difference between the inlet temperature and

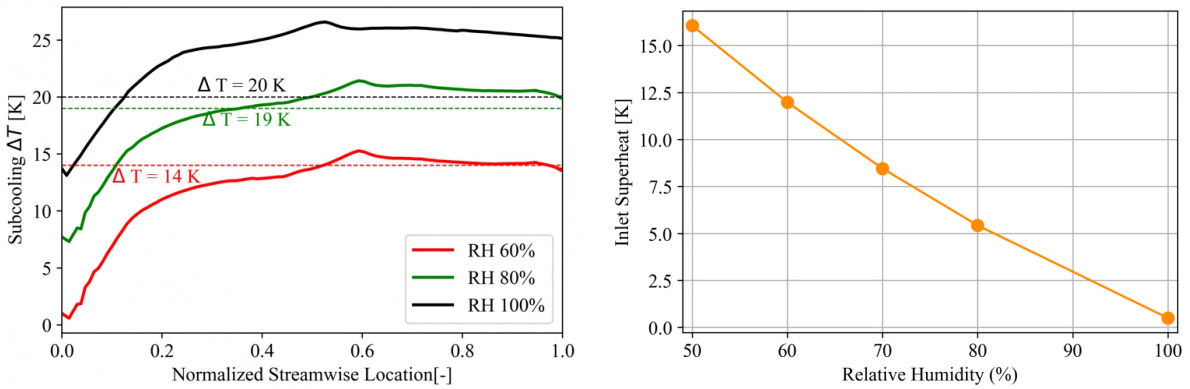

(a) (b)

Figure 4.16: (a) The inlet-to-outlet distribution of the average subcooling for 60%, 80% and 100% relative humidity at the inlet; the red, green and black dotted lines show the threshold values of subcooling used for the 60%, 80% and 100% RH cases, respectively, (b) The variation in the inlet superheating with relative humidity at inlet.

the dew point temperature at the inlet, varying with the relative humidity values at the inlet. The dew point temperature is the temperature at which the vapor pressure is equal to the saturation pressure, so the lower the difference is at the inlet, the easier it is for the flow to condense. This is the key reason for greater levels of subcooling, and consequently, condensation in the blade passages. The superheating values at the inlet decrease almost linearly with an increase in RH. At 100% relative humidity, by definition, the inlet superheat is 0, as it is the maximum amount of vapor that the air can hold under those conditions. The subcooling on the meridional plane is shown in Figure 4.17 for relative humidities

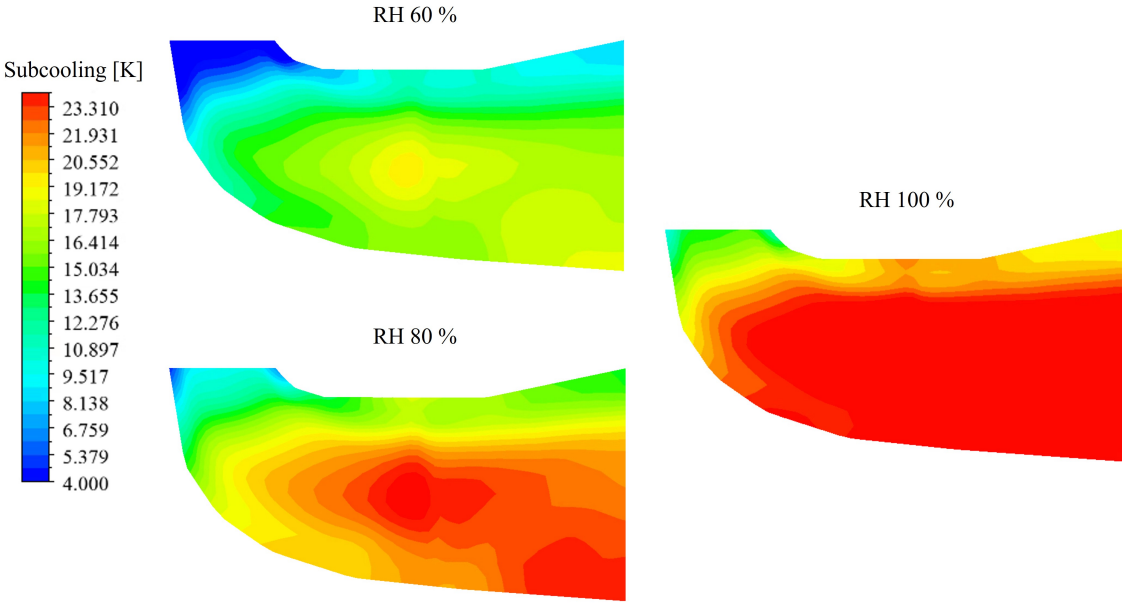

Figure 4.17: The meridional visualization of subcooling in the blade passage that leads to condensation, for 60%, 80%, and 100% relative humidity at the inlet.

60%, 80%, and 100%. The subcooling progressively increases with the relative humidity, and the areas with the greatest temperature dip are midway through the passage, almost at the centre, and near the rotor outlet close to the hub. It can be inferred that these are the regions affected the most by the expansion in this type of rotor. The nucleation rate contours in the blade passage can be seen in Figure 4.18. The highest values of nucleation are observed close to the hub midway through the blade passage. Some more peaks appear close to the same location along the vertical mid-line. These locations are similar to the regions of greatest subcooling.

Overall, the nucleation rate peaks are observed to be greater and more spread out for higher relative humidities. The nucleation rate is not a field variable that is solved for during the iterative solution process; it is calculated from the steady state solution and mainly depends on the vapor temperature and the supersaturation ratio. Thus, there are some discrepancies observed in the subcooling and peak nucleation rate locations, such as in the RH 100% case, where, at the top right corner (shroud side), another peak is observed, but the subcooling there is actually lower.

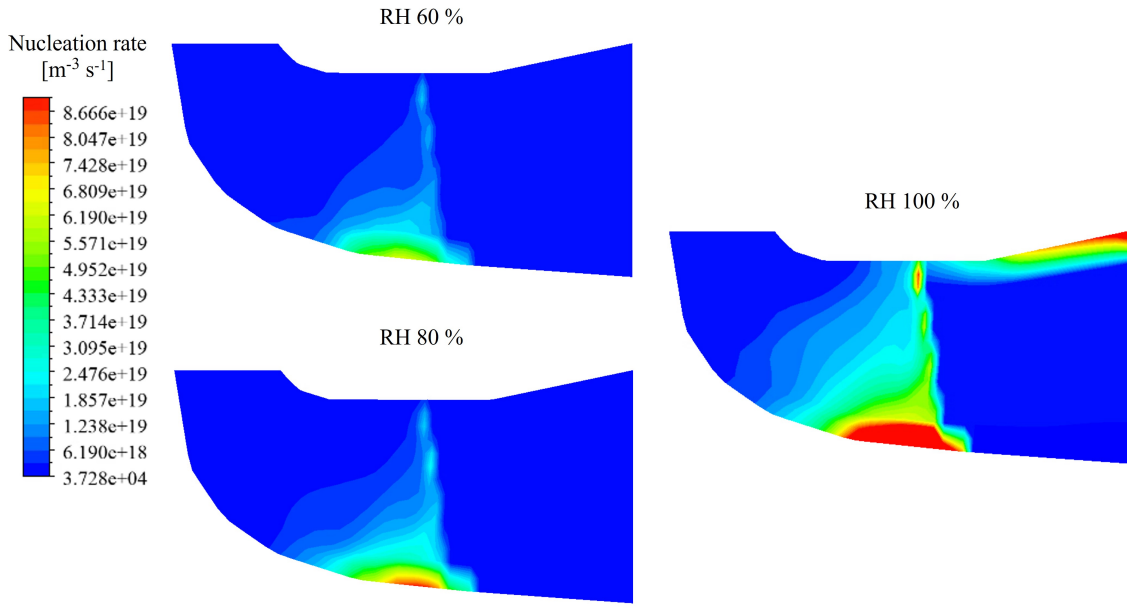

Figure 4.18: The meridional visualization of the nucleation rate of liquid droplets in the blade passages, for 60%, 80%, and 100% relative humidity at the inlet.

Figure 4.19 shows the circumferential variation of the mass fraction of the liquid generated at 50% span, and 0.7 streamwise location, which is a location downstream of the blade trailing edges. The dip in LMF values is only seen in blades near the scroll inlet, where relatively smaller amounts of liquid are generated due to lower subcooling, as established in Figure 4.15a. In the blade passages that are further away, the LMF values rise as the flow expands the highest there. It is already established, and can again be seen here, that the higher the relative humidity, the larger the liquid mass fraction near the outlet. The increase in the liquid fraction at the outlet does not seem to be linear. The increase in the LMF as relative humidity is increased from 60% to 80% is less than the rise observed as the RH goes from 80% to 100%. It can be inferred that the LMF starts to rise by a greater extent as the humidity progresses towards fully saturated conditions.

The blade-to-blade plots of the static temperature and the liquid mass fraction at 50% span are presented in Figure 4.20. In Figure 4.20a, the initial dip in temperature due to expansion can be observed at the start of the blade passages. A blade-to-blade plot of a (hypothetical) dry case without condensation is provided. The expected behavior in an expander is observed, and the temperature drops steadily from the inlet to the outlet. On the other hand, in the wet cases, the low temperature zone near the inlet gets progressively smaller as the humidity increases. It can be inferred that the relative humidity level impacts the degree of liquid generation, as well as the location of the onset of condensation. The latent heat released due to higher liquid generation in the higher RH cases causes the temperature to immediately recover from the dip caused by the expansion in the rotor.

In all of the cases, the temperature at the outlet is higher. In blade passages away from the scroll inlet, the temperature rise is significantly higher, as discussed in the section on circumferential asymmetry. The temperature keeps rising up to the outlet, which could be explained as a deficiency of the one-way coupling used in the model, as it bases the vapor to liquid mass transfer purely on the subcooling levels recorded, but doesn't account for the subsequent loss in subcooling due to the heat release. Higher temperatures are recorded at the suction side, as that is where the flow expands the most.

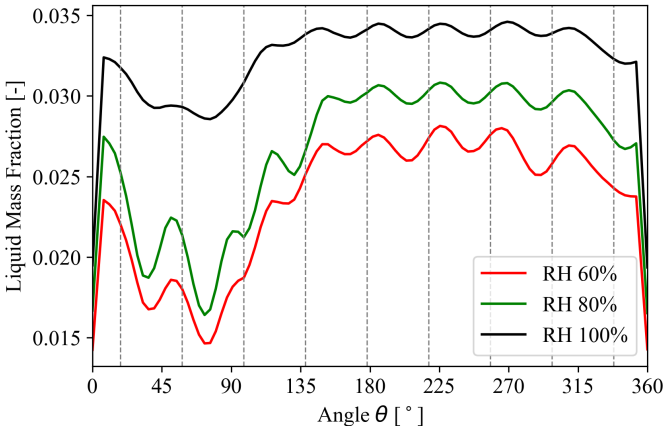

Figure 4.19: The circumferential distribution of the liquid mass fraction for 60%, 80%, and 100% relative humidity; the dotted gray vertical lines correspond to the blade positions.

The liquid mass fraction also follows a similar pattern, as shown in Figure 4.20b. The bulk of the liquid generation takes place towards the end of the blade passage, in agreement with the observations of Wittmann et al. [67]. For 60% relative humidity, there is barely any liquid generation in the blade passage, and only close to the trailing edge, the LMF increases. In the cases with higher relative humidity, the liquid generation starts much earlier, and the mass fraction of the generated liquid reaches higher values at the end of the passage.

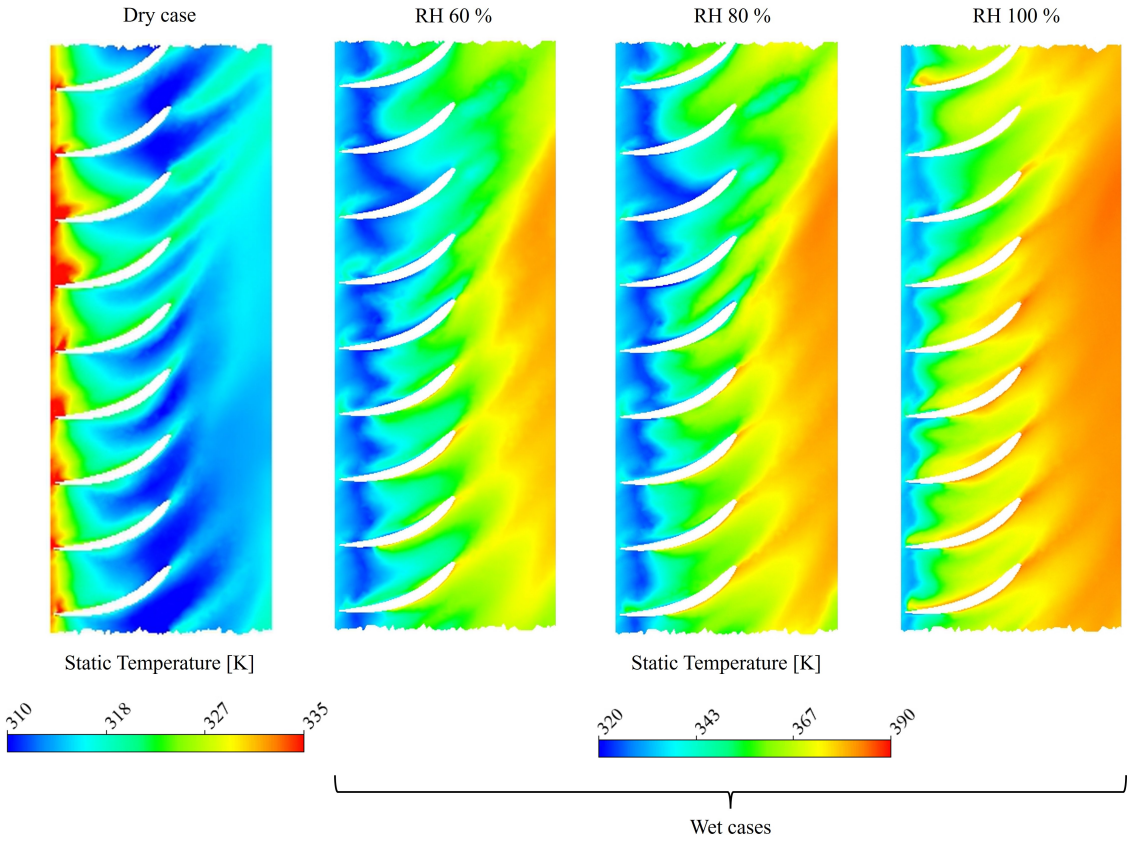

(a) Blade-to-blade plots of the static temperature for a dry case without condensation, and wet cases with condensation.

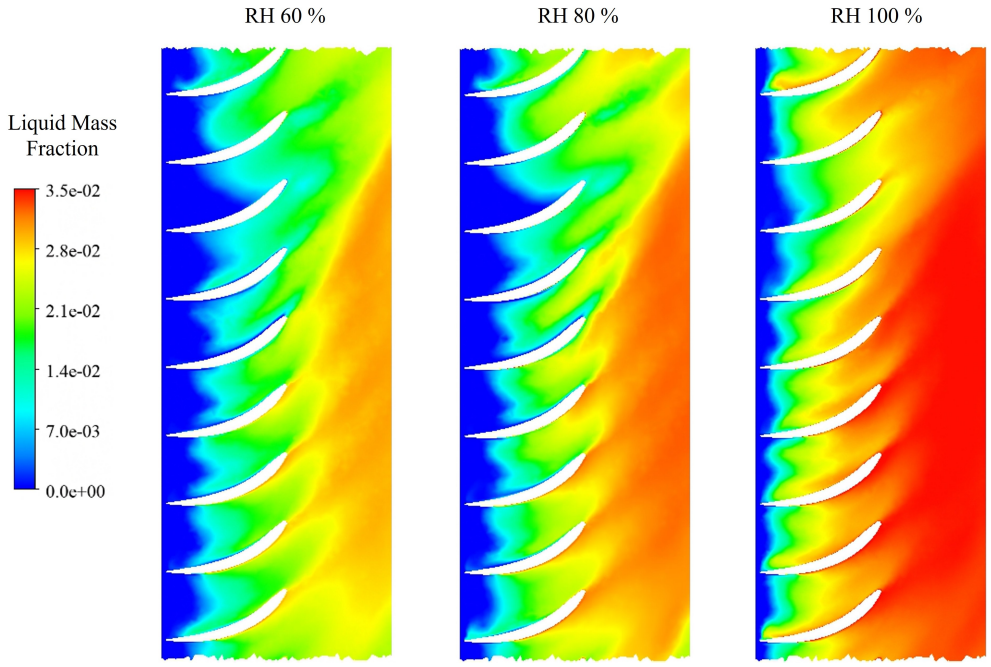

(b) Blade-to-blade plots of the liquid mass fraction.

Figure 4.20: The blade-to-blade plots for cases with relative humidity 60%, 80% and 100%. at 50% span.

The condensed fraction of water vapor and the mass flow reduction in the gas phase are expressed for the different relative humidity levels in Figure 4.21. These values, calculated at the rotor outlet, are given by,

$$\text{Condensed vapor} = \frac{\dot{m}_{liquid}}{\dot{m}_{vapor}} \times 100 \ [\%] \tag{4.7}$$

$$\text{Mass flow change} = \frac{\dot{m}_{liquid}}{\dot{m}_{mixture}} \times 100 \ [\%] \tag{4.8}$$

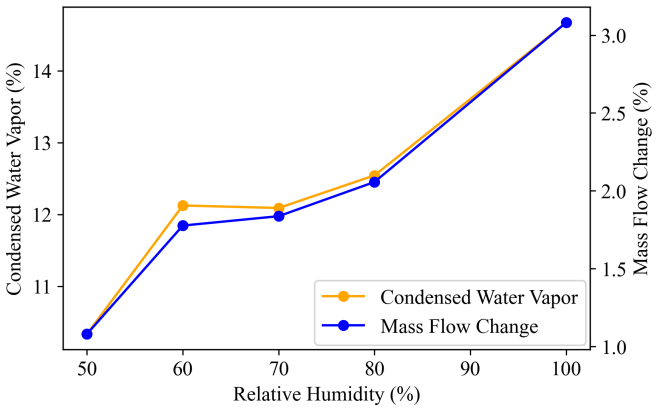

Figure 4.21: The change in the condensed water vapor fraction and the mass flow of the gas phase with relative humidity.

The fraction of condensed vapor goes up as the flow becomes more humid, up to 15%, and so does the change in mass flow. This change in the overall mass flow in the gas phase reflects a direct thermodynamic loss - this is the lost mass flow that could have been used to do useful work and impart energy to the turbine, whereas, on conversion to liquid, it has some detrimental effects. These effects include physical damage such as corrosion, as well as moving the outlet conditions thermodynamically

towards equilibrium, preventing further work extraction from the flow. However, the power output can be observed to increase with an increase in the relative humidity, which will be discussed later in section 4.7.

4.5. Effect of Inlet Pressure

As discussed in the methodology, the inlet pressure is enforced through a mass flow rate. In the preliminary (dry turbine) simulation, where condensation does not occur and only the subcooling is recorded, a pressure inlet boundary condition is provided. The mass flow rate corresponding to this pressure ratio is fed into the next case (wet turbine), with condensation enabled. Ideally, this should result in the same pressure ratio across the turbine. However, due to condensation and the release of latent heat, it leads to a phenomenon called thermal throttling [15].

Due to thermal throttling, for a fixed mass flow rate, the pressure ratio of a turbine increases to keep the mass flow constant, which is exactly what is observed in the present study. The inlet pressures specified in the initial (dry turbine) simulation correspond to pressure ratios of 1.55, 1.65, and 1.75 across the turbine, and these are the numbers mentioned throughout for analysis. However, it is essential to address that the corresponding actual pressure ratios (in wet turbine cases) are larger: 1.64, 1.76, and 1.83, respectively, as a consequence of thermal throttling.

Taking just the rotor region into consideration, it is observed that the effective expansion across the blades is governed by two mechanisms that affect the pressure. One of them is already discussed: the rise in pressure at the inlet to maintain mass flow and compensate for the loss in flow rate due to condensation. This raises the pressure at the rotor inlet. The other mechanism is the release of latent heat, which brings the flow conditions towards equilibrium at the rotor outlet, raising the pressure there.

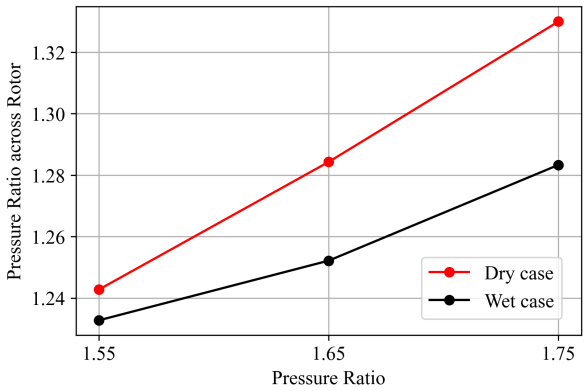

Figure 4.22: A comparison of the effective pressure ratio across the rotor for the dry and wet cases under the same conditions.

So, effectively, the pressure at both the inlet and the outlet of the rotor rises due to the flow condensing. Thus, not a lot can be intuitively said about the rise or drop in the expansion, and it depends on what extent the mechanisms change the pressure. On plotting the pressure drop in the dry case (under the same conditions, without condensation) and the wet case, as shown in Figure 4.22, it is observed that the expansion across the rotor blades is smaller by a margin for all the analyzed cases. Thus, in this case, with a steady mass flow rate, condensation clearly poses an impediment to the expansion in the turbine wheel.

Other fields, such as the liquid mass fraction, vary in the manner presented in the inlet-to-outlet plot shown in Figure 4.23. The liquid generated in the lower pressure ratio cases is only marginally different. For the 1.75 pressure ratio case, a larger liquid mass fraction is observed. The general trend suggests that the higher the expansion, the more the liquid generated, which is in accordance with condensation physics.

The circumferential plot for the temperature at a plane downstream of the rotor blades (streamwise

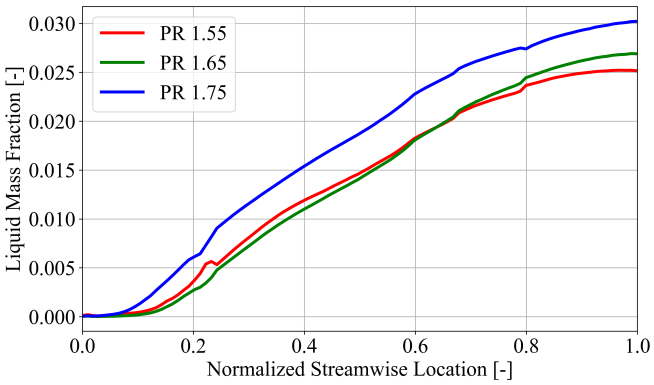

Figure 4.23: The liquid mass fraction distribution on the inlet-to-outlet line for the turbine pressure ratios 1.55, 1.65, and 1.75.

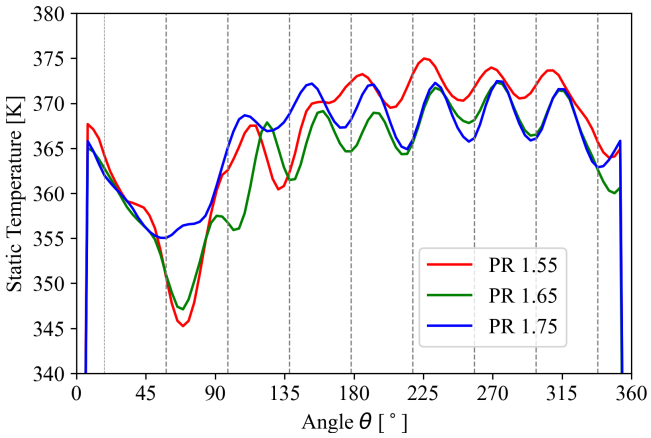

Figure 4.24: A circumferential plot of the static temperature just upstream of the rotor outlet (streamwise 0.7) for the turbine pressure ratios 1.55, 1.65 and 1.75; the dotted vertical lines represent blade positions.

0.7), is presented in Figure 4.24. It is interesting to note that the rotor outlet temperatures increase as the pressure ratio of the system is decreased. This was also noted by Mao et al. [68], who found that the cooling at the rotor outlet plane was greater in the case of higher pressure ratios. The case with the lowest pressure ratio 1.55, has the least liquid generated. However, it has the highest temperatures at the outlet, in spite of releasing a lower amount of latent heat as compared to the rest.

It can be explained by the two competing phenomena of cooling due to expansion in the wheel and heat release near the outlet due to liquid formation. In the 1.55 pressure ratio case, the expansion is not high enough, and the latent heat release takes over, raising the flow temperature as shown. The other cases show a marginal difference in the outlet temperature, as the two opposing mechanisms result in a very similar temperature field for these cases.

The variation in the amount of vapor in the flow that condenses, expressed as a percentage, with an increase in the pressure ratio is shown in Figure 4.25. This increases almost linearly with the pressure ratio, going up to 19% of the steam condensing into liquid water in the rotor passage, as a pressure ratio of 1.75 is imposed. The mass flow change in the gas phase due to liquid condensing out is also shown in the same figure. The lower pressure ratio cases exhibit up to 2% of the mass flow changing, whereas a pressure ratio of 1.75 is found to decrease the mass flow by a higher percentage. This is also evident from the liquid mass fraction distribution presented earlier in Figure 4.23, where this case shows greater liquid generation by some margin.

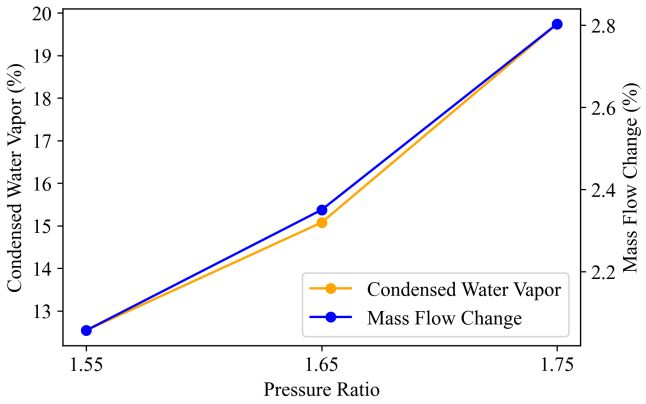

Figure 4.25: The change in the condensed water vapor fraction and the mass flow of the gas phase with pressure ratio.

4.6. Effect of Rotational Speed

The rotational speed of the turbine wheel has an impact on the condensation characteristics of the humid air in it. The speeds tested are 60000 RPM, 80000 RPM, 110000 RPM, and the original case setup speed, 97000 RPM. The other inlet parameters, such as relative humidity and inlet pressure, are maintained. The mass flow rate changes accordingly in each case. Larger rotor speeds lead to larger pressure drops, which can affect the ability of the flow to reach saturation conditions, and consequently, to condense.

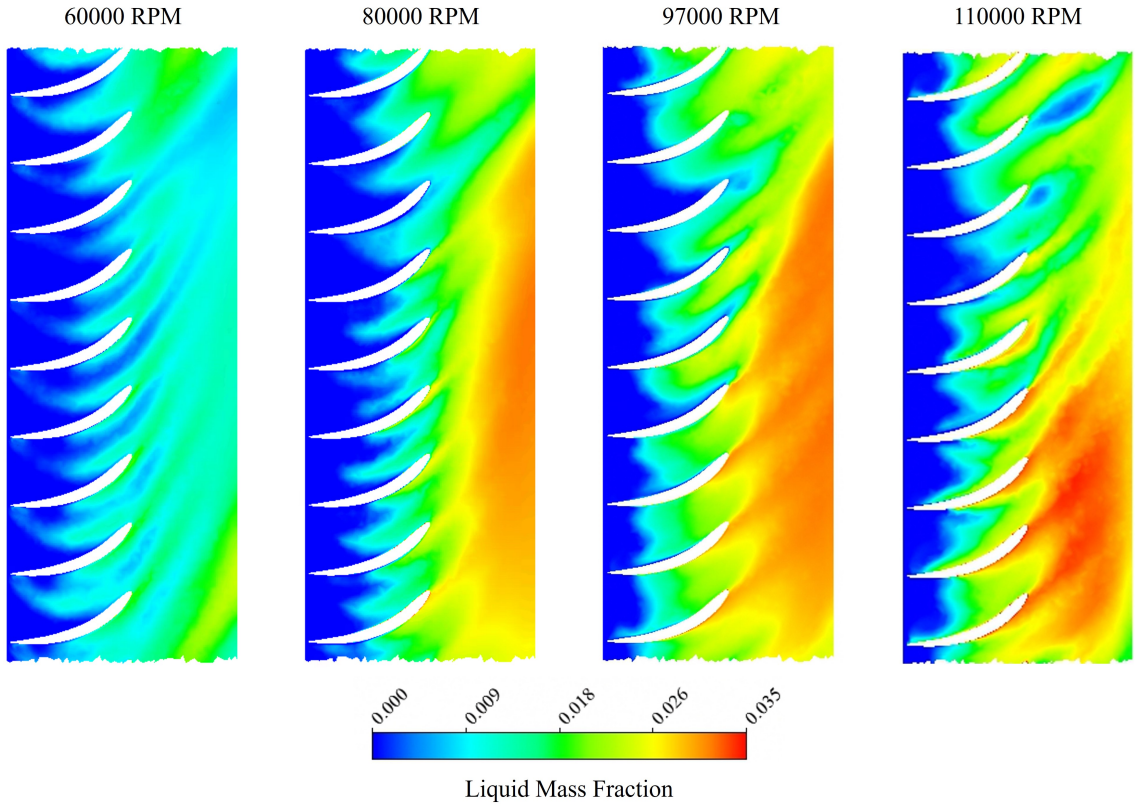

Figure 4.26: The blade-to-blade plots showing liquid mass fraction at 50% span for different rotational speeds.

In Figure 4.26, the blade-to-blade plots of the liquid mass fraction are presented for all four rotational speeds. It is evident that the 60000 RPM case experiences the least liquid formation, and the onset of condensation occurs close to the end of the blade passage. Most of the liquid generated is downstream of

the rotor wheel. 60000 RPM is a very low off-design speed, and it is included in the analysis only for the sake of comparison. At 80000 RPM, the extent of liquid generation is comparable to the original case at 97000 RPM discussed earlier. Interestingly, the liquid generation decreases with a further increase in the rotational speed, as seen in the 110000 RPM case. Some liquid generation is still observed in the blade passages farther from the scroll inlet, where subcooling was observed to be higher. This is in agreement with results from a study by Wittmann et al. [18].

This happens because the onset of condensation is pushed away from the inlet and the leading edge tip gaps due to higher speeds. For the lowest speed of 60000 RPM, it is observed that some liquid is formed at the leading edge tips, seen as streaks continuing into the blade passages. The liquid generation near tip gaps is prevalent at lower speeds, and is hindered at large speeds, causing a delay in the onset of condensation, and thus, lower liquid generation. Another possible reason for the lower liquid mass fraction in the 110000 RPM case is the reduced subcooling. A rapid expansion leads to a large pressure drop, causing the saturation temperature to fall. This can lower the subcooling ($T_{sat}(P) - T$), causing fewer cells to reach the threshold value required to form liquid. A similar trend is reflected in the

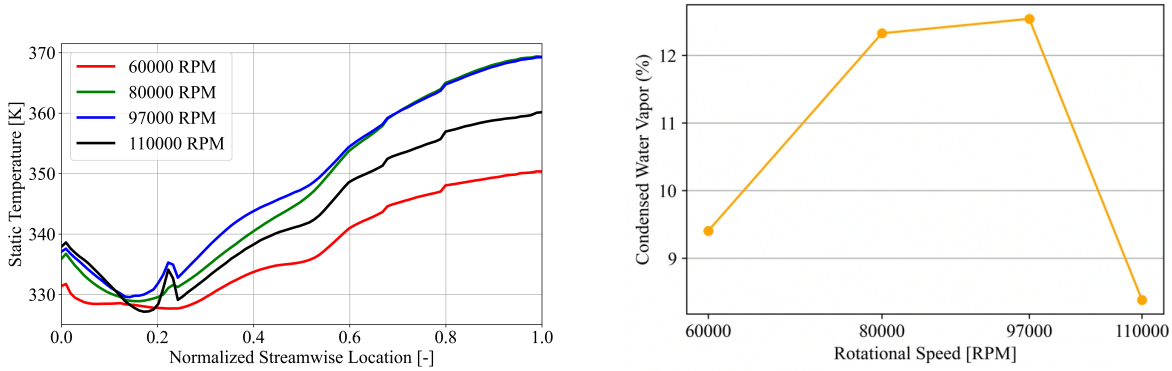

Figure 4.27: (a) The inlet-to-outlet distribution of the static temperature for different rotational speeds; (b) The variation in the condensed water vapor fraction at the outlet, with rotational speed.

inlet-to-outlet distribution of temperature, as shown in Figure 4.27a. The lowest rise in temperature due to minimal latent heat release is recorded in the 60000 RPM case. The rotor outlet temperature is almost 20K less than the runs with higher RPMs. The 80000 and 97000 RPM cases exhibit similar averaged temperature distributions, as the degree of expansion, as well as liquid generation, are very close. The highest speed of 110000 RPM yields a relatively lower amount of liquid, and thus the outlet temperature is less than the 97000 RPM case.

In Figure 4.27b, the condensed vapor fraction is presented. It is seen that the percentage of the vapor condensed starts from a lower value, reaches a peak as the rotor speed is increased, and finally decreases again. The fraction drops to an even lower value on the higher side of the design speed, which is in agreement with results from Wittmann et al. [18], who observed the same trend. Even though the liquid generation in the 110000 RPM case seems more than that in the 60000 RPM one, as seen in Figure 4.26, the condensed vapor percentage is slightly lower. This is because the mass flow rates for the two cases are different, and these values only represent the liquid generation in terms of a fraction of the total mass flow.

4.7. Efficiency

For any work-extracting device, such as a turbine, it is important to characterize how thermodynamically efficient its conversion of available energy to useful work is. The baseline for comparison is often taken to be an ideal case in which the expansion is isentropic, i.e., the maximum possible work is extracted. In Figure 4.28a, the usual turbine expansion process is illustrated on the enthalpy-entropy ($h - s$) plane by the black continuous line. The isentropic expansion is represented by the dashed line, and the real process, in case of condensation, by the continuous line and the dotted line, showing the enthalpy rise due to the latent heat release and the increase in entropy due to irreversibilities. Here, the total-to-static

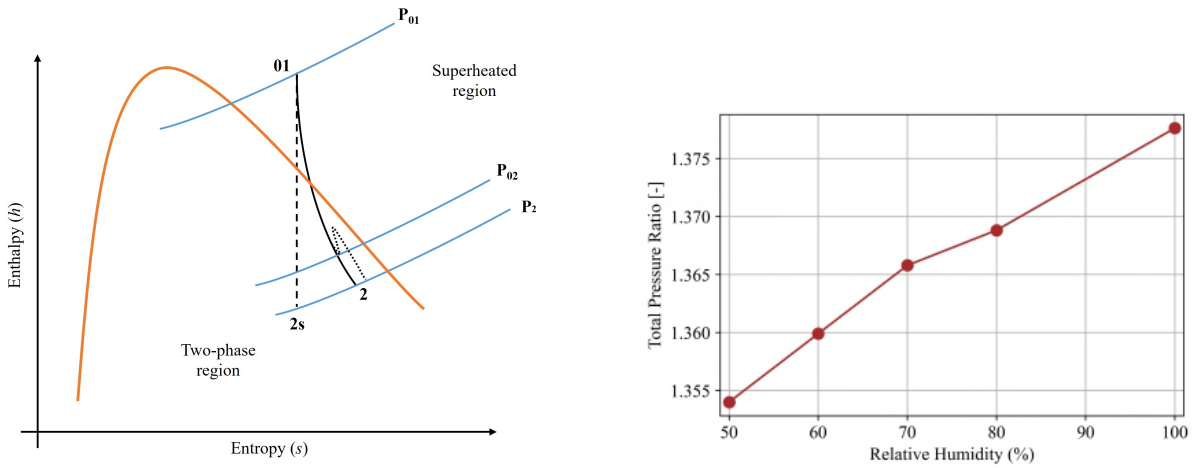

Figure 4.28: (a) A representation of the isentropic (dashed black line) and the actual (solid black line) enthalpy drop for the expansion in the turbine on the Mollier ($h-s$) plane, the dotted black line denotes the enthalpy increase due to condensation, and the orange line denotes the saturation curve; (b) The variation in the total pressure ratio across the rotor, with relative humidity.

isentropic efficiency is considered, which is given by,

$$\eta_t = \frac{\Delta h_{\text{actual}}}{\Delta h_{\text{isentropic}}} = \frac{h_{01} - h_2}{h_{01} - h_{2s}}, \tag{4.9}$$

where '01' represents stagnation conditions at the inlet, and '2', the static conditions at the outlet.

However, in this present case, the steam at the turbine inlet is superheated, and through the course of expansion it crosses the saturation line into the two-phase region. The actual expansion path includes the dotted line, as the enthalpy increases. This makes the calculation of the efficiency more complicated, as the release of latent heat distorts the enthalpy values and fields associated with it [15]. Thus, the efficiency is obtained from the power generated by the turbine,

$$\eta_t = \frac{\tau\Omega/\dot{m}}{(h_{01} - h_{2s})}, \tag{4.10}$$

where the power is calculated from the product of the torque on the blades τ and the angular speed Ω. The mass flow through the turbine is $\dot{m}$. The isentropic enthalpy drop is given from the ideal gas isentropic relations,

$$h_{01} - h_{2s} = \frac{\gamma}{\gamma - 1} \cdot \frac{P_1}{\rho_1} \left[1 - \left(\frac{P_2}{P_1} \right)^{\frac{\gamma-1}{\gamma}} \right] + \frac{V_1^2}{2}. \tag{4.11}$$

The isentropic efficiency is the standard ideal case which produces the maximum possible enthalpy drop, and therefore, work extraction. However, even if the ideal expansion were to occur under these conditions, the flow would condense, as the saturation line is still crossed. Thus, our definition of the isentropic enthalpy change might not be complete and requires further scrutiny. This definition can be proceeded with, as it has also been utilized by other authors to evaluate efficiency in condensing flows [17].

The isentropic efficiencies for both the wet (with condensation) and dry (without condensation) cases are presented in Figure 4.29a. For the dry cases, the overall efficiency for each composition is higher as compared to their respective condensing case, as the torque is higher. This is because there is a larger gaseous mass flow that performs work on the turbine, as compared to the wet cases. The

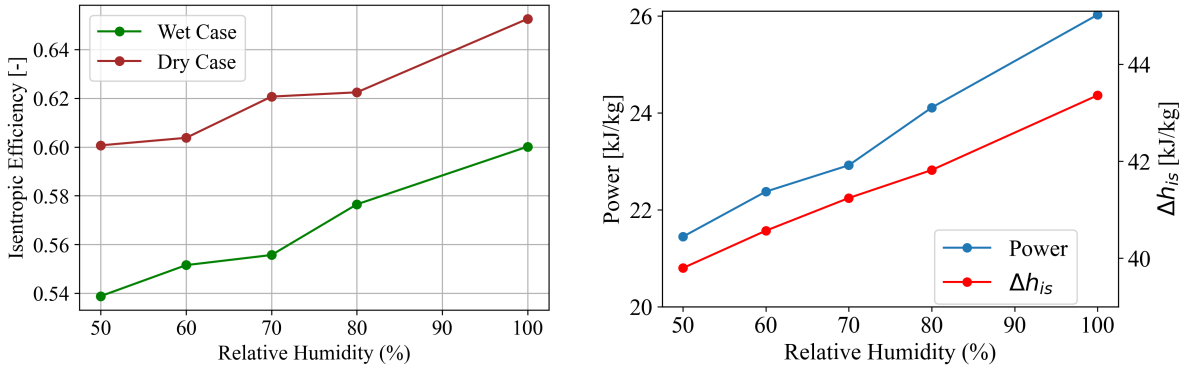

Figure 4.29: (a) The variation of isentropic efficiency of the turbine with a change in the relative humidity, (b) The change in the two components used to define the isentropic efficiency - power per unit mass flow ($\tau\Omega/\dot{m}$), and isentropic enthalpy drop (Δh_{is}), with relative humidity.

dry efficiency also increases with increasing relative humidity (without condensing), as the isentropic exponent decreases, making the expansion capacity better.

For the wet cases, the efficiency is seen to increase almost linearly from 54% to 60% with the rise in relative humidity. This is contrary to what is observed in the results from Wittmann et al. [17], where efficiency decreases as the air becomes more humid. This change is primarily because in the present study, the turbine outlet temperature is higher than the inlet temperature, due to the release of a high amount of latent heat. This was not the case for Wittmann et al. [17]; however, they noted that the efficiency of the turbine might rise in certain applications where the turbine experiences a temperature increase at the outlet, similar to our case.

To further understand why the efficiency increases in the present case, it is important to understand how the individual terms change as RH increases. The power output per unit mass flow increases with the relative humidity, which is consistent with published results [17]. This happens mainly due to two reasons - the increase in the total pressure ratio across the turbine due to thermal throttling as the air becomes more humid, which is shown in Figure 4.28b. Secondly, it is due to the increase in the specific heat ratio (γ) for wet air, as compared to dry air. The isentropic enthalpy change, which is the denominator, also increases, but the increase is slower than the rise in power, as shown in Figure 4.29b. This leads to an increase in the isentropic efficiency.

The rise in the isentropic enthalpy change with increasing relative humidity can be explained by the change in the pressure ratio across the rotor. Due to thermal throttling, the total pressure changes across the turbine with condensation, even though the imposed pressure ratio and the mass flow rate are kept constant for all the cases. The pressure ratio (P_2/P_1) across the rotor increases with the increase in relative humidity. But the inlet pressure to the rotor also increases to maintain the mass flow, and so does the velocity of the flow. From Equation 4.11, it can be seen that these changes lead to an increase in the values of Δh_{is}.

The analysis of the results leads to several interesting conclusions and implications for the overall system, which are discussed in the chapter ahead.

5

Conclusions and Outlook

5.1. Conclusions

The present study aimed to demonstrate how the condensation in fuel cell turbocharger turbines can impact the thermodynamics of the system. An Euler-Euler approach was used, and the condensation was integrated into the ANSYS Fluent framework with a User-Defined Function (UDF). The main conclusions that can be outlined from the analysis done are as follows:

The modelling approach:

- From the literature review, it was found that the problem of condensation in turbines has been studied extensively, however, most of the studies are related to low pressure steam turbines. Fuel cell turbocharger turbines are inherently different, as they operate in much more humid conditions, under relatively lower temperatures and pressures. Thus, these turbines require a dedicated analysis of the liquid generation under such conditions.
- It is a complex problem involving compressible multiphase physics in a turbulent flow through a turbine rotor. A robust way to capture the physics is using Lagrangian particle tracking models [15], which are computationally heavy. The model used in this study is a fully Eulerian one, implemented in ANSYS Fluent. A user-defined function (UDF) was implemented in the Fluent framework which used a critical level of subcooling to trigger condensation. The predicted physics agrees well with results from published literature.
- The Cartesian 2D Moore B nozzle geometry was used to validate our model. The experimental results were reproduced with accuracy, and the results showed good agreement with other numerical studies available in literature as well. The slip velocity was disabled when the model was adapted for the full turbine geometry, to provide numerical stability.
- The critical values of the subcooling that were used to trigger condensation in this study have been obtained from experimentally verified results from Mao et al. [68]. However, there are no experimental results available for the particular blade geometry used, and it is important that test results are available to calibrate the model better.

A summary of the analysis of the results:

- From the analysis of the results, it was observed that the prediction of the location of the onset of condensation, and the temperature and Mach number distribution showed agreement with published literature. The extent of the liquid generation was over-predicted, as compared to the few other studies conducted for FC turbocharger turbines. However, there are differences in operating conditions and blade geometry which makes only a qualitative comparison possible.
- The outlet of the turbine rotor was found to be hotter than the inlet, which was a reflection of the high latent heat release due to liquid generation. It has been mentioned in literature that this is observed in the later stages of some multistage operations where the strong condensation heats

up the flow significantly, also providing a power potential. This leads to a higher power output despite the smaller gaseous mass flow rate, which is exactly what is found in the present study.

- With an increase in the relative humidity, the subcooling of the flow was observed to be stronger, leading to more liquid generation. The decrease in the gaseous mass flow rate is almost linear with the rise in humidity.
- For a fixed mass flow rate, due to condensation, the pressure ratio across the turbine changes. This is a phenomenon called thermal throttling. The effective pressure drop across the turbine rotor was seen to drop in the 'wet' case, when compared to a case under the same conditions without the occurrence of condensation. As the pressure ratio increases, the amount of liquid generation is determined by the balance of the competing mechanisms of expansion and pressure rise due to latent heat release.
- The extent of condensation for different rotational velocities was also compared. It was found that for low rotational speeds the liquid generation is quite low, and increases on increasing the speed. A peak is reached for the condensed steam fraction, and on increasing the speed further, the liquid generation seemed to drop. This was in agreement with published results.
- The isentropic efficiency of the turbine under wet conditions, for different relative humidities, was evaluated. Because of the condensing flow and the release of latent heat, it was difficult to use the thermodynamic definition of the efficiency (Δh). Thus, it was defined using the expression for the power generated. The efficiency was seen to increase with an increase in the relative humidity, due to the increase in the power potential from the additional latent heat in the system.

Implications for the system:

- The large latent heat release and the gaseous mass flow change lead to the thermal throttling of the turbine, resulting in a change of the performance characteristics of the turbine. So, a given performance chart is only applicable for a particular relative humidity at the turbine inlet [15]. This affects the operation of the other components in the system, such as the compressor which the turbine assists. It was found that the surge margin for the compressor is reduced when operating with a turbine in which liquid condenses out.
- Accumulation of condensed liquid in several condensation-prone areas, such as the rotor outlet, and the droplets striking the blades can cause corrosive damage to the turbine components. The gaseous flow through the turbine is likely to be hindered in case of too much condensation.
- If any component is too close to the outlet of the turbine, the heat might cause adverse effects. The components downstream may behave differently than intended.
- The power generated can increase with an increase in the humidity of the flow, and in practice, this effect can be utilized.

5.2. Recommendations for Future Work

- **Experimental data to tune model:** The current model uses data from literature for choosing the subcooling threshold, which sacrifices some accuracy due to the blade geometry being different. The Lee model in ANSYS Fluent is used to trigger condensation, and it is associated with two coefficients to determine evaporation and condensation, as seen in Equation 3.34 and Equation 3.35. The value of the condensation coefficient was chosen by tuning the model to the Moore B nozzle test data. The evaporation coefficient was maintained at 0.1, since no evaporation was accounted for here.

  It is important to consider the possibility of evaporation of some of the liquid water that is condensed due to high temperature. It is difficult to model with just local conditions and coefficients, unless experimental data is available that measures exactly how much liquid is seen downstream of the rotor. Thus, test data is essential to tune the model and make it robust.
- **Choosing a different trigger for enabling condensation:** In this present study, only the flow subcooling was chosen as a trigger for condensation. An attempt was made to use nucleation rate as the trigger, but it did not seem to work well without a discrete particle tracking model enabled, as done by Wittmann et al. [17]. For a fully Eulerian approach, the zones of condensation

given by this method were abrupt and did not seem physically consistent. Another parameter that can be used to trigger nucleation is the supersaturation ratio S, which is the ratio of the vapor pressure to the local saturation pressure. In theory, if $S > 1$, there should be droplets nucleating. However, due to metastability, the critical nucleation values have been found to be higher, around 5, from experiments conducted in expansion cloud chambers [93]. This was tested for the Moore B nozzle with $S = 5$, and it did not provide good agreement with experimental data, as shown in Figure 5.1. The condensation shock is predicted much earlier and closer to the throat. Increasing it did not replicate the experimental profile very well either. This shows that the trigger value needs more tuning, or could be even combined with the subcooling trigger. This is something that could be explored further.

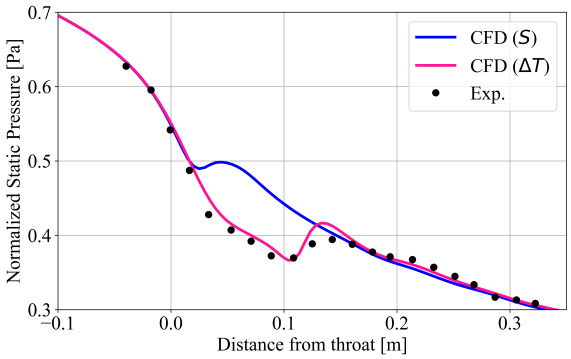

Figure 5.1: Static pressure profiles in the Moore B nozzle with different triggers for condensation, subcooling (ΔT) and supersaturation ratio (S), against experimental data.

- **Using a transient iterative approach:** In this study, a steady-state case was solved, where subcooling was checked in a preliminary simulation. A transient approach could be implemented here, which updates the subcooling at the end of every time step. The subcooling criterion is re-evaluated. Then, the regions that no longer satisfy the critical subcooling conditions due to latent heat release are taken into account. This establishes an iterative feedback system that accounts for the reduction in subcooling based on how the flow properties change.

  However, evaluating the subcooling requires the saturation temperature, which is dependent on the local mass fraction of the flow. Therefore, if the critical subcooling varies based on the local relative humidity of the flow, then this critical subcooling value must also be re-evaluated accordingly. For this, again, experimental data is required, to establish a relationship between the flow conditions and maximum subcooling. Moreover, attaining numerical stability in a transient simulation of such flows can be challenging.
- **Efficiency calculation:** The total-to-static isentropic efficiency was already obtained in this study. The isentropic enthalpy drop is measured in the conventional way from the ideal gas isentropic relations. This might not be completely accurate, as even in the ideal case of isentropic expansion that is chosen as the baseline, there should be flow condensing, because the saturation line is crossed. There are still questions about the definition of the baseline for comparison in the research community.
- **Near-wall effects:** The current case uses wall functions to resolve the boundary layer, as is usually the norm for computationally heavy turbomachinery cases. However, it might be of interest to simulate the same case with a wall-resolved approach, as it can capture the physics better near the blades. This will provide a better estimate of the static pressure near the blades and close to the hub, and consequently, a more accurate prediction of condensation in those regions.

  Moreover, the frozen-rotor interface method is used, which fixes the blade positions relative to the scroll, which leads to some deviation from the actual behavior. A more comprehensive sliding mesh model could be used to study the phenomena in greater detail.

Overall, this study is motivated to serve as a basis for further research on this phenomena. There is extensive scope for development of robust models, which requires experiments being undertaken to provide more data for validation. The work could find potential applications in fuel cell applications beyond automobile turbochargers.

References

[1] Julio A Sanguesa, Vicente Torres-Sanz, Piedad Garrido, Francisco J Martinez, and Johann M Marquez-Barja. A review on electric vehicles: Technologies and challenges. *Smart Cities*, 4(1): 372–404, 2021.

[2] Brahim Mebarki, Boumediene Allaoua, Belkacem Draoui, and Djamel Belatrache. Study of the energy performance of a pem fuel cell vehicle. *International Journal of Renewable Energy Research (IJRER)*, 7(3):1395–1402, 2017.

[3] Yun Wang, Bongjin Seo, Bowen Wang, Nada Zamel, Kui Jiao, and Xavier Cordobes Adroher. Fundamentals, materials, and machine learning of polymer electrolyte membrane fuel cell technology. *Energy and AI*, 1:100014, 2020.

[4] Ltd. Mitsubishi Heavy Industries. Development of electric turbochargers for fuel cell systems, 2025. URL `https://www.mhi.co.jp/technology/review/pdf/e602/e602140.pdf`. Accessed: 2025-03-12.

[5] A Dalvi and M Guay. Control and real-time optimization of an automotive hybrid fuel cell power system. *Control Engineering Practice*, 17(8):924–938, 2009.

[6] Eva Schießwohl, Thomas von Unwerth, Frank Seyfried, and Dieter Brüggemann. Experimental investigation of parameters influencing the freeze start ability of a fuel cell system. *Journal of Power Sources*, 193(1):107–115, 2009.

[7] Ltd. Mitsubishi Heavy Industries. Development of electric turbochargers for fuel cell systems, 2025. URL `https://www.mhi.co.jp/technology/review/en/abstracte-60-2-140.html`. Accessed: 2025-03-12.

[8] Stefan Pischinger, C Schönfelder, W Bornscheuer, H Kindl, and A Wiartalla. Integrated air supply and humidification concepts for fuel cell systems. *SAE Transactions*, pages 86–92, 2001.

[9] `https://www.edmunds.com/car-buying/turbocharger-technology-gives-new-cars-more-mpg.html`. [Accessed 26-02-2025].

[10] FuelCellCars.com. Fuel cells: All about - how do they work?, 2025. URL `https://fuelcellscars.com/Fuel_Cells_All_About_How_Do_They_Work.htm`. Accessed: 2025-03-12.

[11] BG Pollet, I Staffell, JL Shang, and V Molkov. Fuel-cell (hydrogen) electric hybrid vehicles. In *Alternative fuels and advanced vehicle technologies for improved environmental performance*, pages 685–735. Elsevier, 2014.

[12] Radu Tirnovan and Stefan Giurgea. Efficiency improvement of a pemfc power source by optimization of the air management. *International Journal of Hydrogen Energy*, 37(9):7745–7756, 2012.

[13] Dong Kyu Kim, Jeong Hoon Seo, Seonyeob Kim, Min Kyu Lee, Ki Young Nam, Han Ho Song, and Min Soo Kim. Efficiency improvement of a pemfc system by applying a turbocharger. *International journal of hydrogen energy*, 39(35):20139–20150, 2014.

[14] Dietmar Filsinger, Gen Kuwata, and Nobuyuki Ikeya. Tailored centrifugal turbomachinery for electric fuel cell turbocharger. *International Journal of Rotating Machinery*, 2021(1):3972387, 2021.

[15] Tim Wittmann, Sebastian Lück, Christoph Bode, and Jens Friedrichs. On the impact of condensation and liquid water on the radial turbine of a fuel cell turbocharger. *Machines*, 10(11):1053, 2022.

[16] Tim Wittmann, Sebastian Lück, Tim Hertwig, Christoph Bode, and Jens Friedrichs. The influence of condensation on the performance map of a fuel cell turbocharger turbine. In *Turbo Expo: Power for Land, Sea, and Air*, volume 84997, page V006T19A001. American Society of Mechanical Engineers, 2021.

[17] Tim Wittmann, Sebastian Lück, Christoph Bode, and Jens Friedrichs. Modelling the condensation phenomena within the radial turbine of a fuel cell turbocharger. *International Journal of Turbomachinery, Propulsion and Power*, 6(3):23, 2021.

[18] Tim Wittmann, Sebastian Lück, Jens Friedrichs, Piotr Wiśniewski, and Sławomir Dykas. Analysis of the condensation phenomena within the radial turbine of a fuel cell turbocharger. In *Turbo Expo: Power for Land, Sea, and Air*, volume 86106, page V10BT35A010. American Society of Mechanical Engineers, 2022.

[19] F Bakhtar. Special issue on wet steam. *Proceedings of the Institution of Mechanical Engineers, Part C: Journal of Mechanical Engineering Science*, 218(8):i–iii, 2004.

[20] JA Hesketh and PJ Walker. Effects of wetness in steam turbines. *Proceedings of the Institution of Mechanical Engineers, Part C: Journal of Mechanical Engineering Science*, 219(12):1301–1314, 2005.

[21] JB Young and AJ White. Special issue on the baumann wet steam conference. *Proc. Inst. Mech. Eng. Part A J. Power Energy*, 228:108–109, 2014.

[22] Herbert B Callen. *Thermodynamics and an Introduction to Thermostatistics*. John wiley & sons, 1991.

[23] P Carles. A brief review on the onset of free convection near the liquid-vapour critical point. *Journal de Chimie Physique et de Physico-Chimie Biologique*, 96(6):1044–1051, 1999.

[24] JD Gunton. Homogeneous nucleation. *Journal of statistical physics*, 95:903–923, 1999.

[25] Can F Delale, Günter H Schnerr, and Marinus E H van Dongen. Condensation discontinuities and condensation induced shock waves. *Shock Wave Science and Technology Reference Library: Multiphase Flows I*, pages 187–230, 2007.

[26] James E McDonald. Homogeneous nucleation of vapor condensation. i. thermodynamic aspects. *American Journal of Physics*, 30(12):870–877, 1962.

[27] Peter G Vekilov. Nucleation. *Crystal growth & design*, 10(12):5007–5019, 2010.

[28] Farhang Bakhtar, JB Young, AJ White, and DA Simpson. Classical nucleation theory and its application to condensing steam flow calculations. *Proceedings of the Institution of Mechanical Engineers, Part C: Journal of Mechanical Engineering Science*, 219(12):1315–1333, 2005.

[29] Farid Abraham. *Homogeneous nucleation theory: the pretransition theory of vapor condensation*, volume 1. Elsevier, 2012.

[30] WJ Dunning. General and theoretical introduction. In *Nucleation*, pages 1–67. Marcel Dekker New York, 1969.

[31] IJ Ford. Nucleation theorems, the statistical mechanics of molecular clusters, and a revision of classical nucleation theory. *Physical Review E*, 56(5):5615, 1997.

[32] A Dillmann and GEA Meier. A refined droplet approach to the problem of homogeneous nucleation from the vapor phase. *The Journal of chemical physics*, 94(5):3872–3884, 1991.

[33] Barbara N Hale. Monte carlo calculations of effective surface tension for small clusters. *Australian journal of physics*, 49(2):425–434, 1996.

[34] Kari Laasonen, Stephan Wonczak, Reinhard Strey, and Ari Laaksonen. Molecular dynamics simulations of gas–liquid nucleation of lennard-jones fluid. *The Journal of Chemical Physics*, 113 (21):9741–9747, 2000.

[35] Max Volmer. Nucleus formation in supersaturated systems. *Z. Phys. Chem.*, 119:277–301, 1926.

[36] Ladislaus Farkas. Keimbildungsgeschwindigkeit in übersättigten dämpfen. *Zeitschrift für physikalische Chemie*, 125(1):236–242, 1927.

[37] Richard Becker and Werner Döring. Kinetische behandlung der keimbildung in übersättigten dämpfen. *Annalen der physik*, 416(8):719–752, 1935.

[38] David W Oxtoby. Homogeneous nucleation: theory and experiment. *Journal of Physics: Condensed Matter*, 4(38):7627, 1992.

[39] Keramat Fakhari. Numerical modeling and investigation of unsteady phenomena in condensing flows of industrial steam turbines. 2011.

[40] Max Volmer. Kinetik der phasenbildung. *(No Title)*, 1939.

[41] Ja B Zeldovich. On the theory of formation of a new phase, cavitation. *J. Exp. Theor. Phys.*, 12: 525, 1942.

[42] Welby G Courtney. Remarks on homogeneous nucleation. *The Journal of Chemical Physics*, 35 (6):2249–2250, 1961.

[43] Michael Mozurkewich. Aerosol growth and the condensation coefficient for water: A review. *Aerosol science and technology*, 5(2):223–236, 1986.

[44] AF Mills and RA Seban. The condensation coefficient of water. *International Journal of Heat and Mass Transfer*, 10(12):1815–1827, 1967.

[45] Arthur Kantrowitz. Nucleation in very rapid vapor expansions. *The Journal of chemical physics*, 19(9):1097–1100, 1951.

[46] MJ Kermani and AG Gerber. A general formula for the evaluation of thermodynamic and aerodynamic losses in nucleating steam flow. *International journal of heat and mass transfer*, 46(17): 3265–3278, 2003.

[47] Andrew G Gerber. Two-phase eulerian/lagrangian model for nucleating steam flow. *J. Fluids Eng.*, 124(2):465–475, 2002.

[48] Tao Zhang, Chaohai Wei, Chunhua Feng, Yuan Ren, Haizhen Wu, and Sergei Preis. Advances in characteristics analysis, measurement methods and modelling of flow dynamics in airlift reactors. *Chemical Engineering and Processing-Process Intensification*, 144:107633, 2019.

[49] Hassan Pouraria, Jung Kwan Seo, and Jeom Kee Paik. Numerical modelling of two-phase oil–water flow patterns in a subsea pipeline. *Ocean Engineering*, 115:135–148, 2016.

[50] E Gharaibah, A Read, and G Scheuerer. Overview of cfd multiphase flow simulation tools for subsea oil and gas system design, optimization and operation. In *Offshore Technology Conference Brasil*, page D011S003R004. OTC, 2015.

[51] Marcus Mccallum and Roland Hunt. The flow of wet steam in a one-dimensional nozzle. *International journal for numerical methods in engineering*, 44(12):1807–1821, 1999.

[52] Shigeki Senoo and Yoshio Shikano. Non-equilibrium homogeneously condensing flow analyses as design tools for steam turbines. In *Fluids Engineering Division Summer Meeting*, volume 36169, pages 843–850, 2002.

[53] M García, Y Sommerer, T Schönfeld, and T Poinsot. Evaluation of euler-euler and euler-lagrange strategies for large-eddy simulations of turbulent reacting flows. In *ECCOMAS thematic conference on computational combustion*, volume 30, pages 1–18, 2005.

[54] GS Arnold, DA Drew, and RT Lahey Jr. An assessment of multiphase flow models using the second law of thermodynamics. *International journal of multiphase flow*, 16(3):481–494, 1990.

[55] JB Young. The fundamental equations of gas-droplet multiphase flow. *International journal of multiphase flow*, 21(2):175–191, 1995.

[56] John D Denton. *Loss mechanisms in turbomachines*, volume 78897. American Society of Mechanical Engineers, 1993.

[57] Jabir Edathol, Dmitrii Brezgin, Konstantin Aronson, and Heuy Dong Kim. Prediction of non-equilibrium homogeneous condensation in supersonic nozzle flows using eulerian-eulerian models. *International journal of heat and mass transfer*, 152:119451, 2020.

[58] Michael J Moore. Predicting the fog-drop size in wet-steam turbines. *Wet steam*, 1973.

[59] Pascal Post and Francesca di Mare. Highly efficient euler-euler approach for condensing steam flows in turbomachines. *GPPS Montreal*, 18, 2018.

[60] Jörg Starzmann, Fiona R Hughes, Sebastian Schuster, Alexander J White, Jan Halama, Vladimir Hric, Michal Kolovratník, Hoon Lee, Libor Sova, Miroslav Šťastný, et al. Results of the international wet steam modeling project. *Proceedings of the Institution of Mechanical Engineers, Part A: Journal of Power and Energy*, 232(5):550–570, 2018.

[61] Assim H Yousif, Amer M Al-Dabagh, and Reyadh Ch Al-Zuhairy. Non-equilibrium spontaneous condensation in transonic steam flow. *International journal of thermal sciences*, 68:32–41, 2013.

[62] Giacomelli Francesco, Mazzelli Federico, and Milazzo Adriano. Cfd modelling of the condensation inside a cascade of steam turbine blades: comparison with an experimental test case. *Energy Procedia*, 126:730–737, 2017.

[63] Guan Heng Yeoh and Jiyuan Tu. *Computational techniques for multiphase flows*. Butterworth-Heinemann, 2019.

[64] Ahmed M Nagib Elmekawy and Mohey Eldeen HH Ali. Computational modeling of non-equilibrium condensing steam flows in low-pressure steam turbines. *Results in Engineering*, 5: 100065, 2020.

[65] Sebastian Schuster, Dieter Brillert, and Friedrich-Karl Benra. Condensation in radial turbines—part i: mathematical modeling. *Journal of Turbomachinery*, 140(10):101001, 2018.

[66] ANSYS Inc. *ANSYS Fluent Theory Guide*. ANSYS Inc., 2023. Available at: `https://www.ansys.com`.

[67] Tim Wittmann, Sebastian Lück, Christoph Bode, and Jens Friedrichs. Investigation of water droplet erosion in the radial turbine of a fuel cell turbocharger. *Proceedings of Global Power and Propulsion Society*, pages 18–20, 2021.

[68] Haoyu Mao, Xingwang Tang, Jinling Liu, and Sichuan Xu. Numerical investigation of the non-equilibrium condensation inside a fuel cell turbine with variable geometry. *International Journal of Heat and Mass Transfer*, 217:124710, 2023.

[69] PT Walters. Optical measurement of water droplets in wet steam flows. In *Heat and Fluid Flow in Steam and Gas Turbine Plant, Conf. Publ*, number 3, page 216, 1973.

[70] G Gyarmathy. Nucleation of steam in high-pressure nozzle experiments. *Proceedings of the Institution of Mechanical Engineers, Part A: Journal of Power and Energy*, 219(6):511–521, 2005.

[71] DA Labuntsov, AG Lobachev, BA Kol'chugin, and EA Zakharova. The main principles of variation in vapour content of equilibrium and non-equilibrium twophase flows in channels of different geometry. *Thermal Engineering*, 31(9):506–508, 1984.

[72] F Bakhtar and K Zidi. Nucleation phenomena in flowing high-pressure steam: experimental results. *Proceedings of the Institution of Mechanical Engineers, Part A: Journal of Power Engineering*, 203(3):195–200, 1989.

[73] Clifford A Moses and Gilbert D Stein. On the growth of steam droplets formed in a laval nozzle using both static pressure and light scattering measurements. 1978.

[74] Georg Gyarmathy. Zur wachstumsgeschwindigkeit kleiner flüssigkeitstropfen in einer übersättigten atmosphäre. *Zeitschrift für angewandte Mathematik und Physik ZAMP*, 14:280–293, 1963.

[75] Philip G Hill. Condensation of water vapour during supersonic expansion in nozzles. *Journal of Fluid Mechanics*, 25(3):593–620, 1966.

[76] Alexander J White, John B Young, and Paul T Walters. Experimental validation of condensing flow theory for a stationary cascade of steam turbine blades. *Philosophical Transactions of the Royal Society of London. Series A: Mathematical, Physical and Engineering Sciences*, 354(1704): 59–88, 1996.

[77] F Bakhtar, RA Webb, MH Shojaee-Fard, and MA Siraj. An investigation of nucleating flows of steam in a cascade of turbine blading. 1993.

[78] Farhang Bakhtar, Mojtaba Ebrahimi, and Richard A Webb. On the performance of a cascade of turbine rotor tip section blading in nucleating steam: part 1: surface pressure distributions. *Proceedings of the Institution of Mechanical Engineers, Part C: Journal of Mechanical Engineering Science*, 209(2):115–124, 1995.

[79] F Bakhtar, M Ebrahimi, and RA Webb. An investigation of nucleating flows of stream in a cascade of turbine blading—wake traverses. 1994.

[80] Chen Wang, Lei Wang, Hongxia Zhao, Zhongyong Du, and Zhaoqiu Ding. Effects of superheated steam on non-equilibrium condensation in ejector primary nozzle. *International Journal of Refrigeration*, 67:214–226, 2016.

[81] Hao Zhou, Xinliang Li, Han Qi, and Changping Yu. Subgrid-scale model for large-eddy simulation of transition and turbulence in compressible flows. *Physics of Fluids*, 31(12), 2019.

[82] Florian R Menter. Two-equation eddy-viscosity turbulence models for engineering applications. *AIAA journal*, 32(8):1598–1605, 1994.

[83] Wen Ho Lee. A pressure iteration scheme for two-phase flow modeling. *Multiphase transport fundamentals, reactor safety, applications*, 1:407–431, 1980.

[84] Asghar Alizadehdakhel, Masoud Rahimi, and Ammar Abdulaziz Alsairafi. Cfd modeling of flow and heat transfer in a thermosyphon. *International Communications in Heat and Mass Transfer*, 37(3):312–318, 2010.

[85] Stefano Bortolin, Enrico Da Riva, and Davide Del Col. Condensation in a square minichannel: application of the vof method. *Heat Transfer Engineering*, 35(2):193–203, 2014.

[86] J Sauter. Grössenbestimmung von brennstoffteilchen. *Forschungsarbeiten auf dem Gebiete des Ingenieurwesens*, 279, 1926.

[87] Thermopedia. Spray, 2025. URL `https://www.thermopedia.com/content/1108/`. Accessed: 2025-03-13.

[88] Novid Beheshti, Alexey A Burluka, and Michael Fairweather. Assessment of σ- y liq model predictions for air-assisted atomisation. *Theoretical and Computational Fluid Dynamics*, 21:381–397, 2007.

[89] ANSYS, Inc. Best practices for spatial discretization gradient. `https://innovationspace.ansys.com/courses/courses/tips-tricks-for-ansys-fluent-simulations-ansys-courses/lessons/spatial-discretization-best-practices-ansys-courses/`, April 2024. Accessed: 2025-06-17.

[90] He Li, Xiaodong Wang, Hailong Huang, Jiuxin Ning, and Jiyuan Tu. A numerical analysis of the influence of nozzle geometric structure on spontaneous steam condensation and irreversibility in the steam ejector nozzle. *Applied Sciences*, 11(24):11954, 2021.

[91] Haoyu Mao, Xingwang Tang, Jinling Liu, and Sichuan Xu. Numerical and experimental investigation on condensation inside a turbine designed for an 100 kw polymer electrolyte membrane fuel cell system. *International Journal of Hydrogen Energy*, 50:945–960, 2024.

[92] Sebastian Schuster, Friedrich-Karl Benra, Hans Josef Dohmen, Sven König, and Uwe Martens. Sensitivity analysis of condensation model constants on calculated liquid film motion in radial turbines. In *Turbo Expo: Power for Land, Sea, and Air*, volume 45585, page V01BT27A021. American Society of Mechanical Engineers, 2014.

[93] Farhang Bakhtar and Kaddour Zidi. Nucleation phenomena in flowing high-pressure steam part 2: theoretical analysis. *Proceedings of the Institution of Mechanical Engineers, Part A: Journal of Power and Energy*, 204(4):233–242, 1990.

[94] FF Abraham. Homogeneous nucleation theory, 1974. *New York: Academic*, 1979.

[95] D Kashchiev. Solution of the non-steady state problem in nucleation kinetics. *Surface Science*, 14(1):209–220, 1969.

[96] Grazia Lamanna. On nucleation and droplet growth in condensing nozzle flows. 2002.

[97] Georg Gyarmathy. *Grundlagen einer theorie der nassdampfturbine*. PhD thesis, ETH Zurich, 1962.

[98] P Peeters, CCM Luijten, and MEH Van Dongen. Transitional droplet growth and diffusion coefficients. *International journal of heat and mass transfer*, 44(1):181–193, 2001.

[99] J.B. Young and University of Cambridge. Engineering Department. *Spontaneous Condensation of Steam in Supersonic Nozzles: Part 1, Nucleation and Droplet Growth Theory; Part 2, Numerical Methods and Comparison with Experimental Results*. Number pts. 1-2 in CUED/A-Turbo/TR. University of Cambridge, Department of Engineering, 1980. URL `https://books.google.nl/books?id=Zu5fuAAACAAJ`.

[100] M Heiler. Instationare phanomene in homogen/heterogen kondensierenden dusen-und turbinenstromungen. *Dissertation, Fakultat fur Maschinenbau, Universitat Karlsruhe (TH)*, 1999.

[101] F Bakhtar and K Zidi. On the self diffusion of water vapour. *Proceedings of the Institution of Mechanical Engineers, Part C: Journal of Mechanical Engineering Science*, 199(2):159–164, 1985.

A

Appendix: Nucleation Rate and Droplet Growth Theory

A.1. Derivation of the Nucleation Rate expression

The derivation of the expression of the nucleation rate is discussed here. Let us consider a droplet of radius r, comprised of g molecules. It can be called a g-mer. Under steady state, the rate of acquisition of a molecule by the g-mer, say C_g, and the rate at which a $(g+1)$-mer loses a molecule must be equal. In other words, the condensation and evaporation rates must be balanced.

$$C_g n_g = E_{g+1} n_{g+1} \tag{A.1}$$

where, n_g, the number of g-mers per unit volume follows a Boltzmann distribution,

$$n_g = n_1 \exp\left(-\frac{\Delta G}{k_B T_v}\right) \tag{A.2}$$

n_1 being the number of monomers per unit volume [94]. However, in reality, it is erroneous to assume steady state, as the two rates are never balanced. To account for the difference, let f_g represent the concentration of the g-mers under these conditions. The growth rate I_g (also termed nucleation current) of these g-mers can be denoted by,

$$I_g = C_g f_g - E_{g+1} f_{g+1} \tag{A.3}$$

The rate of change in the concentration is given by,

$$\begin{aligned} \frac{\partial f_g}{\partial t} &= -\left[(C_g f_g - E_{g+1} f_{g+1}) - (C_{g-1} f_{g-1} - E_g f_g)\right] \\ &= -\left(I_g - I_{g-1}\right) \cong -\frac{\partial I_g}{\partial g} \end{aligned} \tag{A.4}$$

According to the kinetic theory, C_g can be obtained from the expression for the rate at which molecules impact the surface of the droplet. Assuming spherical droplets,

$$C_g = q_c A g^{2/3} \frac{\rho_v v_v}{4m} \tag{A.5}$$

where, v_v is the mean speed of the vapour molecules and q_c is the condensation coefficient. Solving (A.3), and eliminating the term E_{g+1}, we get

$$\frac{I_g}{C_g n_g} = \frac{f_g}{n_g} - \frac{f_{g+1}}{n_{g+1}} \cong -\frac{\partial}{\partial g}\left(\frac{f_g}{n_g}\right) \tag{A.6}$$

We use (A.2) to eliminate E_{g+1}. Eliminating I_g from equations (A.4) and (A.6), we obtain the time rate of change in concentration,

$$\frac{\partial f_g}{\partial t} = -\frac{\partial I_g}{\partial g} = \frac{\partial}{\partial g}\left[C_g n_g \frac{\partial}{\partial g}\left(\frac{f_g}{n_g}\right)\right] \tag{A.7}$$

(A.7) governs isothermal nucleation, which can be carried out in two ways - steady or transient. One of the solutions to the transient problem was investigated semi-analytically by Kashchiev [95], in terms of a characteristic time τ. If a given supersaturation is imposed initially on the vapor in a saturated state, then I_g reaches 99% of its steady state value in a characteristic time of 10^{-7} to 10^{-6} s. This timescale is found to be smaller than the overall time for active nucleation in nozzles.
Usually, the transient state is neglected and it is assumed that the steady state nucleation rate is attained instantaneously. For the steady state solution, integrating (A.6),

$$I_{\mathrm{CL}} \int_{g=1}^{\infty} \frac{\mathrm{d}g}{C_g n_g} = \int_{g=1}^{\infty} -\mathrm{d}\left(\frac{f_g}{n_g}\right) \tag{A.8}$$

I_{CL} being the classical steady-state value of I. Solving the integral on the right hand side,

$$I_{\mathrm{CL}} = \left[\int_{g=1}^{\infty} \frac{\mathrm{d}g}{C_g n_g}\right]^{-1} \tag{A.9}$$

Evaluating it analytically, we get the nucleation rate J_{CL} per unit volume,

$$J_{CL} = q_c \frac{\rho_v^2}{\rho_l}\left(\frac{2\sigma}{\pi m^3}\right)^{1/2} \exp\left(-\frac{4\pi r^{*2}\sigma}{3k_B T_v}\right) \tag{A.10}$$

The nucleation rate J is negligibly small at low values of supersaturation ratios, but grows dramatically with an increase in subcooling $\Delta T = T_s - T_v$.

A.2. Droplet Growth Theory

In the current study, we have discussed the initiation of condensation. Although droplet growth models are not used in the solution process, it is useful to know how, upon nucleation, the clusters can grow in the supercooled vapor through the exchange of mass and energy with the vapor surrounding them. The droplet temperature rises above that of the vapor due to the liberation of latent heat, and consequently, so does the vapor pressure. This increase is very sudden and rapid as there is no surface other than the vapor to conduct the heat away. This is often termed as a condensation shock. The growth rate of the droplet is governed by the rate at which heat is conducted away from it, which is associated with the Knudsen number (Kn). It is defined as follows,

$$Kn = \frac{\tilde{l}}{2r} \tag{A.11}$$

which represents the ratio of the mean free path of the vapor molecules to the droplet diameter. The mean free path is given by,

$$\tilde{l} = \frac{3\mu_v}{P}\sqrt{\frac{\pi R T_v}{8}} \tag{A.12}$$

For small Kn (Kn << 1), the continuum hypothesis is valid, and diffusion is the primary transfer process. For large value of Kn (Kn >> 1), it acts as a rarefied gas and the kinetic theory is applicable, and the droplet growth process is governed by the kinetic process of impingement of the vapor molecules to the droplets [96]. For large Kn, the Hertz-Knudsen formula is widely used.

One of the oldest and the most popular models was given by [97], which is based on an interpolation of quantities such as temperature and vapor mass fractions between a very small and a very large Knudsen number, making it applicable for both continuum and rarefied regimes. The Nusselt number was used to quantify heat and mass fluxes that determined the droplet growth.

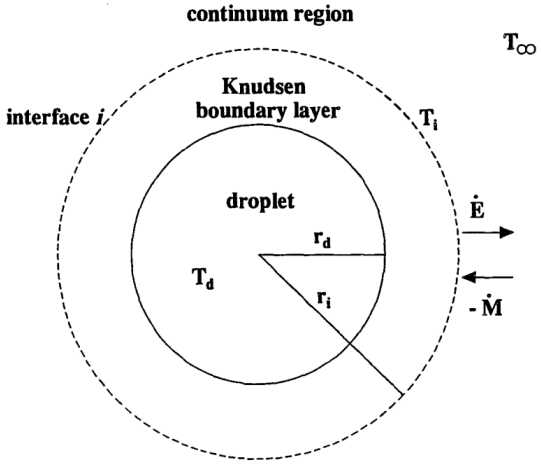

Figure A.1: Different regions in a droplet in the Young model [98].

Another popular growth model was given by [99], which was based on dividing the droplet into three regions - the droplet itself, the Knudsen boundary layer and the continuum region, as shown in Figure A.1. The innermost droplet is in equilibrium with its surface. The second layer has a width of the order of the mean free path of the free molecules, and in the outermost continuum region, the macroscopic conservation laws are valid. By equating heat and mass fluxes at the interface i between the Knudsen and continuum layer, the droplet growth rate can be attained.

Young's model is used in the continuum/diffusion regime ($0 \leq Kn \leq 0.1$), whereas the Gyarmathy model is applied in the transition regime ($0.1 \leq Kn \leq 10$) Peeters et al. [98]. Further improvements and corrections have been introduced in these models by researchers Heiler [100], Bakhtar and Zidi [101]. This model for estimating the growth rate of the radius is useful in the Lagrangian framework, and is included here for context. However, in this study, we will use an Eulerian framework, in which the two phases are treated as interpenetrating continua, and thus a "droplet" cannot be separated from the flow.